Inauguraldissertation
zur Erlangung des Doktorgrades der Naturwissenschaften
vorgelegt beim Fachbereich 07
(Mathematik und Informatik, Physik, Geographie)
der Justus-Liebig-Universität Gießen

Strain Engineering and Buffer Layer Design in VO_2 Thin Film Structures: From Phase Transition Mechanisms to Smart Window Applications

Kontrolle der Verspannung und Pufferschichtdesign in VO_2-Dünnschichtsystemen: Von den Mechanismen des Phasenübergangs zu Anwendungen in intelligenten Fenstern

---

von

Hao LU

aus Lu'An

I. Physikalisches Institut
AG Klar

2025

Dekan:	Prof. Dr. Christian Heiliger
Erstgutachter:	Prof. Dr. Peter J. Klar
Zweitgutachter:	Prof. Dr. Yunbin He
Verfassungsdatum:	20. Januar 2026

Zusammenfassung

Diese Dissertation behandelt zwei zentrale Forschungsrichtungen. Erstens untersuchen wir die Einstellbarkeit des Metall-Isolator-Übergangs (MIT) in kristallinen VO_2-Dünnfilmen durch Einstellen der Verspannung. Hochwertige epitaktische VO_2-Filme unterschiedlicher Dicke werden mittels Puls-Laser-Deposition auf TiO_2-(110)-Substraten abgeschieden. Der resultierende Verspannungszustand hängt von der Filmdicke ab. Diese Korrelation wird durch eine detaillierte Charakterisierung der strukturellen und elektrischen Eigenschaften ermittelt. VO_2-Filme mit einer Dicke von weniger als 20 nm bleiben vollständig verspannt und zeigen eine Zugspannung entlang der c-Achse der Rutilphase, was zu einer Erhöhung der MIT-Temperatur um bis zu 30°C im Vergleich zu relaxierten, 300 nm dicken Filmen führt. In dickeren Filmen induziert der Verspannungsgradient einen graduellen und räumlich variierenden Übergang der geschichteten VO_2-Regionen vom Isolator- in den Metallzustand bei Temperaturerhöhung.

Zweitens untersuchen wir den Einsatz von Rutil $Cu_xTi_{1-x}O_2$ als Pufferschicht zur Realisierung eines Niedertemperatur Wachstums von thermochromen VO_2-Filmen. Insbesondere analysieren wir den Einfluss des Kupfereinbaus auf die strukturellen und optischen Eigenschaften von TiO_2. Der Kupfereinbau führt zur Legierungsbildung und senkt die Übergangstemperatur von der Anatas- zur Rutilphase, wodurch sich Rutil-$Cu_xTi_{1-x}O_2$ bereits bei Sputtertemperaturen von 200°C bilden kann, im Vergleich zu 600°C für reines Rutil-TiO_2. Wir stellen eine Dreischichtstruktur bestehend aus einer $Cu_xTi_{1-x}O_2$-Pufferschicht, einer thermochromen VO_2-Schicht und einer Anatas-TiO_2-Antireflexionsschicht her und untersuchen deren thermochrome Kennzahlen. Obwohl die optische Transparenz von $Cu_xTi_{1-x}O_2$ im sichtbaren Spektralbereich mit steigendem Kupferanteil abnimmt, sind die Kennzahlen dieser Struktur mit denen einer analogen Struktur mit Rutil-TiO_2 als Pufferschicht vergleichbar. Somit ermöglicht der Einsatz einer Pufferschicht aus Rutil-$Cu_xTi_{1-x}O_2$ die Herstellung von VO_2-basierten Mehrschichtsystemen für thermochrome Anwendungen bei Herstellungstemperaturen, die mit industriellen Sputtersystemen kompatibel sind.

Abstract

This dissertation presents two main research directions. First, we investigate the tunability of the metal–insulator transition (MIT) in crystalline VO_2 thin films via strain engineering. High-quality VO_2 epitaxial films of various thicknesses are deposited on TiO_2 (110) substrates using pulsed laser deposition. The resulting strain state depends on the film thickness. This correlation is established by detailed characterization of the structural and electrical properties. VO_2 films thinner than 20 nm remain fully strained and exhibit tensile strain along the *c*-axis of the rutile phase, resulting in an increase of the MIT temperature by up to 30°C compared to relaxed 300 nm thick films. In thicker films, the strain gradient induces a gradual and spatially varying transition of layered regions from the insulating to the metallic phase upon heating.

Second, we investigate the use of rutile-phase $Cu_xTi_{1-x}O_2$ as a buffer layer to enable low-temperature growth of thermochromic VO_2. Specifically, we examine the influence of copper incorporation on the structural and optical properties of TiO_2. Copper incorporation promotes alloy formation and reduces the anatase-to-rutile transition temperature, allowing rutile-phase $Cu_xTi_{1-x}O_2$ to form during sputtering at temperatures as low as 200°C, versus 600°C for pure rutile TiO_2. We fabricate and investigate a tri-layer structure comprising a $Cu_xTi_{1-x}O_2$ buffer layer, a thermochromic VO_2 layer, and an anatase TiO_2 antireflection coating. Although increasing Cu content reduces the optical transparency of $Cu_xTi_{1-x}O_2$ in the visible range, the performance of the tri-layer structure approaches that of an analogous structure using rutile TiO_2 as the buffer layer. Thus, employing a rutile $Cu_xTi_{1-x}O_2$ buffer layer enables the fabrication of VO_2-based multilayer structures for thermochromic applications at temperatures compatible with industrial sputtering systems.

Contents

List of Figures ix

List of Tables xi

1 Introduction 1
1.1 Fundamental Studies of VO_2 3
1.1.1 Energy-Level Evolution of V $3d$ Orbitals in Octahedral Environments 3
1.1.2 Mechanisms of the Metal–Insulator Transition 9
1.1.3 Crystal Structure and Electronic Band Structure 13
1.1.4 Tuning the Metal–Insulator Transition 23
1.2 Thermochromic VO_2 Coatings for Smart Windows 28
1.2.1 Strategies for Lowering T_c 29
1.2.2 Band-Gap Engineering and Enhancing Visible Transparency 31
1.2.3 Challenges and Our Approaches 33

2 State of the Art 39
2.1 Thin Film Preparation and Characterization 39

3 Publication 1: Correlation of MIT and strain state of VO_2 thin films on TiO_2 (110) substrates 49

4 Publication 2: $Cu_xTi_{1-x}O_2$ buffer layers in VO_2–based smart windows – a viable compromise towards large-scale industrial production 67

5 Conclusions and Outlook 89

Bibliography 91

6 Acknowledgments 101

7 Declaration of Originality 103

List of Figures

1.1 Temperature dependence of the resistivity of a VO_2 film deposited on quartz substrate. The inner plot shows the derivative of the logarithm of resistivity. 2
1.2 (a) R-VO_2 and (b) M_1-VO_2 2
1.3 Spatial shapes of the five $3d$ atomic orbitals. 5
1.4 Schematic illustration of a V ion in a distorted octahedral crystal field. 6
1.5 Angular parts of the d orbitals 6
1.6 Orbital-overlap model of V–O bonding in rutile VO_2. 8
1.7 Temperature-Induced Orbital Reconstruction and Band Splitting Across the Metal–Insulator Transition in VO_2. 9
1.8 Generalized phase diagram of VO_2 under combined doping, stoichiometry, and strain control 14
1.9 Schematic diagram of the electronic band structure of M_1-VO_2 during n-type doping 15
1.10 Schematic diagram of the electronic band structure of M_1-VO_2 transformed from R-VO_2 with reduced c_R/a_R ratio under stress 16
1.11 Schematic illustration of V–V dimerization along the c-axis in the rutile structure of VO_2. 18
1.12 Schematic electronic band structure of metallic VO_2. Adopted from Ref. 19
1.13 Schematic electronic band structure of M_1-VO_2. 21
1.14 (a) Schematic diagram of a perfect cubic structure. (b) Cubic structure-edge dislocation 26
1.15 Growth window diagram for VO_2. 36

2.1 Schematic illustration of Rayleigh, Stokes, and anti-Stokes scattering. 44

List of Tables

1.1 Lattice parameters of different VO_2 phases (including α and γ). . . 13
1.2 Crystallographic parameters of rutile-related dioxides. 18
1.3 Summary of dopant effects on VO_2 transition temperature and optical properties 33

1 Introduction

The element vanadium was first discovered in the early 19th century and has since been recognized for the vibrant colors and diverse properties of its compounds. [1] Although Spanish-Mexican mineralogist Andrés Manuel del Río initially identified it in 1801, it was the Swedish chemist Nils Gabriel Sefström who is widely credited with its discovery in 1830. [2] He named the element *vanadium*, after the Norse goddess Vanadis, in reference to the brilliant hues of its various salts.

Among vanadium oxides, vanadium dioxide (VO_2) stands out as a prototypical correlated material exhibiting a sharp and reversible metal–insulator transition (MIT) near 68 °C, as shown in Figure **1.1**. [3,4] This first-order transition, accompanied by pronounced hysteresis, involves an abrupt change in electrical conductivity—up to five orders of magnitude in bulk single crystals and three in sputtered thin films—*accompanied by* a strong optical contrast between the highly transmitting insulating phase and the reflective metallic phase. [4] VO_2 couples its electronic and lattice degrees of freedom, undergoing a structural transformation from the high-temperature rutile (R, Figure **1.2a**) to the low-temperature monoclinic (M_1, **1.2b**) phase during the transition. Early anomalies in magnetic susceptibility and thermodynamic measurements made between the 1930s and 1950s hinted at this transition, which was systematically characterized by Morin in 1959. [5–7] Owing to its transition temperature close to ambient conditions and its dramatic electrical–optical switching behavior, VO_2 has become a benchmark system for studying electron–lattice interactions and nonequilibrium phase transitions, while also inspiring diverse applications in smart coatings, infrared detection, optical switching, and neuromorphic computing. [8]

In this chapter, we provide an atomistic explanation of the fundamental origins underlying the macroscopic properties of VO_2 described above. We further review recent advances in the study of its phase transition and present a detailed discussion of its crystal structure, electronic band structure, and potential applications in smart windows.

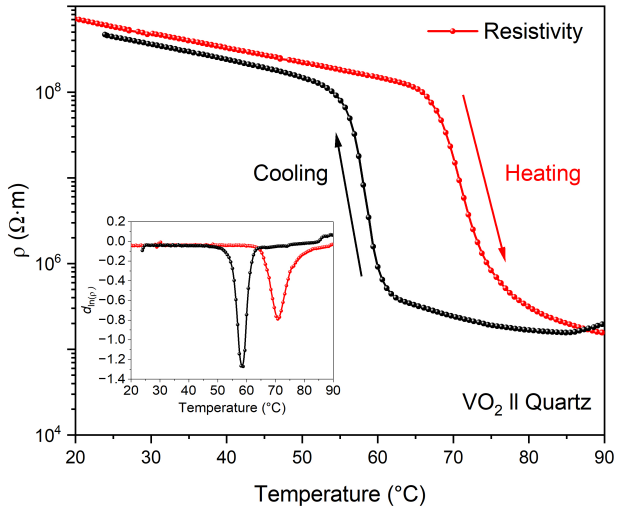

Figure 1.1: Temperature dependence of the resistivity of a VO_2 film deposited on quartz substrate. The inner plot shows the derivative of the logarithm of resistivity.

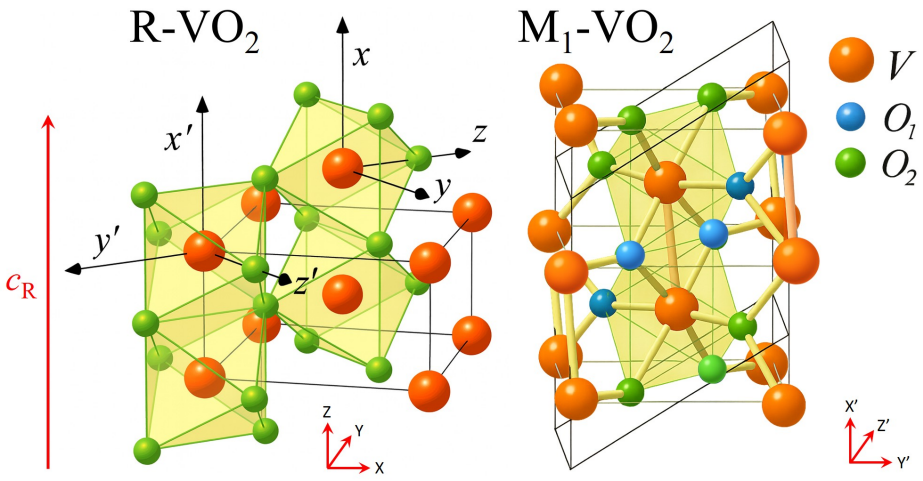

Figure 1.2: (a) R-VO_2 and (b) M_1-VO_2. Adopted from Ref. [9].

1.1 Fundamental Studies of VO_2

1.1.1 Energy-Level Evolution of V 3*d* Orbitals in Octahedral Environments

The ground-state electronic configuration of vanadium (V, atomic number 23) is [Ar] $3d^3 4s^2$, corresponding to five valence electrons in the outermost shell, with three occupying the $3d$ orbitals and two residing in the $4s$ orbital. According to the Aufbau principle, the electron filling sequence generally follows the order $4s$ before $3d$, namely [Ar] $4s^2 3d^3$. [10,11] The reason is that, in terms of actual energy levels, the $3d$ and $4s$ orbitals are nearly degenerate, and the filling order does not strictly follow the simple sequence of principal quantum numbers. [12]

The $3d$ orbitals are characterized by the principal quantum number $n = 3$ and the angular momentum quantum number $l = 2$ (corresponding to d orbitals). The magnetic quantum number m_l takes five possible values (-2, -1, 0, $+1$, $+2$), resulting in five equivalent spatial orientations (see below). [13] According to the Pauli exclusion principle, [14] each orbital can further accommodate two electrons of opposite spin defined by the spin quantum number $m_s = \pm 1/2$. [15]

Beginning with scandium (Sc, $Z = 21$), the transition metal series exhibits the so-called "$3d$ orbital collapse" phenomenon. As the nuclear charge increases, the radial distribution of the $3d$ orbitals contracts significantly, and their energy decreases markedly, causing the $3d$ levels in free atoms to fall below the $4s$ levels. This explains why the $4s$ orbital is filled first in potassium and calcium, whereas for transition metals such as scandium and vanadium, the $3d$ orbitals become more stable. [16,17] Although the single-electron energy of the $3d$ orbital is lower than that of $4s$, in multi-electron atoms the more spatially extended $4s$ orbital becomes energetically favorable due to electron–electron repulsion, resulting in partial occupation in the ground state of neutral atoms. [18]

For neutral vanadium, the ground-state configuration is $3d^3 4s^2$, whereas in the monovalent cation V^+, the configuration becomes $3d^4$, indicating that the $4s$ electron is lost first. Experimental observations confirm that during ionization, the $4s$ electron is removed prior to the $3d$ electrons. [11] Hence, the energy ordering can be summarized as follows: in the case of unoccupied orbitals, the $4s$ level lies slightly below the $3d$ level, but as the $3d$ orbitals become progressively filled and contract, their bound-state energy becomes lower than that of $4s$. The $4s$ electron remains in the valence shell but is more easily ionized. This near-degeneracy of the $3d$ and $4s$ levels also gives rise to irregular electron configurations in certain elements, such as Cr ($3d^5 4s^1$) and Cu ($3d^{10} 4s^1$), reflecting the additional stability associated with half-filled or fully filled $3d$ shells. [17]

The $3d$ orbitals, characterized by $l = 2$, exhibit complex angular distributions and exist in five equivalent orientations, conventionally denoted as $3d_{xy}$, $3d_{xz}$, $3d_{yz}$, $3d_{x^2-y^2}$, and $3d_{3z^2-r^2}$ (commonly abbreviated as $3d_{z^2}$). Among them, four orbitals adopt a cloverleaf-shaped distribution differing only in orientation, while the $3d_{z^2}$ orbital has a distinct "two-lobes-plus-torus" shape, featuring two lobes along the z-axis and a ring around the equatorial plane. [19]

More specifically, the wavefunctions of the $3d$ orbitals (see Figure **1.3**) can be expressed as the product of a radial function $R_{3d}(r)$ and the corresponding Cartesian coordinate factors: [20]

- $3\boldsymbol{d}_{xy}$: proportional to the xy factor, lying in the xy-plane with four lobes oriented between the x and y axes. The nodal planes are yz ($x = 0$) and xz ($y = 0$). The wavefunction is positive (+) in the first and third quadrants ($xy > 0$) and negative (−) in the second and fourth quadrants ($xy < 0$).
- $3\boldsymbol{d}_{xz}$: proportional to xz, distributed in the xz-plane with nodes at yz ($x = 0$) and xy ($z = 0$). The wavefunction is positive (+) where x and z have the same sign, and negative (−) where they have opposite signs.
- $3\boldsymbol{d}_{yz}$: proportional to yz, distributed in the yz-plane with nodes at xz ($y = 0$) and xy ($z = 0$). The wavefunction is positive (+) where y and z have the same sign, and negative (−) where they have opposite signs.
- $3\boldsymbol{d}_{x^2-y^2}$: proportional to $(x^2 - y^2)$, with four lobes directed along the x and y axes; the nodal planes are $x = \pm y$, where the wavefunction changes sign. The lobes along the x-axis are positive (+), while those along the y-axis are negative (−).
- $3\boldsymbol{d}_{3z^2-r^2}$ $(3\boldsymbol{d}_{z^2})$: represented by $(3z^2 - r^2)R(r)$, featuring two lobes along the z-axis and a toroidal ring in the equatorial plane. Unlike the other four d orbitals with planar nodes, the d_{z^2} orbital contains two conical nodal surfaces defined by $3z^2 - r^2 = 0$. The wavefunction is positive (+) in the lobes along the z-axis and negative (−) in the toroidal ring region.

In the metallic rutile phase of VO_2, the V^{4+} ions are uniformly arranged along c axis, with each vanadium ion being approximately octahedrally coordinated by six oxygen atoms, as shown in Figure **1.4**. The crystal as a whole retains the tetragonal symmetry characteristic of the rutile structure. The rutile structure can also be described from an alternative perspective: it may be regarded as a body-centered tetragonal lattice composed of metal atoms, in which each metal atom is surrounded by an oxygen octahedron. The octahedra located at the corners and at the body center of the unit cell are rotated by 90° relative to each other about the rutile c axis, as shown in Figure **1.2a**. As a result, the translational symmetry of the lattice is reduced from body-centered tetragonal to simple tetragonal. Along the rutile c

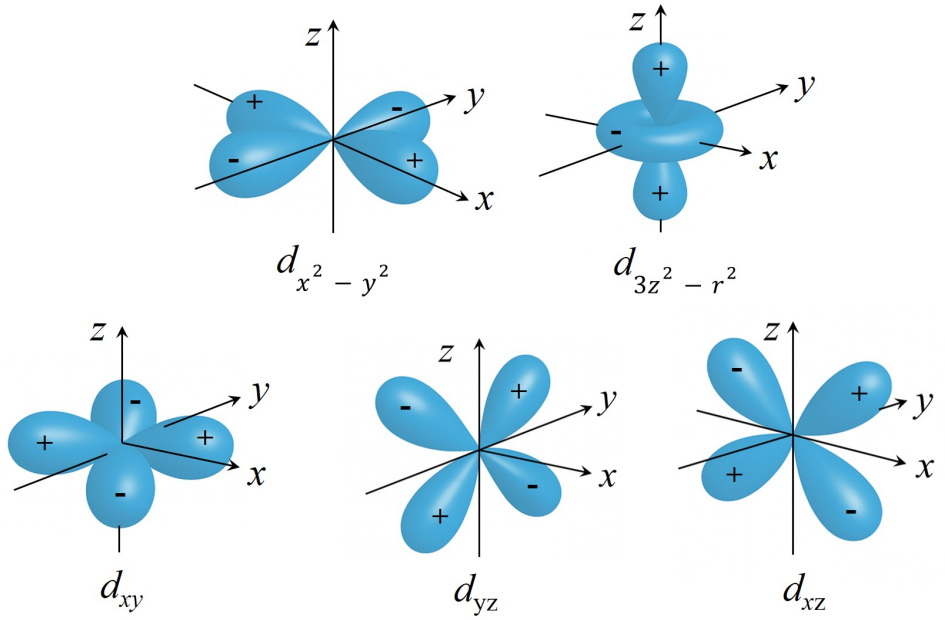

Figure 1.3: Spatial shapes of the five 3*d* atomic orbitals. [20]

axis, adjacent octahedra are connected by edge sharing, while these one-dimensional octahedral chains are further cross-linked through corner sharing. Strictly speaking, each octahedron possesses orthorhombic rather than perfect tetragonal symmetry. However, for most compounds, the deviation from the ideal tetragonal or even cubic geometry is very small, and the structural features can therefore be discussed within an approximately tetragonal or cubic framework. [21]

In rutile VO_2, two distinct types of metal–oxygen bond lengths are observed (see Figure **1.4**):

1. **Apical bond length:** two V–O bonds of 1.92 Å;
2. **Equatorial bond length:** four V–O bonds of 2.03 Å.

The local environment in which each V atom is approximately octahedrally coordinated by six O atoms causes the five V 3*d* orbitals to split under the crystal field into a higher-energy e_g set ($d_{3z^2-r^2}$ and $d_{x^2-y^2}$) and a lower-energy t_{2g} set (d_{xy}, d_{xz}, and d_{yz}). The t_{2g} orbitals remain triply degenerate, and their partial occupation at the Fermi level gives rise to metallic conductivity. This subsection follows the approach of Eyert, using a local coordinate system centered on each metal atom to analyze the atomic orbitals of rutile-type VO_2. [9] These local coordinate systems are indicated in Figure **1.2a**. It should be noted that the octahedra at the corners and at the body center of the unit cell differ in orientation, resulting in an

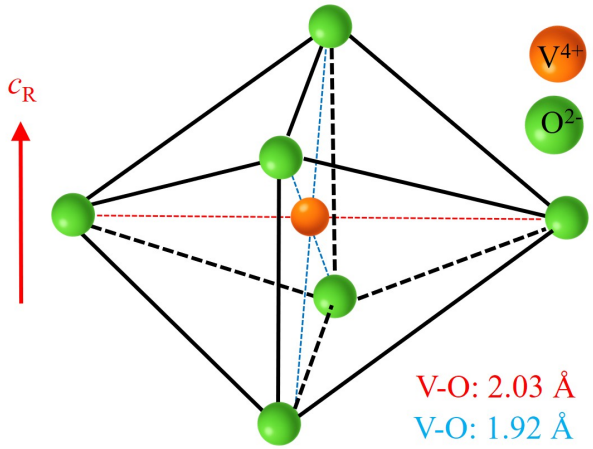

Figure 1.4: Schematic illustration of a V ion in a distorted octahedral crystal field.

alternation of the local z axis between the rutile [110] and rutile [$\bar{1}$10] directions. Unlike the common practice of aligning the x and y axes with the metal–ligand bonds, Eyert rotated the local x and y axes by 45° with respect to the local z axis so that they become parallel and perpendicular, respectively, to the rutile c axis. Consequently, the $d_{x^2-y^2}$ and d_{xy} orbitals exchange their roles, and the d_{yz} orbital becomes aligned with the crystallographic axes of the rutile basal plane.

As shown in Figure **1.5**:

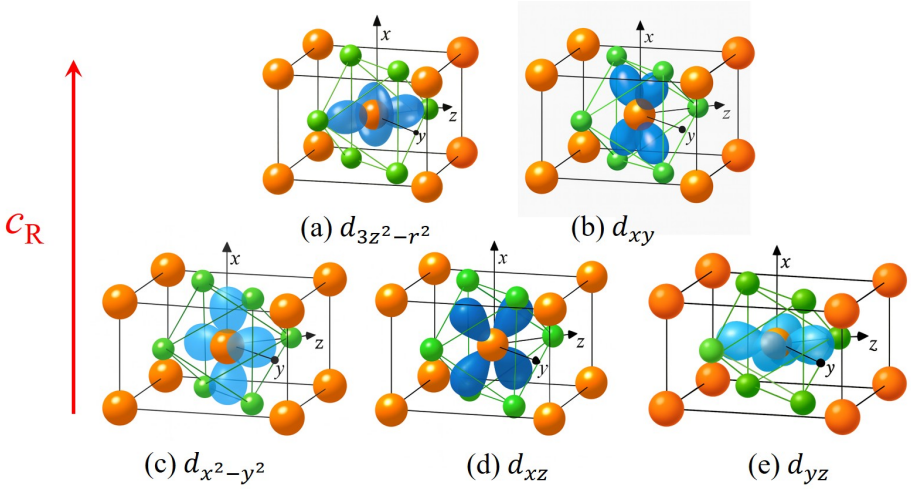

Figure 1.5: Angular parts of the d orbitals. Adopted from Ref. [9].

- The $d_{3z^2-r^2}$ orbital extends along the local z axis, perpendicular to the xy

plane. Its lobes point directly toward the apical oxygen atoms, resulting in a strong σ-type overlap with the O $2p$ orbitals and, consequently, a pronounced σ-bonding–antibonding splitting.

- The d_{xy} orbital lies in the local xy plane, perpendicular to the z axis; its lobes point toward the equatorial oxygen atoms and overlap strongly with the in-plane O–$2p$ orbitals in a σ fashion, leading to pronounced σ-type bonding–antibonding splitting.

- The $d_{x^2-y^2}$ orbital extends along the rutile c axis (the local x axis) and the local y axis, pointing toward the edges of the octahedral basal plane; it directly overlaps (via d–d interactions) with the chain-direction V $3d$ orbitals of the same orientation, shows negligible hybridization with the $2p$ orbitals of the apical oxygen atoms, and thus primarily contributes to σ bonding.

- The d_{xz} orbital is directed toward the faces of the octahedron and participates in π bonding along the direction perpendicular to the chains.

- The d_{yz} orbital points along the rutile $\langle 100 \rangle$ direction; after the 45° rotation of the local coordinate system, it becomes aligned with the basal-plane axes, where its lobes hybridize with the in-plane O–$2p$ orbitals through π-type overlap, thereby contributing to weaker π bonding channels.

According to the Goodenough model, the $3d$ orbitals of V^{4+} ions located at octahedral coordination sites are split by the cubic component of the crystal field into a higher-energy doubly degenerate E_g state and a lower-energy triply degenerate T_{2g} state. Because neighboring octahedra share edges along the c_R axis, the orthorhombic lattice distortion completely removes the residual degeneracy of the d orbitals. [22]

As illustrated in Figure **1.6**, in R-VO_2, the V $3d_{3z^2-r^2}$ orbital points along the local z-axis toward the apical O atoms and forms a strong $d_{3z^2-r^2}$–p σ-type hybridization with the O $2p$ orbitals. Similarly, the V $3d_{xy}$ orbital, oriented toward the equatorial O atoms in the basal plane, also engages in σ-type hybridization with the O $2p$ orbitals, resulting in the formation of σ and σ^* bonds. Under the periodic potential of the crystal, σ bands form below the Fermi level, while σ^* bands appear above it. [9]

The V $3d_{x^2-y^2}$ orbital is oriented along the c axis and directly overlaps with orbitals of the same orientation through $d_{x^2-y^2}$–$d_{x^2-y^2}$ σ-type interactions, forming σ bonds. This orbital exhibits negligible hybridization with the $2p$ orbitals of the apical oxygen atoms and, under the periodic crystal potential, gives rise to the $d_{\|}$ band of VO_2. [9]

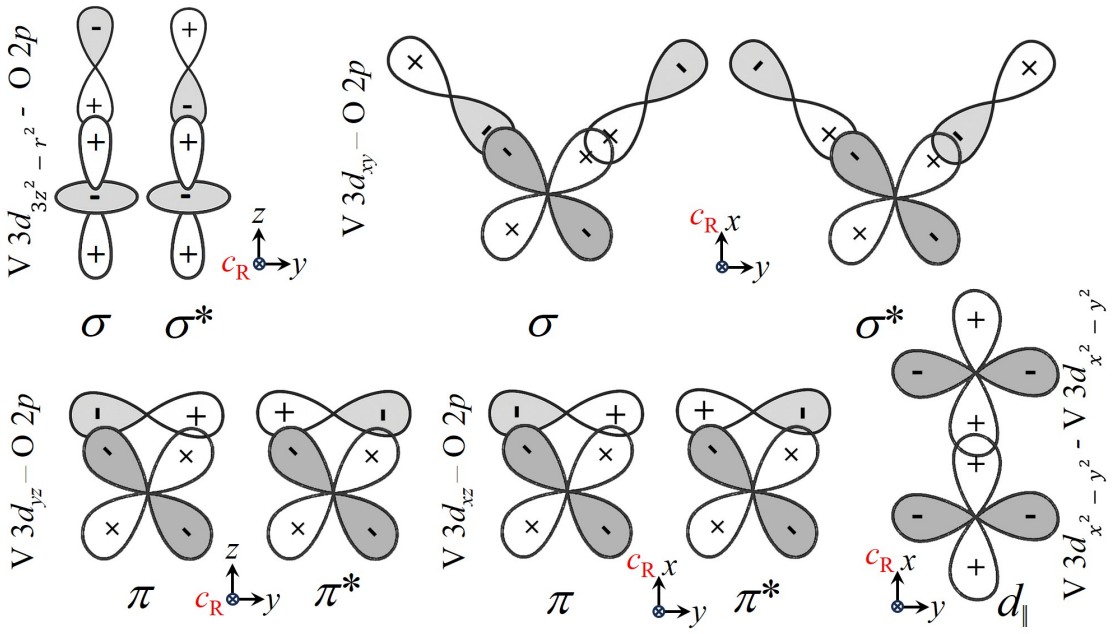

Figure 1.6: Orbital-overlap model of V–O bonding in rutile VO_2.

In addition, the V $3d_{xz}$ orbital forms a d_{xz}–p π-type overlap with the O $2p$ orbitals, while the $3d_{yz}$ orbital forms a d_{yz}–p π-type overlap, corresponding to the formation of π and π^* bonds, respectively. Through the periodic potential of the crystal, π bands are established below the Fermi level, and π^* bands emerge near the Fermi level. The π^* bands are mainly consists of contributions from V $3d$ orbitals, less from by the O $2p$ orbitals. Because V^{4+} possesses only a single $3d$ electron, the $d_{x^2-y^2}$, d_{yz}, and d_{xz} orbitals cannot be fully occupied, leading to an overlap between the $d_\parallel$ and π^* bands, both of which are intersected by the Fermi level. Consequently, the $d_\parallel$ and π^* bands are both distributed in the vicinity of the Fermi level. [9]

Upon cooling, the structure of VO_2 transforms into the monoclinic M_1 phase, in which vanadium atoms dimerize along the c-axis, and the $d_\parallel$ band undergoes strong splitting at the upper and lower edges of the t_{2g} band manifold, forming two narrow subbands corresponding to bonding and antibonding $d_\parallel$ states. The VO_6 octahedra experience a slight tilting, thereby breaking the original symmetry and enhancing the overlap between metal and oxygen orbitals. The π^* band are collectively shifted to higher energies as a consequence of the reduced V–O distances.

The transition of the electronic band structure described above is illustrated schematically in Figure **1.7**.

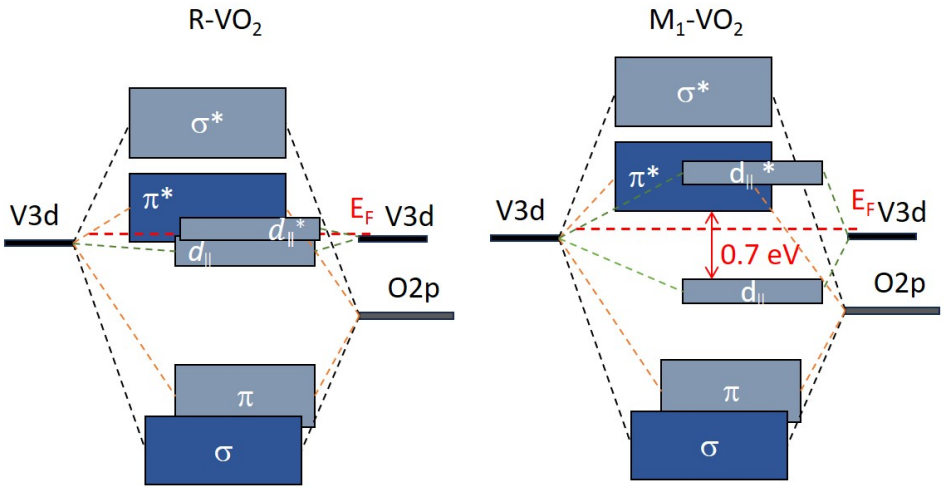

Figure 1.7: Temperature-Induced Orbital Reconstruction and Band Splitting Across the Metal–Insulator Transition in VO_2. [22]

1.1.2 Mechanisms of the Metal–Insulator Transition

Despite the early discovery of the MIT in VO_2 already in 1959, the fundamental mechanism driving the MIT in VO_2 remains a topic of active debate. The key question is whether the insulating phase arises primarily from electron–electron interactions, as described by the Mott mechanism, or from lattice distortions that induce band gap opening through Peierls-like instabilities. These two perspectives offer distinct physical pictures: the Mott mechanism emphasizes Coulomb repulsion and electronic correlation in narrow bands, while the Peierls mechanism highlights periodic lattice distortions that split degenerate bands due to symmetry reduction. The challenge lies in disentangling the contributions of these coexisting effects, as both structural and electronic changes are observed near the transition temperature and are usually entangled. [4, 9]

The Mott scenario gained prominence following Mott's 1968 review, in which he identified VO_2 as a strongly correlated electron system. [23] In the high-temperature rutile phase, VO_2 exhibits relatively low electrical conductivity and paramagnetic behavior, inconsistent with a conventional metal. Mott argued that the conduction band in VO_2 must be narrow enough that Coulomb repulsion localizes the electrons, resulting in a correlation-induced insulating state. He further proposed that charge carriers may exist as small polarons—thermally activated electron–hole pairs (V^{4+}/V^{5+}) that are localized by lattice polarization. In this model, the insulating behavior is not simply a result of band structure rearrangement but stems from many-body electron interactions. This interpretation challenged the earlier

purely structural model (i.e., the metal–insulator transition in VO_2 is attributed to a lattice distortion driven by vanadium atom dimerization along the rutile *c*-axis, which lifts the degeneracy of electronic bands and opens a band gap, thereby leading to the formation of an insulating state) and suggested that VO_2 might reside on the insulating side of the Mott transition even in its nominally metallic state.

In contrast, Adler and Brooks proposed a band-theoretical model in 1967 that offered a thermodynamic framework for the semiconductor-to-metal transition [24]. Their theory predicted a linear decrease of the energy gap with increasing carrier concentration, culminating in a discontinuous collapse at a critical threshold. Depending on material-specific parameters, this transition could be either first- or second-order. They considered both antiferromagnetic-induced band splitting and structural distortion as potential mechanisms. Among these, the structural distortion model showed better agreement with experiments, emphasizing the crucial role of lattice symmetry breaking in modifying the electronic structure. The model also provided quantitative relationships for predicting physical observables such as transition temperature and pressure dependence.

Experimental evidence supporting the structural viewpoint came from optical studies by Verleur et al. in 1968, who analyzed the complex dielectric function of VO_2 thin films and single crystals over a wide photon energy range [25]. They observed a distinct optical band gap of $\sim$0.6 eV in the insulating phase, and a pronounced spectral shift near the transition temperature, indicating band gap closure during the MIT. Similarly, Berglund and Guggenheim systematically measured electrical and optical properties across the transition and associated the gap formation with V–V dimerization—a structural feature indicative of Peierls distortion [26]. This suggested that periodic lattice distortions could indeed split the *d* bands and open a gap, lending strong support to the Peierls mechanism.

However, subsequent structural investigations on doped systems provided more nuanced insights. Marezio et al. (1972) discovered two intermediate monoclinic phases (M_2 and T) in Cr-doped VO_2, revealing a multi-stage transition pathway from rutile to M_1 via partially dimerized states [27]. In the M_2 phase, only half of the vanadium atoms form dimers, while others remain undimerized, forming zigzag chains. Notably, the system remains insulating in this phase, implying that dimerization alone cannot fully account for the MIT. Complementary work by Pouget and Launois confirmed the existence of the M_2 phase and emphasized that electron localization persists even without full V–V pairing [28]. These findings provided compelling evidence that the MIT arises from a cooperative interplay between structural distortions and electronic correlations.

This correlation was also discussed by Goodenough in 1971, he proposed that two simultaneous processes drive the MIT: (i) a transition from antiferroelectric to paraelectric order associated with V–V pairing, and (ii) the formation of metallic

V–V bonds corresponding to a shift from covalent to itinerant bonding. [22] His band theory interpretation illustrated how temperature-induced lattice distortions modulate the overlap between vanadium d and π bands, leading to band splitting at low temperatures and band merging at high temperatures. This band evolution accounts for the insulating-to-metallic transition in terms of both orbital hybridization and structural transformation. As depicted in Figure **1.7**, the schematic orbital-resolved band diagrams of the R and M_1 phases of VO_2, the V $3d$ orbitals hybridize with O $2p$ orbitals to form bonding (σ, π) and antibonding (σ^*, π^*) orbitals which form the bands denoted as σ, π, σ^* and π^* bands. Furthermore, some V $3d$ orbitals, specifically $d_{x^2-y^2}$ form σ like bonding and antibonding, V-V orbitals along the c_R yielding the so called $d_\parallel$ and $d_{\parallel^*}$ bands. In the high-temperature rutile phase, the undimerized vanadium chains allow the partially filled $d_\parallel$ and π^* bands to overlap near the Fermi level, resulting in metallic conductivity. Upon cooling, structural dimerization along the c-axis induces a bonding–antibonding splitting of the $d_\parallel$ states, opening an energy gap of $\sim$0.7 eV in the M_1 phase. This orbital reconfiguration localizes the electrons within the lower-energy $d_\parallel$ subband, leading to an insulating ground state. The transition thus reflects a cooperative mechanism involving Peierls-type lattice distortion and covalent-to-itinerant electronic reorganization. The specific physical picture has been described earlier.

The notion of a dual mechanism was also supported by Zylbersztejn and Mott in 1975, who argued that neither Mott nor Peierls effects alone could explain the full transition. [4] Instead, they proposed a correlation-assisted Peierls transition, wherein structural distortions enhance the effect of electron correlations by modifying the bandwidth and effective Hubbard U (on-site Coulomb interaction energy). Their conclusion was based on doping and magnetic susceptibility experiments, which showed that while the low-temperature phase is correlated and gapped, the high-temperature phase behaves as a weakly correlated metal with delocalized carriers.

Later, time-resolved studies by Brorson et al. (1994) revealed that under femtosecond laser excitation, VO_2 could undergo an ultrafast transition to a metallic state within a few hundred femtoseconds. [29] Remarkably, the electronic change—band gap collapse—preceded any observable structural change, indicating that the MIT can be triggered purely electronically under nonequilibrium conditions. This transient metallic state emphasized the dynamical role of electronic correlations and demonstrated that structural distortions, while important at equilibrium, are not strictly necessary to initiate the transition.

Theoretical advances in the 1990s further supported this viewpoint. Wentzcovitch et al. used density functional theory (DFT) with local density approximation (LDA) to calculate the electronic structure of VO_2 and found that the experimentally observed lattice distortion was insufficient to open the band gap [30]. Their

simulations predicted a metallic state even in the monoclinic structure, suggesting that electron correlation must be included to reproduce the insulating behavior. This prompted the application of the LDA+DMFT (Dynamical Mean-Field Theory) method by Biermann et al. [31], who demonstrated that V–V dimers in the insulating phase form a "dynamical singlet"—a correlated bonding state that stabilizes the gap. Their work showed that while Peierls distortion splits the bands, only strong dynamic correlations explain the gap magnitude and insulating character, thus reinforcing the idea of a correlation-assisted Peierls transition.

Recent experimental studies have continued to refine this cooperative picture. Qazilbash et al. employed near-field infrared imaging and spectroscopy to visualize metallic domains during the MIT at nanometer scales [32]. They observed divergence in the optical effective mass and evidence of a pseudogap, consistent with Mott physics. More importantly, the electronic transition preceded the structural transformation, indicating that correlations dominate the initial stage of the transition. In parallel, Budai et al. used neutron and X-ray scattering combined with first-principles calculations to show that phonon entropy plays a critical role in driving the transition [33]. They found that the rutile phase exhibits strongly anharmonic lattice vibrations, contributing significantly to the entropy gain and stabilizing the metallic phase. This highlighted the thermodynamic complexity of the MIT, wherein lattice dynamics and entropy compete with orbital ordering and electron correlation.

Most recently, Tao et al. used ultrafast electron diffraction and transmission electron microscopy to decouple the structural and electronic transitions in VO_2 [34]. They discovered a novel monoclinic metallic phase (M_3), accessible by substrate engineering and optical excitation, in which the system remains metallic despite retaining monoclinic symmetry. This decoupling confirms that the structural transformation is not a strict prerequisite for the electronic transition and reinforces the view that the MIT is fundamentally driven by electronic correlations, with lattice distortion playing a secondary, modulating role.

In summary, decades of research have revealed that the MIT in VO_2 is governed by a complex interplay between electron correlation, lattice distortion, orbital hybridization, and thermodynamic effects. Neither a purely Peierls nor a purely Mott model can fully account for the transition. Instead, VO_2 exemplifies a "correlation-assisted Peierls transition," in which both electronic and structural degrees of freedom cooperate to produce the observed phenomena. This rich coupling makes VO_2 a model system for studying emergent behavior in strongly correlated materials and continues to inspire novel experimental and theoretical investigations.

1.1.3 Crystal Structure and Electronic Band Structure

Although the mechanism underlying the metal–insulator transition in VO_2 remains debated, there is broad consensus regarding its crystallographic and electronic structure. In the preceding section, we briefly reviewed the structural and electronic characteristics of VO_2 and outlined key aspects of the transition mechanism. Here, we focus on the R and M_1 phases of VO_2 employed in our experiments, and elucidate the correlation between their crystallographic configurations and electronic band structures. We further establish the connection between their electronic band structures and macroscopic properties such as electrical conductivity, optical transmittance, and color appearance.

In addition to the well-established monoclinic M_1 and rutile R phases [35], VO_2 can also stabilize into several other polymorphs under doping or applied strain. These include the monoclinic M_2 phase [27], the triclinic T phase [27], and the metastable M_3 phase [34], which can be induced by photoexcitation. The M_2 and T phases are generally considered intermediate structures along the $M_1 \rightarrow R$ phase transition pathway, while the M_3 phase exhibits metallic behavior under non-equilibrium conditions and is not discussed further in this work. Representative lattice parameters of these phases are listed in Table **1.1**; however, it should be noted that the parameters of the M_2 and T phases are sensitive to dopant concentration and strain conditions, and the values provided are typical examples.

Table 1.1: Lattice parameters of different VO_2 phases (including α and γ).

Phase	a (Å)	b (Å)	c (Å)	α (°)	β (°)	γ (°)	V (Å^3)	**Reference**
M_1-VO_2	5.7517	4.5378	5.3825	90.00	122.646	90.00	118.29	[35]
T-VO_2 ($V_{0.976}Cr_{0.024}O_2$)	9.1650	5.7970	4.5220	—	92.14	—	239.0	[27]
M_2-VO_2 ($V_{0.976}Cr_{0.024}O_2$)	9.0664	5.7970	4.5255	90.00	91.88	90.00	237.5	[27]
B-VO_2	12.030	3.6930	6.4200	90.00	106.10	90.00	274.033	[36]
R-VO_2	4.5546	4.5546	2.8514	90.00	90.00	90.00	59.15	[35]

The phase transition pathways of VO_2 are known to be diverse. Reported sequences include: $M_1 \rightarrow R$, $M_1 \rightarrow M_2 \rightarrow R$, $M_1 \rightarrow T \rightarrow M_2 \rightarrow R$, $M_2 \rightarrow R$, and $T \rightarrow R$. [27,37] Despite the differences in transition pathways, VO_2 invariably transforms into the metallic rutile R phase upon heating above the critical temperature (T_c), characterized by its tetragonal symmetry.

In contrast to the M_1–R transition, which involves both structural and electronic reconstruction, the B phase of VO_2 retains its monoclinic structure throughout the thermal cycle. While minor changes in lattice parameters occur with temperature, no first-order structural phase transition is observed. The electrical resistivity of B-VO_2 decreases nearly linearly with increasing temperature, showing no abrupt

change characteristic of a metal–insulator transition, and instead exhibiting a continuous semiconducting behavior. [38]

Among all known phases, the M_1 and R structures are the most extensively studied. As illustrated in Figure **1.2**, under ambient pressure and above T_c, VO_2 adopts a tetragonal rutile structure (space group $P4_2/mnm$), with lattice constants $a = b = 4.55$ Å and $c = 2.85$ Å. [35] Below T_c, unstrained and stoichiometric VO_2 crystals switch to the monoclinic M_1 phase (space group $P2_1/c$), with lattice parameters $a = 5.75$ Å, $b = 4.54$ Å, $c = 5.38$ Å, and $\beta = 122.6°$. [35] Compared to the R phase, the M_1 unit cell doubles in volume and features V–V dimerization along the rutile c-axis direction, accompanied by a zigzag distortion of the vanadium chains. The dimerization results in alternating V–V bond lengths of 2.65 Å (short) and 3.12 Å (long) [39], in contrast to the equidistant V–V spacing in the R phase.

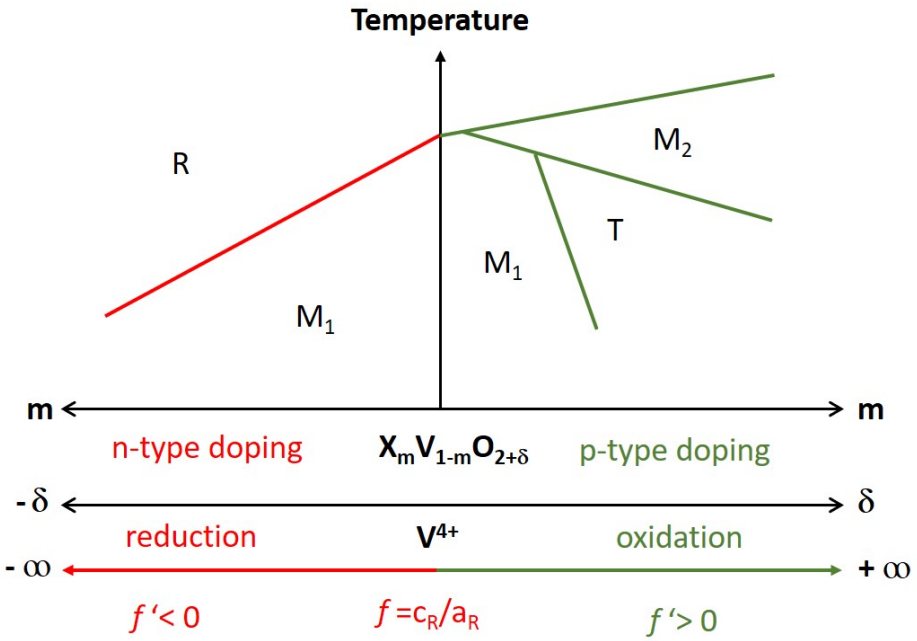

Figure 1.8: Generalized phase diagram of VO_2 under combined doping, stoichiometry, and strain control. Adopted from Ref. [37].

Beyond the M_1–R transformation, VO_2 exhibits a range of competing phases, resulting in a rich structural phase diagram. [37] Figure **1.8** presents a generalized phase diagram of VO_2, mapping its diverse phase transition pathways and complex structural evolution under varying temperature and external control parameters. The vertical axis denotes temperature, while the horizontal axis represents a synthetic control parameter encompassing doping type, stoichiometry deviation, and lattice

strain. Under ambient (unperturbed) conditions—corresponding to the central axis of the diagram—VO_2 typically undergoes a direct M_1–R phase transition.

The left side of the diagram corresponds to conditions such as n-type doping, oxygen-deficient films (i.e., $\delta < 0$, indicating a reduced V^{4+} valence state), and compressive lattice strain ($f' < 0$). Under these circumstances, the material tends to stabilize within the M_1–R two-phase region, and the T_c decreases with increasing control strength, resulting in a well-defined metal–insulator transition. In contrast, the right side of the diagram corresponds to p-type doping, oxygen-rich films (i.e., $\delta > 0$, indicating oxidation toward V^{5+}), and tensile lattice strain ($f' > 0$). These conditions promote the formation of intermediate phases such as M_2 and T, leading to multistage transition pathways, including $M_1 \rightarrow T \rightarrow M_2 \rightarrow R$ or $M_1 \rightarrow M_2 \rightarrow R$. These intermediate states generally require external doping or strain engineering to become thermodynamically stable near room temperature, and their corresponding transition temperatures tend to increase with increasing control strength.

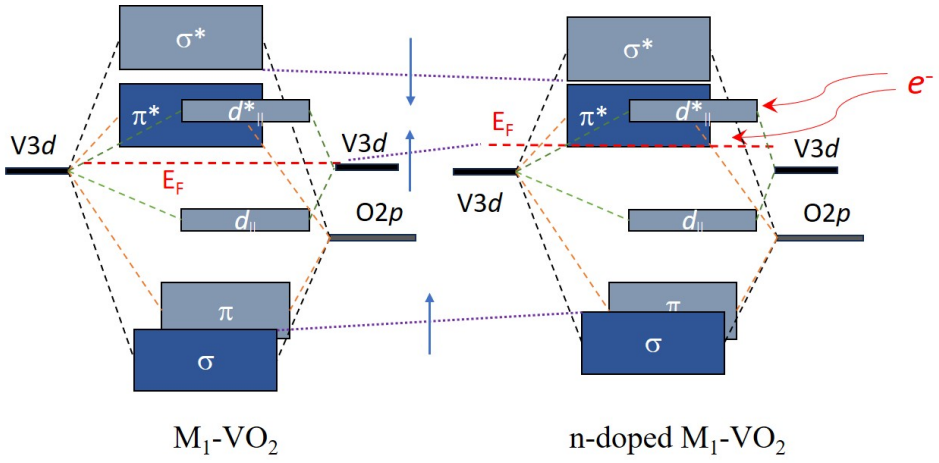

Figure 1.9: Schematic diagram of the electronic band structure of M_1-VO_2 during n-type doping

Without considering external stress, n-type doping of M_1-phase VO_2 essentially introduces additional electrons into the vanadium $3d$ $d_{x^2-y^2}$ orbitals. As shown in Figure **1.9**, this extra electron filling further populates the $d_{\parallel}^*$ (antibonding $d_{\parallel}$) states derived from $d_{x^2-y^2}$, enhancing the direct V–V orbital overlap and driving the $d_{\parallel}^*$ band to lower energies, thereby reducing the bonding–antibonding splitting of the $d_{\parallel}$ states. At high doping concentrations, the vanadium $3d_{xz}$ and $3d_{yz}$ orbitals may also become occupied, leading to additional filling of the π^* states derived from these orbitals and causing an upward shift of the Fermi level. As the doping level increases, the Fermi energy gradually enters the π^* bands and may even penetrate into the $d_{\parallel}^*$ band, thereby strengthening the metallic character.

n-type doping also weakens the hybridization between the vanadium $3d$ and oxygen $2p$ orbitals, reducing the overlap of their electronic wavefunctions. Consequently, the bonding σ bands shift slightly upward in energy, while the corresponding antibonding σ^* bands move downward. This band-level effect provides an explanation for the experimentally observed reduction of the metal–insulator transition temperature (T_c) in n-doped VO_2.

By contrast, p-type doping in VO_2 mainly removes electrons from the $d_{\|}$ band. Such hole doping weakens V–O hybridization, slightly lowers the energies of the bonding σ and π states, and simultaneously shifts the antibonding σ^* and π^* states downward. As the $d_{\|}$ band becomes less occupied and approaches half-filling, the Peierls instability along the vanadium chains is enhanced, leading to stronger bonding–antibonding splitting and driving the system toward insulating monoclinic phases (M_1 or M_2). Consequently, the Fermi level moves deeper into the $d_{\|}$ band, the overall bandwidth narrows, and the T_c is not reduced and may even increase. And oxygen vacancy engineering in VO_2 can be regarded as an intrinsic form of n- and p-type doping in the material.

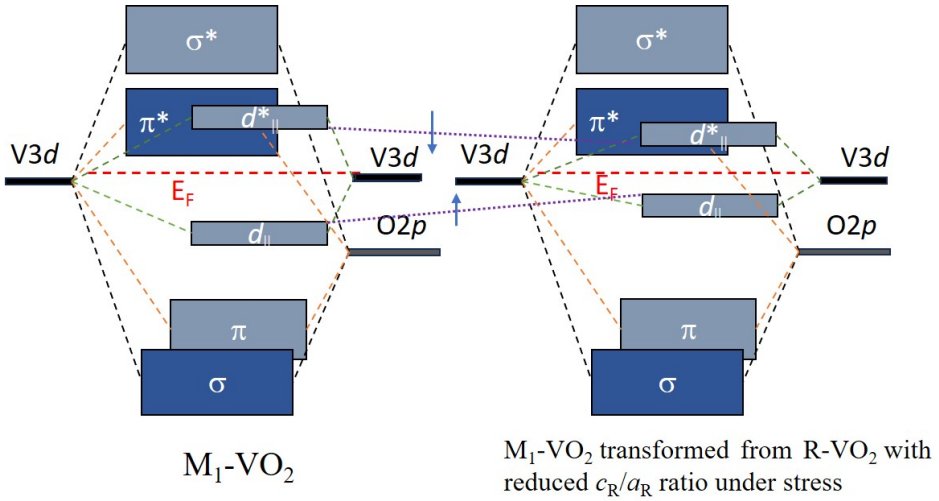

Figure 1.10: Schematic diagram of the electronic band structure of M_1-VO_2 transformed from R-VO_2 with reduced c_R/a_R ratio under stress

In stress regulation, when the ratio c_R/a_R decreases (corresponding to compression along the rutile c-axis or in-plane tension), the V–V spacing along the vanadium chains shortens. This shortening enhances the overlap of the $d_{x^2-y^2}$, d_{xz}, and d_{yz} orbitals, thereby strengthening both the direct V–V orbital overlap and V $3d$ – O $2p$ σ/π hybridization. As a consequence, the bandwidths of the π^* and $d_{\|}$ bands increase. When VO_2 transforms from the rutile phase to the monoclinic M_1 phase under these conditions, the splitting of the $d_{\|}$ orbitals becomes smaller; specifically,

the $d_{\parallel}^{*}$ (antibonding) level shifts downward, while the $d_{\parallel}$ (bonding) level shifts upward. The energy separation between $d_{\parallel}$ and π^{*} thus decreases, and the system becomes more metallic. Figure **1.10** illustrates the electronic band structure of M_1-VO_2 before and after this stress regulation.

Tensile strain produces the opposite effect. When c_R/a_R increases, the V–V spacing along the chain increases, weakening the overlap of the $d_{x^2-y^2}$, d_{xz}, and d_{yz} orbitals. This reduces the direct V–V orbital overlap as well as the V,3d–O,2p σ/π hybridization, leading to narrower π^{*} and $d_{\parallel}$ bandwidths. During the R-to-M_1 transition under these conditions, the splitting of the $d_{\parallel}$ orbitals becomes larger; that is, the $d_{\parallel}^{*}$ level shifts upward, while the $d_{\parallel}$ level moves downward. The energy separation between $d_{\parallel}$ and π^{*} therefore increases, enhancing the insulating character of the system.

In our previous study [35], we investigated the structural phase transition from the monoclinic M_1 phase to the rutile R phase in Ti-doped VO_2. Considering the emergence of 180° rotational domains during this transformation, the lattice correspondence between the M_1 and R phases can be summarized as follows:

$$
\begin{aligned}
\vec{a}^{1}_{\mathrm{M_1}} &\approx 2\vec{c}_R \parallel z \parallel x'_1 \\
\vec{b}^{1}_{\mathrm{M_1}} &\approx \vec{a}_R \parallel x \parallel y'_1 \\
\vec{c}^{1}_{\mathrm{M_1}} &\nparallel \vec{b}_R \parallel y \parallel z'_1 \\
\vec{a}^{2}_{\mathrm{M_1}} &\approx -2\vec{c}_R \parallel -z \parallel x'_2 \\
\vec{b}^{2}_{\mathrm{M_1}} &\approx -\vec{b}_R \parallel -y \parallel y'_2 \\
\vec{c}^{2}_{\mathrm{M_1}} &\nparallel -\vec{a}_R \parallel -x \parallel z'_2
\end{aligned}
$$

The transformation from the Cartesian coordinate system of each monoclinic domain to that of the rutile lattice can be formally expressed as:

$$
\begin{pmatrix} x'_i \\ y'_i \\ z'_i \end{pmatrix} = I_i \begin{pmatrix} x \\ y \\ z \end{pmatrix}, \tag{1.1}
$$

where the transformation matrices I_i are given by:

$$
I_1 = \begin{pmatrix} 0 & 0 & 1 \\ 1 & 0 & 0 \\ 0 & 1 & 0 \end{pmatrix}, \quad I_2 = \begin{pmatrix} 0 & 0 & -1 \\ 0 & -1 & 0 \\ -1 & 0 & 0 \end{pmatrix}. \tag{1.2}
$$

An analogous transformation relationship also holds for the structural transition from undoped M_1-VO_2 to R-VO_2.

The lattice distortion from the rutile to the monoclinic M_1 phase observed in VO_2 is not unique; similar structural transitions are found in other transition metal dioxides, including NbO_2, MoO_2, WO_2, TcO_2, and α-ReO_2, see table **1.2**. [40] As illustrated in Figure **1.11**, these compounds exhibit pronounced metal–metal bonding interactions that promote the formation of metal–metal dimers along the c-axis of the rutile framework. Concurrently, atoms undergo zigzag-like lateral displacements perpendicular to the chain direction. This cooperative distortion gives rise to the monoclinic M_1 structure, whose unit cell volume doubles that of the parent rutile phase. Notably, all six dioxides display an unusually small ratio of rutile lattice constants c_R/a_R, indicating a structural predisposition toward metal–metal pairing and lattice instability. [9]

Table 1.2: Crystallographic parameters of rutile-related dioxides.

Compound	a (Å)	b (Å)	c (Å)	β (°)	V (Å^3)	c/a	Closest M–M (Å)
VO_2 (R)	4.554	—	2.851	—	58.97	0.625	2.85
VO_2 (M_1)	5.7517	4.5278	5.3825	122.65	59.00	0.626	2.62
NbO_2	13.690	5.9871	5.9871	—	70.13	0.618	2.80
MoO_2	5.6109	4.8562	5.6285	120.95	65.76	0.577	2.51
WO_2	5.5607	4.9006	5.6631	120.44	66.53	0.567	2.49
TcO_2	5.55	4.85	5.62	121.9	64.20	0.586	—
α-ReO_2	5.562	4.838	5.561	120.87	64.25	0.576	2.49

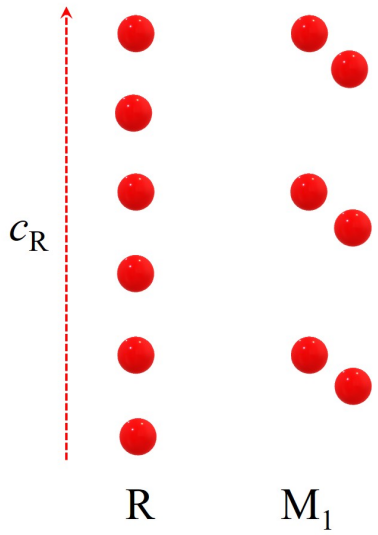

Figure 1.11: Schematic illustration of V–V dimerization along the c-axis in the rutile structure of VO_2.

Despite the pronounced structural similarities among the six aforementioned dioxides, their electronic properties differ markedly. Notably, only VO_2 and NbO_2—both characterized by a d^1 electronic configuration—undergo a metal–insulator transition. [21]

While the crystallographic aspects of this transition are now well established, the corresponding changes in the electronic structure are equally crucial for understanding the physical properties of VO_2.

The electronic structure of metallic VO_2 has been extensively investigated through a wide range of optical absorption and photoemission spectroscopy experiments. Based on the experimental findings reported in multiple references, we present in Figure **1.12** shows a schematic illustration of its band structure, explicitly annotated with the corresponding band width value. [41–44] To clearly differentiate the respective contributions of oxygen and vanadium to the electronic bands, a simplified representation is adopted. Although the diagram slightly differs in form from Fig. 1.4, it is nonetheless derived from the same physical framework originally proposed by Goodenough in his band theory of VO_2.

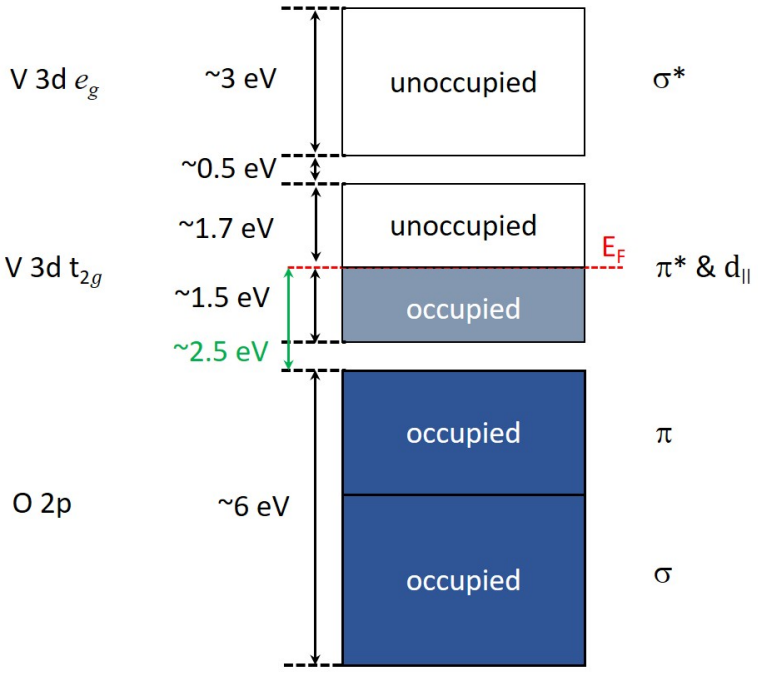

Figure 1.12: Schematic electronic band structure of metallic VO_2. Adopted from Ref. [22]

As mentioned before, in a nearly ideal cubic octahedral coordination environment, hybridization between the oxygen $2p$ and vanadium $3d$ orbitals gives rise to both

σ- and π-type overlap. Due to the significantly stronger p–d interaction in the σ configuration, the bonding–antibonding splitting between the σ/σ^* states is substantially larger than that of the π/π^* states. Although the σ and π bonding states originate from p–d hybridization, their electronic character is predominantly oxygen $2p$. In contrast, the corresponding antibonding states are mainly derived from the vanadium $3d$ orbitals. Specifically, the σ^* states arise from out-of-phase overlap between O $2p$ and V $3d$ orbitals, primarily involving the V e_g orbitals (such as d_{z^2} and d_{xy}), while the π^* states are formed mainly by the V t_{2g} orbitals (including d_{xz}, d_{yz}, and $d_{x^2-y^2}$). These π^* states exhibit a dominant V $3d$ character and are responsible for the metallic nature of the system. [21]

Although the oxygen octahedra in VO_2 exhibit only minor orthorhombic distortions, such subtle structural perturbations are sufficient to lift the degeneracy of the d orbitals from the ideal octahedral crystal field, leading to nontrivial modifications of the electronic band structure. As originally emphasized by Goodenough [22, 45], the d-derived electronic bands in VO_2 are governed not only by the p–d hybridization between O $2p$ and V $3d$ orbitals, but also by strong direct metal–metal interactions. In the rutile structure, the $d_{x^2-y^2}$ orbitals exhibit pronounced overlap along the c-axis, acting as the principal channel for V–V bonding, playing a central role in the metallic phase. [21]

In contrast, the d_{xz} orbital shows negligible overlap with neighboring metal sites and thus contributes little to intersite coupling. On the other hand, the d_{yz} orbital mediates effective metal–metal interactions within the basal plane of the tetragonal lattice, facilitating electronic transport continuity in the in-plane directions. [21]

As shown in the Figure **1.12**, the total occupied bandwidth of R-VO_2 spans approximately 8.5 eV, comprising a narrow V $3d$ band of about 1.5 eV and a broader O $2p$ band of roughly 6 eV. The unoccupied V $3d$ states are primarily distributed in two distinct energy regions: one ranging from the Fermi level up to approximately 1.7 eV, and the other extending from 2.2 eV to 5.2 eV. Optical measurements reveal that the lowest unoccupied V $3d$ states lie approximately 2.5 eV above the top of the O $2p$ band. [21, 41–44]

A clear understanding of the electronic structure of the M_1 phase of VO_2 can be achieved by referencing the well-established band structure of the R phase. Upon undergoing the metal–insulator transition, the octahedral crystal field surrounding V^{4+} ions in R-VO_2 becomes distorted due to the formation of V–V dimers. This distortion induces a splitting of the $d_{\|}$ band. According to literature reports, the total splitting of the $d_{\|}$ band is approximately 2.5 eV, comprising a 0.9 eV energy difference from the valence band maximum to the Fermi level, a 0.5 eV upward shift of the conduction band, and a 1.1 eV separation between the bottom of the $d_{\|}$ conduction band and the π^* conduction band. Experimental data further indicate that the energy difference between the Fermi level and the top of the $d_{\|}$ valence

band is about 0.2 eV, and the bandwidth of the $d_{\|}$ states is roughly 1.5 eV. In addition, the gap between the top of the $d_{\|}$ valence band and the bottom of the π^* conduction band is estimated to be around 0.65 eV. These key features collectively define the electronic band structure of the insulating M_1 phase, as schematically illustrated in Figure **1.13**. [41]

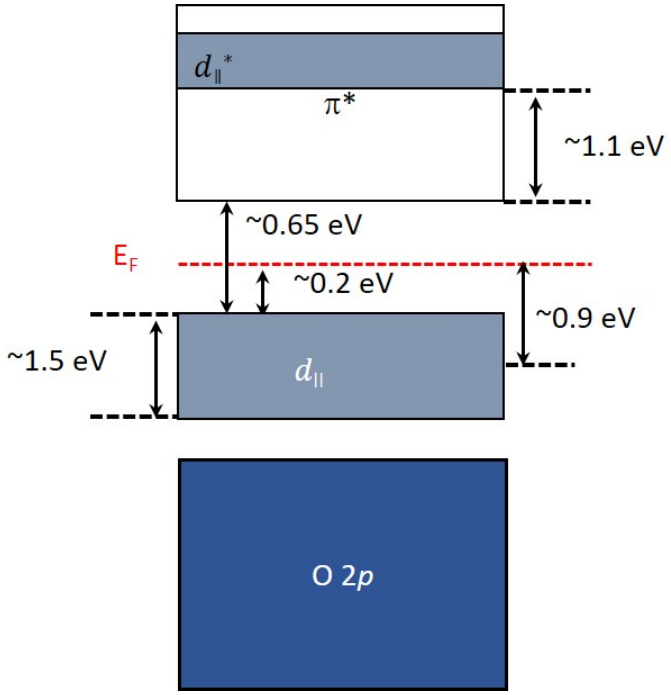

Figure 1.13: Schematic electronic band structure of M_1-VO_2.

The macroscopic properties of VO_2 can be directly traced back to its underlying electronic band structure. In the metallic rutile phase, VO_2 exhibits strong reflection and weak absorption in the infrared region while maintaining high transmittance in the visible range. This behavior can be understood in terms of its band structure and the response of free carriers across different photon energies. [25]

The macroscopic optical properties of VO_2 can be explained along those lines. In the metallic rutile phase, VO_2 exhibits strong reflectance or absorption in the infrared (IR) region while maintaining high transmittance in the visible spectrum. This behavior can be understood by examining its band structure and the collective response of free carriers. [46]

Specifically, in the R phase, the V $3d$ orbitals—predominantly the π^* and $d_{\|}^*$ states—form partially filled conduction bands through p–d hybridization and d-d hybridization, respectively. The Fermi level intersects the π^* band, imparting

metallicity and giving rise to free carriers. The optical response of these free electrons is well described by the Drude model, in which the complex dielectric function is given by:

$$\varepsilon(\omega) = \varepsilon_\infty - \frac{\omega_p^2}{\omega^2 + i\gamma\omega}, \tag{1.3}$$

where ω_p is the R-VO_2 plasma frequency, characterizing the collective oscillation of free carriers; γ is the damping constant representing carrier scattering; ε_∞ is the high-frequency dielectric constant; and ω is the frequency of the incident light.

In the IR range, where $\omega_{\mathrm{IR}} < \omega_p$, the real part of the dielectric function becomes negative ($\mathrm{Re}[\varepsilon(\omega)] < 0$), leading to a metallic response that prohibits electromagnetic wave propagation inside the material. As a result, R-VO_2 exhibits high reflectivity in the infrared spectral region. Due to finite damping ($\gamma \neq 0$), weak absorption arises from dissipative losses of free electrons. [46]

Conversely, at higher frequencies such as in the visible range ($\omega_{\mathrm{VIS}} > \omega_p$), the dielectric response becomes insulating-like ($\mathrm{Re}[\varepsilon(\omega)] > 0$), since the free carriers cannot respond to the rapidly oscillating electric field. Consequently, reflectance drops sharply. Absorption in this range is dominated by interband transitions; however, due to the lack of empty states near the Fermi level, such absorption remains weak. Thus, R-phase VO_2 maintains relatively high transmittance in the visible region. [46, 47]

The characteristic brownish-red appearance of rutile-phase VO_2 stems directly from its complex electronic band structure, which facilitates multiple interband transition mechanisms across the visible spectrum. Notably, optical transitions from the O $2p$ dominated σ and π to either the π^* or $d_\parallel$ states involve excitation energies of approximately 2.0–2.5 eV, [21, 25] corresponding to absorption in the blue-to-green region of the visible spectrum (500–620 nm). Additionally, $d_\parallel \rightarrow \pi^*$ transitions spanning 1.1–2.5 eV [25] contribute to partial attenuation of yellow and green-edge photons. [8]

Moreover, free carriers derived from the partially filled π^* band produce significant low-frequency optical response as described by the Drude model. In the near-infrared to red-light regime (775–1030 nm, ∼1.2–1.6 eV), these carriers lead to strong reflection and weak absorption due to intraband transitions, effectively suppressing the infrared and red component of the transmitted light. [25, 46]

Taken together, these effects produce a selective filtering of the visible spectrum: red light (below ∼1.77 eV) is suppressed by Drude-type reflection and absorption; blue-to-green light (up to ∼2.5 eV) is partially absorbed due to interband transitions; while yellow-to-green light (approximately 2.0–2.3 eV) transmits most effectively. As a result, the human eye predominantly perceives a mixture of transmitted yellow-green photons and diffuse background reflection from the red–infrared

region, yielding the characteristic dark reddish-brown hue of metallic VO_2. This coloration mechanism resembles that of metallic copper or brass, where the optical appearance arises from non-uniform absorption across the visible range driven by specific band structure features. [8, 21, 25, 46]

In contrast, the M_1 phase of VO_2 exhibits a splitting of the $d_\parallel$ and $d_\parallel^*$ bands by approximately 2.5 eV, resulting in the opening of an energy gap of about 0.6–0.7 eV centered at the Fermi level. [25] This gap eliminates free charge carriers, rendering the system insulating. [21,25] As a consequence, the Drude-like free-carrier response vanishes, leading to the disappearance of infrared reflection. Given that the photon energy in the infrared range is significantly lower than the band gap, infrared light is not absorbed but rather transmitted through the material, yielding a high transmittance in this spectral region.

In the visible range, although the M_1 phase is insulating, interband transitions such as O $2p \rightarrow \pi^*$ and $d_\parallel \rightarrow \pi^*$ remain active. These transitions predominantly absorb photons in the blue-green region (approximately 2.0–2.5 eV). [25] Due to the absence of free electrons, the red-light region (below $\sim$1.7 eV) experiences minimal absorption and thus is largely transmitted. [21, 25] As a result, the human eye perceives a mixture of transmitted yellow-green light and a weak red background, giving rise to a warm brown hue. Compared to the metallic R phase, the M_1 phase appears brighter and more saturated in color, primarily due to reduced free-carrier scattering and enhanced optical transmittance. [8]

The temperature-dependent electronic band structure of VO_2 gives rise to a unique infrared switching effect, which serves as the physical basis for VO_2-based smart windows aimed at dynamic solar control. A comprehensive understanding of this band structure is essential for further exploration and modulation of the MIT in VO_2. Such insights pave the way for targeted strategies including doping, strain engineering, and the manipulation of oxygen vacancies to finely tune the transition behavior and optimize device performance.

1.1.4 Tuning the Metal–Insulator Transition

The MIT in VO_2 can be broadly tuned through three primary strategies: extrinsic element doping, strain engineering, and oxygen vacancy modulation (intrinsic doping). Although these approaches are often treated as distinct in methodology and mechanism, they are inherently interconnected and strongly coupled. For instance, dopants not only introduce additional charge carriers but can also induce local lattice distortions or alter the concentration of oxygen vacancies. Strain, in turn, modifies lattice symmetry and the electronic band structure, thereby influencing the formation energy of oxygen vacancies. Conversely, the creation of oxygen

vacancies can change carrier concentration and trigger lattice distortions, which in turn affect the phase stability. Therefore, a comprehensive understanding and effective control of the MIT in VO_2 require the consideration of the synergistic interplay among these intertwined factors.

Doping is a powerful strategy for tailoring the MIT properties of VO_2 and is commonly classified into *n*-type and *p*-type approaches. *n*-type doping refers to the introduction of dopants that donate extra electrons to the host lattice, thereby increasing the electron carrier concentration and shifting the Fermi level toward the conduction band.

In the case of VO_2, *n*-type dopants such as tungsten (W^{6+}) substitute for vanadium (V^{4+}) and contribute additional electrons to the system. [48, 49] These electrons occupy the π^* conduction band states, weaken the insulating M_1 phase, and enhance the stability of the metallic rutile phase.

As a result, *n*-type doping has proven particularly effective in reducing the T_c of VO_2. For instance, W doping can lower T_c by approximately 27 °C per atomic percent, a trend that has been consistently observed in both experimental and theoretical studies. [48, 49] This capability is especially valuable in optoelectronic applications such as smart windows, where precise tuning of T_c and the optical band gap is often required.

The underlying mechanism involves two key factors. First, when W^{6+} ions substitute for V^{4+} in the VO_2 lattice, each dopant contributes two additional electrons to the system. These excess electrons primarily populate the conduction band, dominated by π^* states, which elevates the Fermi level and enhances the metallic character of the system. In the monoclinic M_1 phase, V–V dimerization opens a band gap of approximately 0.6–0.7 eV, conferring insulating behavior. Because the band gap in the M_1 phase is relatively narrow, it is insufficient to confine these additional carriers originating from W–doping, thus weakening the insulating state and destabilizing the M_1 phase. [50]

Second, W doping induces local lattice distortions, breaking the symmetry of the O–V octahedra and disrupting the tendency toward V–V pairing. In contrast, W ions exhibit a structural preference for the equidistant V–V chains in the rutile R phase, which further stabilizes the metallic phase. This dual effect—electron doping and symmetry breaking—collectively lowers the relative energy of the R phase and shifts the T_c to lower temperatures. [51]

Here, W doping is employed as a representative example to elucidate the underlying physical mechanism by which n-type doping reduces the T_c in VO_2. A comprehensive discussion of other n-type dopants is omitted here for brevity, as the focus is placed on the general mechanism rather than the dopant-specific variations.

Oxygen–vacancy control of the MIT in VO_2 can be viewed as intrinsic n-type doping: without introducing extrinsic elements, adjusting only the stoichiometry to create local oxygen deficiency generates V_O point defects that donate electrons. [52,53] As discussed in Sec. 1.1.2, in metallic VO_2 the π^* and $d_\parallel$ bands overlap and are partially filled, with the Fermi level residing within the overlapping region. In metallic VO_2 containing oxygen vacancies, V–V dimerization is weakened, [54] and the number of unoccupied states in the π^* and $d_\parallel$ bands is reduced, leading to a higher Fermi level, reflecting the band-filling effect of electrons donated by oxygen vacancies. This band-filling effect suppresses the metal–insulator transition and stabilizes the metallic phase similar to W–doping. [55]

p-type doping refers to the introduction of lower-valence-state impurity atoms that create holes as the dominant charge carriers in the host lattice. In VO_2, where the metal–insulator transition arises from a cooperative interplay between Mott localization and Peierls distortion, the influence of p-type doping must be evaluated in the context of both the dopant species and its concentration.

Typically, p-type doping in VO_2 is achieved by substituting V^{4+} with lower-valence ions such as Cr^{3+}, Al^{3+}, or Mg^{2+}. [56] Each substitution of atom effectively removes one or two electrons from the system, thereby introducing a hole and reducing the electronic occupancy of the $d_\parallel$ orbital. In pristine VO_2, the Fermi level lies between the $d_\parallel$ bonding and the π^* conduction bands. Upon hole doping, the Fermi level shifts downward toward the $d_\parallel$ bonding states. [56,57]

Thermodynamically, this shift promotes electron localization, pushing the system toward a correlation-driven Mott-insulating regime. The reduction in itinerant-electron density amplifies the role of on-site Coulomb repulsion (Hubbard U) relative to the electronic bandwidth (W), thereby increasing the U/W ratio and reinforcing electron–electron correlations as described by the Hubbard model. As a result, a correlation-induced Mott barrier emerges, stabilizing the monoclinic M_1 insulating phase and leading to an upward shift of the transition temperature T_c under low-doping conditions.

Moreover, experimental studies—such as those involving Cr doping—have reported the emergence of intermediate phases. Specifically, the appearance of the monoclinic M_2 phase, characterized by alternating V–V dimers and zigzag chains of undimerized vanadium atoms, reveals a more complex structural evolution pathway during the MIT and suggests enhanced phase competition. [58]

In certain cases, p-type dopants (e.g., Al^{3+}) may also induce oxygen vacancies, i.e. comparing n–type dopants, as part of a charge compensation mechanism. These vacancies release additional electrons, introducing an effective n-type contribution that partially offsets the hole doping. [56] Consequently, the influence of p-type

doping on the MIT can exhibit non-monotonic behavior, governed by the interplay between hole-induced effects and defect-mediated electronic compensation.

Stress engineering represents a powerful and widely applied strategy for tuning crystal structure stability, electronic band structure, and phase transition behavior. The application of external stress can induce variations in lattice parameters, atomic displacements, and orbital reconfigurations, thereby driving a range of macroscopic phenomena such as plastic deformation, band gap modulation, and phase boundary shifts. [59]

To quantitatively describe the mechanical response of a crystal under stress, the **Burgers vector** (**b**) is introduced as a fundamental descriptor of the magnitude and direction of lattice distortion associated with dislocations. Dislocations, as line defects, serve as primary carriers of crystal plasticity, and their motion—either by glide or climb—typically follows the path of least energy, which is inherently dictated by the orientation of **b**. [60]

First, we introduce the concept of the Burgers vector in an ideal cubic crystal. As illustrated in Figure **1.14a**, a rectangle is drawn in a perfect cubic lattice, with its length and width being integer multiples of the lattice constant a (the unit cell edge length), oriented along the path A $\rightarrow$ B $\rightarrow$ C $\rightarrow$ D.

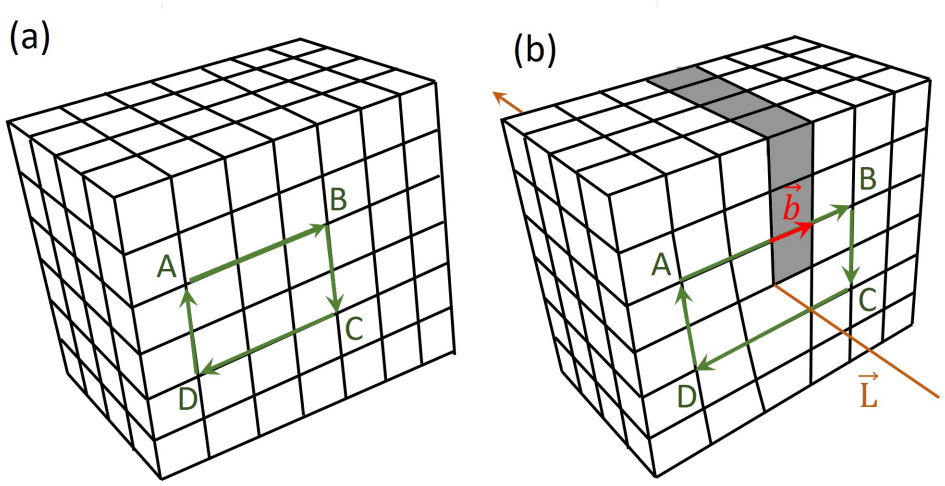

Figure 1.14: (a) Schematic diagram of a perfect cubic structure. (b) Cubic structure-edge dislocation

A pure edge dislocation, shown in Figure **1.14b**, can be visualized as the insertion of an extra half-plane (gray blocks) into the crystal, breaking its translational

symmetry. To determine the Burgers vector, a circuit is traced clockwise around the dislocation line, with each step connecting fully coordinated lattice sites. This circuit is then transferred to an equivalent perfect lattice. In the absence of a dislocation, the loop fails to close; the vector connecting the terminal point to the starting point defines the Burgers vector $\mathbf{b}$, while $\mathbf{L}$ denotes the dislocation line vector. For an edge dislocation, $\mathbf{b} \perp \mathbf{L}$. [60]

In studies of strain control of the VO_2 MIT, stresses in thin films predominantly originate from film–substrate interfacial effects. [61] Such VO_2 layers are typically highly textured or epitaxial, and the resulting strain is graded across the thickness. Effective design must therefore consider both the substrate crystal structure—which sets the magnitude and orientation of the Burgers vectors $\mathbf{b}$ associated with misfit dislocations—and the film thickness.

Stress control in VO_2 thin films falls into two regimes: (i) biaxial and (ii) uniaxial. In the biaxial case—typical when the in-plane rutile VO_2 axes a and b are co-tuned (e.g., $VO_2/TiO_2(001)$, Fan *et al.* [62])—in-plane tension with $\mathbf{b} \parallel a$ or b compresses the out-of-plane c axis. A larger $|\mathbf{b}|$ (stronger interfacial strain) correlates with a lower T_c. As thickness increases, strain relaxation reduces $|\mathbf{b}|$; accordingly, T_c increases with thickness.

From a band perspective, thinner VO_2 films exhibit an upward shift of the $d_\parallel$ level, reduced $d_\parallel$ occupancy, and increased π^* occupancy. In the metallic state, enhanced overlap between the antibonding π^* band and the $d_\parallel$ and $d_\parallel^*$ bands promotes charge transfer from $d_\parallel$, $d_\parallel^*$ to π^*, weakens electron–electron interactions, and stabilizes metallicity. Conversely, in the insulating state the reduced $d_\parallel$–π^* separation lowers the nucleation barrier and advances the MIT, consistent with the reduced T_c observed in ultrathin films. [62]

In Chapter 3, we investigate uniaxial strain control in a series of VO_2 epitaxial films grown on $TiO_2(110)$ substrate. Rutile TiO_2 possesses a larger lattice constant along the c axis ($c_{TiO_2} \approx 2.959$ Å) than rutile VO_2 ($c_{VO_2} \approx 2.851$ Å), it imposes tensile strain along the rutile c axis of the VO_2 film (i.e., $\mathbf{b} \parallel c$). A larger Burgers vector magnitude $|\mathbf{b}|$ correlates with a higher T_c. As the film thickens, strain relaxation reduces $|\mathbf{b}|$, and T_c approaches the intrinsic value of VO_2. Beyond a critical thickness, oxygen vacancies can emerge and depress T_c below the intrinsic value.

However, in Chapter 4, we do not employ this approach to tune VO_2 film properties. That section targets the translation of VO_2-based smart windows from laboratory demonstrations to large-area, large-format manufacturing, for which the films are deposited by magnetron sputtering. This route is incompatible with epitaxial

growth, and the TiO_2 buffer layers (prepared by magnetron or plasma sputtering) are polycrystalline with randomly oriented surface facets, precluding effective, deterministic strain control.

Building on the above discussions, element doping, strain engineering, and oxygen-vacancy control in VO_2 are not independent knobs but tightly coupled. Doping modifies carrier density, introduces local lattice distortions, and can shift the equilibrium concentration of oxygen vacancies; strain (epitaxial or applied) reshapes lattice parameters and symmetry, thereby tuning the electronic structure as well as the formation energy and spatial distribution of V_O; conversely, creating oxygen vacancies acts as intrinsic n-type doping that raises the carrier density and induces local distortions, feeding back on phase stability. A comprehensive understanding and effective control of the MIT thus require treating these factors as synergistic and co-designed rather than separable.

1.2 Thermochromic VO_2 Coatings for Smart Windows

VO_2, as a thermochromic material with outstanding performance, has attracted considerable attention in the field of smart windows. [63] VO_2 is distinguished by its abrupt change in optical transparency at the MIT, enabling precise and stable modulation without the need for mechanical actuation or complex electrothermal systems. It exhibits a reversible temperature-dependent dielectric constant, with a pronounced contrast between the metallic and insulating states. The rutile phase of VO_2 undergoes its reversible transition to the monoclinic phase at a relatively moderate critical temperature (T_c, 68 °C), accompanied by significant structural and optical changes. These unique characteristics have rendered VO_2 an ideal thermochromic candidate for smart window applications for decades. [37, 63]

Meanwhile, the ever-increasing global demand for energy consumption and the associated CO_2 emissions have intensified the issue of global warming, underscoring the urgent need for energy conservation and emission reduction. Studies indicate that residential buildings account for approximately 30–40% of global primary energy consumption, making the improvement of building energy efficiency a pressing priority. [64] Among various building components, windows have received particular attention due to their relatively low energy efficiency and high maintenance requirements, [65] which has driven smart windows to become a prominent research topic across optics, materials science, and architectural science. Windows play a critical role in providing thermal, visual, and acoustic comfort, while also being associated with daylighting, ventilation, UV protection, skin cancer prevention,

and psychological well-being. [66–69] The interaction between solar radiation and windows involves transmission, reflection, or absorption, which depends on their optical properties in the ultraviolet (UV), visible, and near-infrared (NIR) spectral regions. High transmittance in the visible range is essential to meet illumination requirements, whereas the ideal smart window should enable dynamic switching between high and low transmittance in the UV and NIR regions. Such functionality can reduce cooling loads during hot seasons and enhance solar heat gain during cold seasons. The thermochromic nature of VO_2 provides an efficient mechanism for regulating solar radiation in the invisible spectrum according to environmental temperature, offering a promising solution for the next generation of energy-efficient buildings.

The application of VO_2 in smart windows essentially represents a functional extension of its MIT characteristics. Building upon the understanding of the fundamental mechanisms governing MIT modulation, as outlined in Section 1.1.3, this section focuses on strategies for tailoring MIT properties that are most relevant to smart window performance, specifically the reduction of the transition temperature and the widening of the optical band gap.

1.2.1 Strategies for Lowering T_c

Lowering the T_c of VO_2 toward ambient conditions is a primary research objective. Chemical doping is the most widely used and effective approach to tune T_c. Substitutional dopants stabilize the rutile phase and thereby reduce the T_c via two main mechanisms: (i) supplying extra charge carriers and (ii) introducing lattice strain in the thin VO_2 based films that favors the rutile structure.

Substitutional doping with high-valence cations such as W^{6+}, Mo^{6+}, Nb^{5+}, and Ru^{4+} on V^{4+} sites donates electrons to the lattice, stabilizing the rutile phase and lowering T_c. [48, 49, 70–73] Among reported metal dopants, W shows the highest efficiency: T_c decreases approximately linearly with W content at a rate of ≈ 20 °C/at.%. [48,49] However, W doping also markedly narrows the optical band gap of VO_2, leading to a substantial reduction in visible transmittance. [74] For example, in a VO_2 film containing 2 at.% W with a thickness of 80 nm, T_c is reduced to $\sim$ 17 °C, while the room-temperature visible transmittance drops to only 45.1%. [75] In addition, increasing W content degrades the infrared switching performance, underscoring the need to balance T_c reduction against optical and switching properties through careful engineering optimization. [74]

Compared with W, Ru doping is less efficient in lowering T_c (about 6.5 °C/at.%), but it better preserves the optical band gap and visible transmittance of VO_2. For instance, when 4 at.% Ru is incorporated into the VO_2 lattice, T_c decreases to about

42 °C; for a 90 nm-thick film, the room-temperature visible transmittance remains comparable to undoped VO_2, and the infrared modulation amplitude can still be maintained at roughly 17%. [73] From a cost perspective, W is far more economical than Ru (e.g., metallic W ∼70–71 USD/kg versus metallic Ru ∼26,400 EUR/kg), making W doping a more practical option for low-cost fabrication of VO_2 films with reduced T_c. [76, 77].

Beyond high-valence substitutional cations, interstitial donors such as hydrogen (H) can also significantly depress T_c. [78] The mechanism involves the electrons donated by H filling the $d_{\parallel}$ band associated with V–V dimerization, thereby enhancing metallicity and lowering T_c. Theoretically, the efficiency of H doping in reducing T_c can reach ∼ 38 °C/at.%; [79] however, current synthesis and control techniques make stable and quantitatively controllable H incorporation in VO_2 challenging.

It should be emphasized that electron-donor-based doping strategies are generally accompanied by enhanced free-carrier absorption and the formation of mid-gap states, which lead to a reduction in visible transmittance and a weakening of the infrared modulation capability (ΔT_{sol}). To address these limitations, multi-element doping (co-doping) has been extensively investigated. In this approach, two different elements are simultaneously incorporated into VO_2: one element is used to lower T_c, while the other serves to widen the band gap, thereby achieving a balance between transition temperature reduction and optical performance.

For example, co-doping with W and low-valence cations (e.g., Mg^{2+}, Al^{3+}, or Sr^{2+}) not only decreases T_c but also improves transparency to some extent. [80–82] Dietrich [83] demonstrated that introducing Sr together with W in VO_2 lowers the transition temperature while partially compensating for optical absorption, resulting in a higher luminous transmittance (T_{lum}) than that of singly W-doped VO_2. Another study reported that W+Zr co-doped VO_2 films achieved a T_c of ∼47 °C with $T_{\mathrm{lum}} \approx 48.6\%$ and $\Delta T_{\mathrm{sol}} \approx 4.9\%$, [84] outperforming singly W-doped films in terms of optical metrics. Moreover, mixed-valence co-doping (e.g., Fe^{3+} + Mg^{2+}) has also been reported to reduce T_c to ∼38 °C while simultaneously enhancing both visible transmittance and solar modulation. [85] It should be noted that such improvements in optical performance essentially involve modifications of the electronic band structure of VO_2, and therefore fall under the broader concept of band-gap engineering. In this section, co-doping is discussed as a complement to temperature regulation, while detailed optical and band-gap modulation mechanisms will be elaborated in the following section.

In addition to extrinsic doping, stoichiometry control and strain engineering are also effective in modulating the phase transition. VO_2 is highly sensitive to oxygen content: slight oxygen deficiency (VO_{2-x}) leads to the formation of V^{3+} defect centers, which act as self-doping sites and reduce T_c. For example, by precisely controlling the oxygen partial pressure during reactive sputtering—without introducing foreign

dopants—the T_c of VO_2 films could be tuned within the range of 46–72 °C. [86] The underlying mechanism is analogous to n-type doping, since oxygen vacancies donate electrons and destabilize the insulating phase. [52, 53]

Strain engineering provides another effective approach: by applying external stress or selecting substrates with different lattice mismatches, the lattice parameters of VO_2 can be modified, thereby tuning T_c. Epitaxial VO_2 thin films under tensile strain typically exhibit a lower T_c, whereas compressive strain tends to increase T_c. This behavior is consistent with the mechanism that lattice expansion weakens V–V dimerization and promotes stabilization of the metallic phase. For example, VO_2 grown on sapphire or TiO_2 substrates shows a modulated transition temperature due to differences in thermal expansion coefficients and lattice matching. Furthermore, reducing the film thickness down to the nanoscale can also induce effective strain or quantum size effects, which alter T_c. When the thickness of VO_2 films was reduced from 150 nm to only a few nanometers, T_c decreased significantly, an effect attributed to strain relaxation and surface effects. [87]

In summary, elemental doping, defect engineering, and strain engineering constitute the primary strategies currently employed to reduce the transition temperature of VO_2 for smart window applications. However, balancing the reduction of T_c with the preservation of desirable optical performance remains a critical challenge to be addressed.

1.2.2 Band-Gap Engineering and Enhancing Visible Transparency

As discussed above, certain T_c-lowering doping schemes (e.g., W–Sr and W–Zr co-doping) also modify the electronic band structure of VO_2, thereby affecting its visible transmittance. This indicates that band-structure modulation and band-gap engineering are central to improving the optical performance of VO_2. In its insulating monoclinic phase, VO_2 possesses an intrinsic band gap of $\sim$ 0.7 eV, but also exhibits higher-energy electronic transitions around 2.5 eV that extend into the visible spectrum, producing pronounced film coloration. [**?**] In the metallic rutile phase, additional Drude absorption from free carriers further reduces red light transmittance. Therefore, the objective of band-gap engineering is to broaden the effective band gap or suppress absorption in the 400–700 nm range, while retaining strong near-infrared (NIR) modulation capability.

Band-gap widening in VO_2 is most naturally understood as tuning a cooperative Peierls–Mott insulator [30,31]. In the insulating M_1 phase, V–V dimerization along the rutile c_R axis splits the $d_\parallel$ manifold into bonding and antibonding subbands (a

Peierls gap), while electron correlations (finite Hubbard U) narrow the t_{2g} bandwidth [9]. The resulting hierarchy places a valence-band maximum (VBM), dominated by O $2p$–V $3d$ bonding states, below a conduction-band minimum (CBM) composed mainly of V $d_{\parallel}^{*}$ and π^{*} antibonding states. Perturbations that increase the dimerization amplitude or decrease the effective bandwidth W relative to U push these edges apart: the bonding $d_{\parallel}$ states are stabilized (VBM downshift) and the antibonding states are destabilized (CBM upshift). Low-valence cation substitution (e.g., Mg^{2+} on V^{4+} sites) acts effectively as hole doping: charge compensation drives partial $V^{4+} \rightarrow V^{5+}$, reduces screening, and increases U/W; concomitant size/charge mismatch distorts VO_6 octahedra, modifying specific V–O bond lengths, crystal-field splittings, and p–d covalency. In band terms, strengthened V–V pairing enlarges the $d_{\parallel}$ bonding–antibonding separation (raising the CBM), while reduced covalency lowers the VBM—both trends widen the gap [88]. Anion substitution (e.g., F^{-} for O^{2-}) alters the ligand field and V–O hybridization: fluorine's deeper $2p$ level increases the p–d energy separation, weakens p–d mixing, and drives the bonding manifold to lower energy (VBM downshift). Although O→F nominally donates electrons, these carriers can localize (small-polaron or mixed-valence V^{3+}/V^{4+} sites), avoiding CB filling; simultaneously, reduced covalency and local relaxation enlarge the Peierls splitting, pushing the CBM up [89]. Viewed through a molecular-orbital lens, successful gap-widening routes share two ingredients: (i) a larger bonding–antibonding separation within the $d_{\parallel}$ channel (stronger V–V bond order) and/or (ii) deeper ligand-derived bonding states via tuned V–O (or V–F) hybridization that lower the VBM while correlations keep the t_{2g} bands narrow. The optical consequence is a blue-shifted absorption edge, suppressed visible absorption, and hence higher luminous transmittance, achievable without compromising near-infrared thermochromic modulation when dopant level and strain state are carefully controlled.

Besides doping, nanostructuring and composite strategies have been widely employed to enhance the visible transmittance of VO_2. Reducing the VO_2 grain size or dispersing VO_2 within a transparent matrix can effectively suppress light scattering and incoherent absorption. For example, VO_2–SiO_2 composite films exhibit significantly improved T_{lum} and ΔT_{sol}, because SiO_2 not only acts as a transparent spacer that lowers the optical density but also reduces reflection via refractive-index matching. [90] Similarly, antireflection coatings and multilayer interference designs (e.g., $TiO_2/VO_2/TiO_2$ sandwich stacks) can improve optical performance, although the enhancement is usually moderate. [91]

Furthermore, core–shell nanostructures (e.g., ZnO-coated VO_2 nanoparticles) have been demonstrated to increase both visible transparency and solar modulation. The ZnO shell not only prevents aggregation of VO_2 particles but also provides antireflection and antioxidation functions, yielding $T_{\mathrm{lum}} \approx 51\%$ and $\Delta T_{\mathrm{sol}} \approx 19\%$, both markedly superior to bare VO_2 nanoparticles. [92]

Overall, band-gap and electronic-structure engineering of VO_2—through doping, composite formation, and photonic design—is a key route to improve optical performance. Recent studies have achieved performance levels of $T_{\mathrm{lum}} > 60\%$ and $\Delta T_{\mathrm{sol}} > 10\%$. [93] Table 1.2 summarizes representative performance metrics of VO_2-based smart-window systems reported in recent years. [8]

Table 1.3: Summary of dopant effects on VO_2 transition temperature and optical properties

Group	Dopant	Doping Level (%)	T_{lum} (%)	ΔT_{sol} (%)	dT_c/dx (°C/at.%)	Method
IA	H	3	–	–	−38	simul.
	Li	3	–	–	−43	simul.
	Na	3	–	–	−49	simul.
	K	3	–	–	−94	simul.
IIA	Be	3	–	–	−58	simul.
	Mg	5	82.1	4.8	−3	expt.
	Ca	1.3	–	7.6	–	expt.
	Sr	9.6	54.3	5.0	–	expt.
	Sr	6.8	50.3	6.5	–	expt.
	Ba	8.3	–	7.5	–	expt.
IIIA	B	–	–	–	−83	simul.
VIIA	F	2.93	48.7	10.7	−11.3	expt.
TM	W	2	45.1	6.9	−20	expt.
	Mo	2	–	–	−11	expt.
	Nb	2–3	–	–	−7.8	expt.
	Zr	9.8	60.4	14.1	−0.4	expt.
	Ti	1.1	53.0	17.2	0	expt.
	Ru	4	23.5	–	−6.5	expt.
RE	Eu	4	54.0	6.7	−6.5	expt.
	Tb	4	65.9	4.6	−1.5	expt.
	La	4	50.1	10.3	−1.1	expt.
Co-doping	Mg+W	4% Mg + 2% W	81.3	4.3	−5.5	expt.
	F+W	2.1% F + 1.8% W	–	–	−17.4	expt.
	Zr+W	8.5% Zr + 0.6% W	56.4	12.3	−1.3	expt.
	Mo+W	1.02% Mo + 0.36% W	–	–	−23	expt.
	Hf+W	11% Hf + 3% W	41.1	–	−7.6	expt.

1.2.3 Challenges and Our Approaches

Despite decades of research into VO_2 for smart window applications, several fundamental challenges continue to hinder its commercialization. The two most intrinsic limitations are its relatively high metal–insulator transition temperature, approximately 68 °C, which is significantly higher than ambient temperature, and its narrow optical band gap of about 2.6 eV. [21] These properties make binary VO_2 suboptimal for energy-saving applications under typical ambient conditions.

To address these issues, doping or alloying has become a widely employed strategy for tailoring the MIT temperature and optical band gap. However, conventional

single-element doping typically affects only one parameter and often introduces trade-offs. For example, W doping significantly reduces the MIT temperature but concurrently narrows the band gap, compromising visible light transparency. [74] Conversely, Al doping widens the band gap but raises the MIT temperature. [81] Therefore, recent research has focused on co-doping approaches—such as Hf–W or Sr–W co-doping—to achieve simultaneous modulation of both properties and offset the antagonistic effects. [48, 49, 74, 81, 83]

Yet, whether modifying the transition temperature or the band gap, doping often leads to diminished optical modulation performance. This makes it necessary to precisely optimize the doping concentration to strike a balance among interdependent properties. To compensate for optical degradation, VO_2 is frequently embedded in multilayer thin-film systems. [94] By applying Fresnel antireflection principles, these structures enhance transmittance in specific spectral regions through careful control of layer thickness and interfacial roughness.

Beyond intrinsic material limitations, two major practical constraints further hinder large-scale adoption. First, the high synthesis temperature of VO_2—typically exceeding 400 °C—leads to substantial energy consumption and elevated production costs. While buffer layers have been developed to reduce the required growth temperature, their use must preserve the functional optical switching behavior. Notably, TiO_2 has proven effective as a buffer layer, enabling VO_2 deposition at temperatures as low as 300 °C while retaining acceptable modulation performance. [95] However, growing rutile TiO_2 as buffer layer on glass requires temperature exceeding 550 °C.

Second, the metastable V^{4+} oxidation state in VO_2 is highly susceptible to degradation under ambient conditions, as it tends to oxidize into the pentavalent V^{5+} state. This oxidation deteriorates the material's switching properties and long-term durability. [96] Therefore, an effective passivation layer is essential to maintain stability. Interestingly, antireflection layers in multilayer configurations can also serve this protective role, offering dual benefits in optical enhancement and environmental resistance.

In view of the aforementioned interrelated challenges, this dissertation presents two complementary strategies. The first explores the potential of tuning the MIT characteristics in crystalline VO_2 thin films through strain engineering. Without extrinsic doping, the transition temperature is modulated by controlling oxygen vacancy concentrations and epitaxial stress, offering a promising pathway toward applications in VO_2-based smart windows and related devices. Internal stress within single-crystalline and highly oriented VO_2 thin films can induce lattice strain, thereby modulating the film's microstructure. Under uniaxial strain, the interplanar spacing of crystal planes aligned with the stress direction increases under tensile strain

and decreases under compressive strain. In contrast, planes perpendicular to the strain direction exhibit an opposite trend in their interplanar spacing.

For biaxial strain conditions, the scenarios can be categorized as follows: (i) simultaneous biaxial compression, where the *ab*, *ac*, or *bc* planes are all under compressive strain and the corresponding out-of-plane direction (*c*, *b*, or *a*) experiences tensile strain; (ii) simultaneous biaxial tension, where the in-plane directions are under tensile strain while the out-of-plane direction is compressed; and (iii) biaxial strain of opposing directions, in which the in-plane lattice experiences strain in different directions, leading to either tensile or compressive out-of-plane strain depending on the specific stress configuration [97].

In this study, we focus on the in-plane strain of VO_2 thin films along the rutile *c*-axis and examine its influence on the macroscopic physical properties. This strain originates from the lattice mismatch between the film and the substrate: the rutile TiO_2 substrate possesses a larger *c*-axis lattice parameter than the epitaxial VO_2(R) film. As the film thickness increases, edge dislocations are introduced to relieve the mismatch, with the Burgers vector **b** oriented parallel to the *c*-axis of both R-TiO_2 and R-VO_2.

The second strategy addresses the simultaneous challenges of thermal budget, phase stability, and optical modulation performance. To this end, we propose a multilayer thin-film system. The trilayer thin-film architecture comprises a Cu:TiO_2 buffer layer, a VO_2 active layer, and a TiO_2 antireflection coating. The buffer layer plays a critical role in lowering the crystallization temperature of VO_2 while enhancing its structural quality. On amorphous substrates such as soda-lime glass or quartz, high substrate temperatures—typically exceeding 400 °C—are required to stabilize the monoclinic phase. The dashed region in Figure **1.12** delineates the VO_2 growth window established in our lab via magnetron sputtering.

Quartz glass, being an amorphous substrate with a disordered atomic structure, lacks a crystalline template for epitaxial alignment. This significantly hinders the nucleation of VO_2, which tends to initially form either the metastable VO_2(B) phase or an amorphous structure due to their lower nucleation barriers. Furthermore, the large mismatch in thermal expansion coefficients between $VO_2(M_1)$ (approximately $1.71 \times 10^{-5}\,K^{-1}$) and quartz (approximately $5 \times 10^{-7}\,K^{-1}$) induces substantial tensile stress during deposition and annealing. Combined with the intrinsic lattice incompatibility arising from the non-crystalline nature of quartz, these stresses impede the low-temperature crystallization of the monoclinic $VO_2(M_1)$ phase. As a result, achieving high-quality $VO_2(M_1)$ films on quartz substrates typically requires elevated temperatures and prolonged annealing to overcome both structural and thermomechanical barriers. In contrast, the TiO_2 buffer layer—typically crystallizing in the rutile phase—exhibits lattice parameters closely matched to those of $VO_2(M_1)$, with a lattice mismatch of only ∼0.86%. This favorable lattice alignment

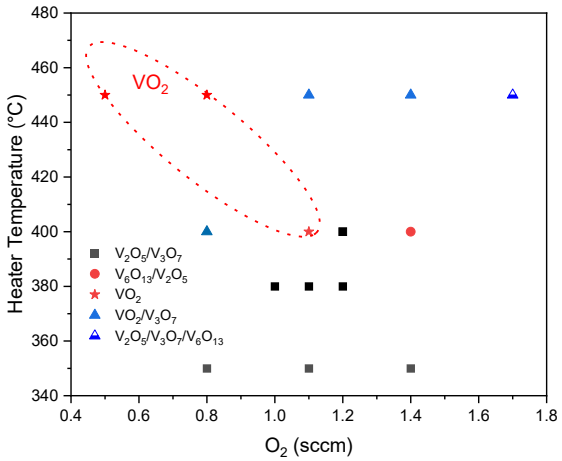

Figure 1.15: Growth window diagram for VO_2.

provides an effective heteroepitaxial template that promotes preferential orientation during VO_2 nucleation and growth. Additionally, acting as an intermediate transition layer between the VO_2 film and the glass substrate, the TiO_2 buffer can partially relieve interfacial stress caused by thermal expansion mismatch and structural incompatibility. These combined effects—lattice templating and strain mediation—notably enhance the crystalline quality and macroscopic uniformity of the VO_2 film. Consequently, the incorporation of a TiO_2 buffer not only reduces the crystallization temperature of VO_2 but also facilitates high-quality growth under lower thermal budgets.

However, the formation of rutile-phase TiO_2 typically requires annealing temperatures exceeding 600 °C, which is incompatible with the lower-temperature requirements for VO_2 film growth. To address this challenge, we employed Cu doping in TiO_2 to effectively reduce the crystallization temperature required for rutile phase formation. The underlying mechanism is as follows: The ionic radii of Cu^{2+} and Cu^{+} are 0.073 nm and 0.077 nm, respectively, slightly larger than the ionic radius of Ti^{4+} (0.0605 nm). Cu^{2+} and Cu^{+} ions likely substitute Ti^{4+} ions in the TiO_2 lattice without inducing the formation of a secondary phase. The substitution of Cu^{2+} and Cu^{+} ions induces lattice distortion and generates oxygen vacancies, weakening Ti–O bonds and facilitating the nucleation and growth of the rutile phase [98].

The tri-layer antireflection (AR) structure employs two interference layers positioned above and below a functional layer (e.g., VO_2). Spectroscopic ellipsometry was performed at 15 °C and 100 °C to obtain the dispersion of VO_2, TiO_2, and $Cu_xTi_{1-x}O_2$ over 200–3000 nm. The experimental $n(\lambda)$ and $k(\lambda)$ were imported as table-dispersion materials (one dataset per temperature). If needed, smooth analytic fits (e.g., Cauchy/Sellmeier) were used to reduce high-frequency noise while

preserving the measured trends.

For a multilayer stack at wavelength λ, each layer j is described by its complex refractive index

$$\tilde{n}_j(\lambda) = n_j(\lambda) - i\,k_j(\lambda),$$

its physical thickness d_j, and the corresponding complex phase retardation

$$\delta_j(\lambda) = \frac{2\pi}{\lambda}\,\tilde{n}_j(\lambda)\,d_j.$$

Under normal incidence, the 2×2 characteristic matrix of layer j can be written as

$$M_j(\lambda) = \begin{bmatrix} \cos\delta_j & \dfrac{i}{\tilde{n}_j}\sin\delta_j \\ i\,\tilde{n}_j\,\sin\delta_j & \cos\delta_j \end{bmatrix}.$$

The total transfer matrix of the stack is $M(\lambda) = \prod_j M_j(\lambda)$, ordered from the incident medium to the substrate. Denoting the (complex) refractive indices of the incident medium and the substrate by $\tilde{n}_0$ and $\tilde{n}_s$, the transmission amplitude is

$$t(\lambda) = \frac{2\,\tilde{n}_0}{\tilde{n}_0 M_{11} + \tilde{n}_0\tilde{n}_s M_{12} + M_{21} + \tilde{n}_s M_{22}}.$$

The spectral transmittance is then

$$T(\lambda) = \frac{\mathrm{Re}\big(\tilde{n}_s\big)}{\mathrm{Re}\big(\tilde{n}_0\big)}\,\big|t(\lambda)\big|^2,$$

which rigorously accounts for multiple-beam interference and absorption in all layers (film stack coherent; substrate treated as incoherent if thick).

Spectral weighting and figures of merit. From $T(\lambda)$, the luminous and solar transmittances are computed as

$$T_{\mathrm{lum}} = \frac{\displaystyle\int_{380}^{780} \varphi(\lambda)\,E_\lambda\,T(\lambda)\,\mathrm{d}\lambda}{\displaystyle\int_{380}^{780} \varphi(\lambda)\,E_\lambda\,\mathrm{d}\lambda}, \qquad T_{\mathrm{sol}} = \frac{\displaystyle\int_{300}^{2500} E_\lambda\,T(\lambda)\,\mathrm{d}\lambda}{\displaystyle\int_{300}^{2500} E_\lambda\,\mathrm{d}\lambda},$$

where $\varphi(\lambda)$ is the CIE photopic luminous-efficiency function and E_λ is the AM1.5 solar spectral irradiance. The temperature-induced modulation of solar transmittance is

$$\Delta T_{\mathrm{sol}} = T_{\mathrm{sol}}(15^\circ\mathrm{C}) - T_{\mathrm{sol}}(100^\circ\mathrm{C}).$$

Thickness scan. The VO_2 active layer thickness was fixed at 40 nm. The buffer-layer thickness and the anti-reflection (AR) overcoat thickness were scanned independently from 0 to 300 nm in 1 nm increments. For each $(d_{\mathrm{buffer}}, d_{\mathrm{AR}})$ pair and

for each temperature dataset (15 °C and 100 °C), $T(\lambda)$ was computed, followed by the evaluation of T_{lum} and T_{sol}. The results were then assembled into 2D performance maps with buffer-layer thickness on the horizontal axis, AR thickness on the vertical axis, and color scales representing either ΔT_{sol} or T_{lum}.

2 State of the Art

2.1 Thin Film Preparation and Characterization

This section provides detailed descriptions of the thin-film deposition methods and characterization techniques employed in the preparation of VO_2 thin films. Three physical vapor deposition (PVD) methods were utilized: pulsed laser deposition (PLD), radio-frequency (RF) magnetron sputtering, and ion beam sputtering (IBS). Each method was selected based on its unique advantages in controlling film quality, deposition parameters, and reproducibility.

Pulsed laser deposition (PLD) was performed using a KrF excimer laser (Lambda Physik COMPEX PRO 205 F, wavelength 248 nm) with a pulse energy of 600 mJ and an adjustable repetition rate. The target material could be either metallic vanadium or a ceramic target. Localized laser irradiation of the target surface generates a high-energy plasma plume composed of atoms, ions, and molecular fragments. This plume expands rapidly normal to the target surface and reacts with a controlled low-pressure reactive gas in high vacuum—for example, in the preparation of VO_2, 99.999% high-purity oxygen was used—before depositing onto the heated substrate. During deposition, material accumulation and thermal evaporation proceed simultaneously, establishing a dynamic equilibrium.

For different material systems, tunable deposition parameters include the target–substrate distance, pulse repetition rate, substrate temperature, reactive gas type and pressure (equivalent to gas flow rate), and the relative rotation speed between the target and substrate. In practice, deposition temperature and reactive gas composition/pressure are typically adjusted to precisely control the film stoichiometry, crystallinity, and defect concentration.

PLD is well suited for the growth of high-quality epitaxial films. The deposition rate scales positively with pulse repetition rate, while its dependence on substrate temperature is nonmonotonic. Overall, PLD offers a relatively low deposition rate, making it ideal for producing small-scale, small-area films from a few nanometers to several hundred nanometers thick. Its precision and versatility render it a valuable tool for proof-of-concept studies in the laboratory—a key reason why this method was chosen for the stress-engineered MIT investigation presented in Chapter 3.

Compared with PLD, **radio-frequency (RF) magnetron sputtering** enables the fabrication of polycrystalline or amorphous films over large areas at higher deposition rates. In Chapter 4, this method was adopted for film preparation. In RF magnetron sputtering, the RF power supply delivers high-frequency alternating voltage to the target through an impedance matching network, driving both electrons and ions in the plasma. Because electrons have a much higher mobility than ions, a negative self-bias forms on the target surface, thereby accelerating the bombardment of positive ions. The rapid polarity reversal inherent to RF excitation allows charges on the target surface to be neutralized within half a cycle, preventing the charge accumulation that would otherwise interrupt discharge when sputtering insulating targets, as often occurs in direct-current (DC) sputtering. This enables stable deposition of insulating materials such as VO_2 and TiO_2.

A magnetic field placed behind the target is oriented perpendicular to the electric field, forcing electrons into cycloidal motion near the target surface via $\mathbf{E}\times\mathbf{B}$ drift, which significantly increases their collision probability with gas molecules and enhances ionization efficiency. During deposition, parameters such as substrate temperature, sputtering gas flow rate, and reactive gas flow rate can be adjusted to achieve oxide, nitride, and other compound films with the desired stoichiometry. The RF power primarily controls the ion energy and thus the deposition rate.

RF magnetron sputtering is suited to both research-scale film growth and large-scale industrial coating, serving as a crucial bridge between laboratory studies and commercial implementation. This is the primary reason we employed this technique in Chapter 4, where our objective was to propose an industrially viable pathway to advance the commercialization of smart-window technologies.

Ion beam sputtering (IBS) was employed as the third deposition technique in this work, with the objective of fabricating high-quality rutile- and anatase-phase TiO_2 thin films. IBS is a high-precision physical vapor deposition (PVD) method in which high-purity argon (or a mixture of reactive gases) is introduced into the ion source and ionized into a plasma. The ions are then accelerated through a grid system to form a well-collimated Ar^+ ion beam. High-energy ions bombard the target surface, transferring momentum to target atoms and ejecting them into the vacuum chamber. Because the ion energy and incidence angle can be independently controlled, the deposition rate and film properties can be precisely optimized. The ejected atoms travel through the vacuum and condense on the substrate, where substrate heating and a controlled reactive atmosphere can be applied to promote crystallization, tune composition, or enable compound film growth. In **IBS**, the ion energy, incidence angle, and beam current density can be adjusted independently of the chamber pressure. However, the deposition rate is generally lower than that of RF magnetron sputtering, making IBS less suitable for large-scale, high-throughput production.

Film structure and crystallinity were characterized using **X-ray diffraction (XRD)** and **Raman spectroscopy**.

XRD analyses rely on Bragg's law,

$$n\lambda = 2d\sin\theta, \tag{2.1}$$

where n is an integer, λ is the X-ray wavelength, d is the interplanar spacing, and θ is the incidence angle. The resulting diffraction pattern allows phase identification and evaluation of crystal quality by comparing peak positions and intensities against standard databases.

In Chapter 3, **XRD rocking curve scans** and **reciprocal space mapping (RSM)** were employed to meet distinct requirements in crystallographic analysis. A **rocking curve** is a standard method for assessing the out-of-plane mosaicity of thin films. The measurement is performed at a fixed diffraction angle 2θ while the sample tilt angle ω—rotation about the normal to the diffraction plane—is varied slightly, and the diffracted intensity is recorded as a function of ω. The full width at half maximum (FWHM) of the diffraction peak serves as a key metric of crystalline quality: smaller FWHM values indicate higher orientation uniformity and lower defect densities. In addition, the peak profile encodes microstructural information such as mosaic block distribution and strain gradients.

For a mosaic structure comprising numerous small crystallites with slight orientation variations, the tilt distribution can often be approximated by a Gaussian function,

$$P(\Delta\omega) \propto \exp\left(-\frac{\Delta\omega^2}{2\sigma^2}\right), \tag{2.2}$$

where $\Delta\omega$ is the deviation from the ideal orientation and σ is the standard deviation of the orientation spread (in degrees). The corresponding diffraction intensity profile is

$$I(\omega) = I_0 \exp\left(-\frac{(\omega-\omega_0)^2}{2\sigma^2}\right), \tag{2.3}$$

where $I(\omega)$ is the diffracted intensity at tilt angle ω, I_0 is the peak maximum, and ω_0 is the peak center. The FWHM is given by

$$\mathrm{FWHM} = 2\sqrt{2\ln 2}\,\sigma, \tag{2.4}$$

which scales directly with the orientation spread. Gaussian peaks are typically symmetric with rapidly decaying tails.

If a continuous variation in lattice spacing exists along the film normal—e.g., strain relaxation from the interface to the surface—the Bragg condition is satisfied over

a broader ω range, producing a Lorentzian profile,

$$I(\omega) = \frac{I_0}{1 + \left(\frac{\omega - \omega_0}{\Gamma}\right)^2}, \tag{2.5}$$

where Γ is the Lorentzian half-width (in degrees), governed by strain gradients, dislocation density, and related defect structures. Lorentzian peaks feature sharp centers with long, slowly decaying tails, reflecting contributions from multiple strain states.

In practice, both mosaic spread and strain gradients often coexist, yielding a Voigt profile—a convolution of Gaussian and Lorentzian components:

$$I(\omega) = \int_{-\infty}^{+\infty} \frac{I_0}{1 + \left(\frac{\omega' - \omega_0}{\Gamma}\right)^2} \cdot \exp\left(-\frac{(\omega - \omega')^2}{2\sigma^2}\right) d\omega', \tag{2.6}$$

where ω' is the integration variable. Here, Γ and σ quantify the Lorentzian and Gaussian broadening, respectively. Fitting the measured curve to a Voigt function enables separation of the Gaussian contribution (mosaicity) from the Lorentzian component (strain gradient), allowing quantitative assessment of defect origins and their relative influence on crystal quality.

In Chapter 3, **RSMs** are employed to analyze the strain distribution in the thin films. A clear understanding of the measurement requires first grasping the physical meaning of the *reciprocal space*. A crystal is formed by atoms arranged in a periodic fashion, whose geometry can be described by the real-space lattice defined by the basis vectors $\mathbf{a}_1$, $\mathbf{a}_2$, and $\mathbf{a}_3$ (in units of Å). However, for probing phenomena such as X-ray diffraction or electron diffraction, the periodicity of the structure is more conveniently represented in reciprocal space.

The reciprocal lattice is a mathematical construct derived from the real-space lattice, with its basis vectors $\mathbf{b}_1$, $\mathbf{b}_2$, and $\mathbf{b}_3$ (in units of Å^{-1}) defined as

$$\mathbf{b}_1 = 2\pi \frac{\mathbf{a}_2 \times \mathbf{a}_3}{\mathbf{a}_1 \cdot (\mathbf{a}_2 \times \mathbf{a}_3)}, \quad \mathbf{b}_2 = 2\pi \frac{\mathbf{a}_3 \times \mathbf{a}_1}{\mathbf{a}_1 \cdot (\mathbf{a}_2 \times \mathbf{a}_3)}, \quad \mathbf{b}_3 = 2\pi \frac{\mathbf{a}_1 \times \mathbf{a}_2}{\mathbf{a}_1 \cdot (\mathbf{a}_2 \times \mathbf{a}_3)}, \tag{2.7}$$

where $\mathbf{a}_1 \cdot (\mathbf{a}_2 \times \mathbf{a}_3) \equiv V$ is the volume of the real-space unit cell (in Å^3), and the factor 2π ensures phase periodicity between reciprocal- and real-space lattices.

Any reciprocal-lattice point can be expressed as

$$\mathbf{G}_{hkl} = h\,\mathbf{b}_1 + k\,\mathbf{b}_2 + l\,\mathbf{b}_3, \tag{2.8}$$

where h, k, and l are the dimensionless Miller indices specifying the lattice point, and $\mathbf{G}_{hkl}$ is the corresponding reciprocal-lattice vector (in Å^{-1}) aligned with the

normal of the (hkl) plane in real space. Its magnitude satisfies $|\mathbf{G}_{hkl}| = 2\pi/d_{hkl}$, with d_{hkl} the interplanar spacing (in Å) of the (hkl) planes.

In diffraction experiments, the scattering vector $\mathbf{Q}$ is defined as the difference between the outgoing and incoming wave vectors. Its in-plane (Q_x) and out-of-plane (Q_z) components can be directly related to the instrument angles. For asymmetric reflections, a common transformation reads

$$Q_x = \frac{2\pi}{\lambda}\left[\cos(2\theta - \omega) - \cos\omega\right], \quad Q_z = \frac{2\pi}{\lambda}\left[\sin(2\theta - \omega) + \sin\omega\right], \tag{2.9}$$

where λ is the X-ray wavelength (in Å), and ω and 2θ are the instrument angles (in degrees, converted to radians for computation). Here, Q_x (in Å^{-1}) denotes the projection of $\mathbf{Q}$ parallel to the sample surface, while Q_z (in Å^{-1}) denotes the projection along the surface normal.

In Chapter 3, to facilitate a direct visualization of the epitaxial relationship, the horizontal and vertical axes of the RSMs have been converted from (Q_x, Q_z) to the Miller indices of the substrate. Given the known epitaxial orientation, the corresponding (hkl) values for the film peaks can thus be readily determined from the same transformation.

X-ray reflectivity (XRR) enables high-precision, non-destructive determination of thin-film thickness (d) by analyzing the interference fringes in the reflected intensity as a function of incident angle. When X-rays impinge on a thin film, reflections occur at both the surface and internal interfaces. The optical path difference between two reflected beams is

$$\Delta = 2d\sin\theta.$$

Constructive or destructive interference occurs when Δ satisfies the corresponding phase condition, producing the characteristic *Kiessig fringes* in the reflectivity curve. At small angles, the fringe spacing $\Delta\theta$ is approximately related to the film thickness d by

$$d \approx \frac{\lambda}{2\left(\sin\theta_{m+1} - \sin\theta_m\right)},$$

where λ is the X-ray wavelength and θ_m and θ_{m+1} are the angles of two adjacent fringe extrema. This expression is a first-order approximation, valid for single-layer films with smooth interfaces and weak absorption.

In real thin-film structures, interfacial roughness, absorption, multilayer stacking, and density variations must be taken into account. A full reflectivity model, such as the *Parratt recursion*, is therefore employed: (1) The film stack is divided into N layers, each characterized by thickness d_i, electron density ρ_i, and interfacial

roughness σ_i. (2) The refractive index of each layer is calculated from the electron density as

$$n_i = 1 - \delta_i + i\beta_i, \quad \delta_i \propto \rho_i.$$

(3) For each incident angle, the reflection coefficients are computed for all interfaces and combined recursively to yield the total reflectivity $R(\theta)$. (4) The parameters d_i, ρ_i, and σ_i are iteratively adjusted to minimize the deviation between the calculated and measured curves via least-squares fitting.

In this fitting process, the *fringe period* is primarily determined by the layer thickness, governing the oscillation frequency; the *fringe decay rate* is controlled by interfacial roughness and absorption; and the *fringe phase* depends on both thickness and density, dictating the positions of maxima and minima.

Raman spectroscopy is employed in this study to probe the vibrational modes of the material, thereby providing complementary structural information. In the experiment, a laser illuminates the sample and induces inelastically scattered light, which is spectrally dispersed and detected to yield the Raman signal. Raman scattering is a nonelastic light–matter interaction. As illustrated schematically in Figure **2.1**, scattering processes are classified as either elastic or inelastic: Rayleigh scattering is elastic, with the scattered frequency identical to that of the incident light; Stokes scattering corresponds to a loss of photon energy; and anti-Stokes scattering corresponds to a gain of photon energy.

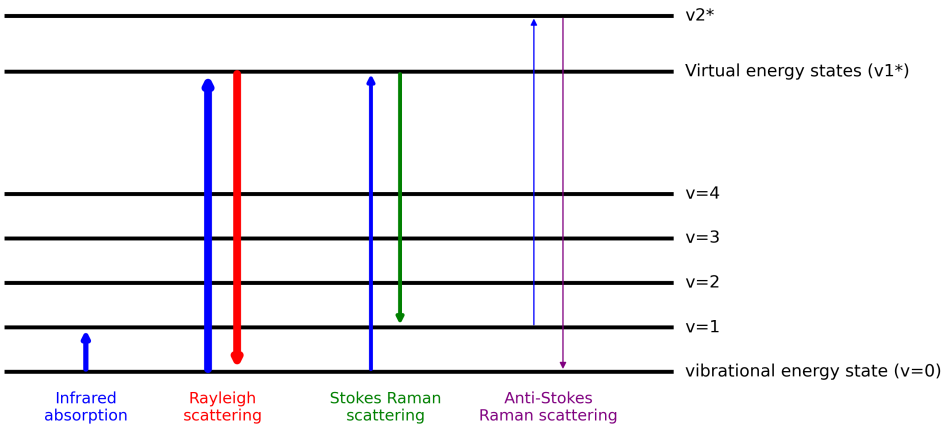

Figure 2.1: Schematic illustration of Rayleigh, Stokes, and anti-Stokes scattering.

From a quantum perspective, an incident photon of frequency ν_0 excites a vibrational mode of the crystal, driving the system from the ground state through a virtual level to a final state. The energy mismatch manifests as a Raman shift,

with the scattered frequency given by

$$\nu_{\text{Raman}} = \nu_0 \pm \nu_m, \tag{2.10}$$

where ν_{Raman} is the scattered frequency and ν_m is the characteristic vibrational or rotational frequency. The minus sign denotes Stokes scattering, and the plus sign denotes anti-Stokes scattering.

The Raman selection rule requires that the generalized vibrational coordinate Q modulate the polarizability tensor $\boldsymbol{\alpha}$, i.e., $\mathrm{d}\boldsymbol{\alpha}/\mathrm{d}Q \neq 0$. Under this condition, the scattering intensity is approximately

$$I \propto |\alpha|^2 I_0, \tag{2.11}$$

where I is the scattered intensity (arbitrary units), α is the effective component of the polarizability tensor (dimensionless), and I_0 is the incident intensity (arbitrary units). In practice, the Raman shift is expressed in terms of wavenumber displacement $\Delta\tilde{\nu}$ (cm^{-1}), which is related to the energy difference E (eV) by

$$E = hc\,\Delta\tilde{\nu}, \qquad 1\ \mathrm{cm}^{-1} \approx 0.124\ \mathrm{meV}, \tag{2.12}$$

where h is Planck's constant (J·s) and c is the speed of light in vacuum ($\mathrm{m{\cdot}s}^{-1}$). Since molecules predominantly occupy the ground state at room temperature, the Stokes signal is far stronger than the anti-Stokes signal, and thus routine Raman measurements focus almost exclusively on Stokes lines.

Intuitively, the Raman shift serves as a "fingerprint" of crystal vibrations. Each chemical bond and lattice vibration is associated with a characteristic frequency ν_m, which appears as a distinct spectral feature. These features provide insight into bond type, symmetry, and local structure, and are highly sensitive to stress, defects, and phase transitions in crystals. Raman spectroscopy therefore offers a nondestructive probe of the microscopic structure and dynamics of crystalline materials, with the peak position, intensity, and linewidth yielding critical information for materials characterization.

Spectroscopic ellipsometry (SE). Ellipsometry determines the complex reflectance ratio

$$\rho(\lambda,\theta) = \frac{r_p}{r_s} = \tan\Psi\, e^{i\Delta}, \tag{2.13}$$

where r_p and r_s are the Fresnel reflection coefficients for p- and s-polarized light at incidence angle θ and wavelength λ. The ellipsometric parameters Ψ and Δ represent the amplitude ratio and phase difference, respectively. For a stratified stack (ambient/film/substrate), $r_{p,s}$ are computed using the characteristic-matrix

(transfer-matrix) formalism. For a single film of thickness d and complex refractive index $\tilde{n}_f = n_f + ik_f$ on a substrate of $\tilde{n}_s$,

$$r_{p,s} = \frac{r_{01}^{p,s} + r_{12}^{p,s}\, e^{2i\beta}}{1 + r_{01}^{p,s} r_{12}^{p,s}\, e^{2i\beta}}, \qquad \beta = \frac{2\pi}{\lambda}\, \tilde{n}_f\, d \cos\theta_f, \tag{2.14}$$

where θ_f is the refracted angle in the film given by Snell's law, and $r_{ij}^{p,s}$ are the Fresnel coefficients at interface i–j.

Measured spectra $\{\Psi(\lambda),\Delta(\lambda)\}$ are regressed against model spectra by minimizing a weighted least-squares merit function

$$\chi^2 = \sum_i w_i \Big[\left(\Psi_i - \Psi_i^{\mathrm{mod}}\right)^2 + \left(\Delta_i - \Delta_i^{\mathrm{mod}}\right)^2 \Big]. \tag{2.15}$$

Here, VO_2 is taken as an example to illustrate the specific fitting procedure in layer model. We use a three-layer stack: ambient/VO_2 film/rutile TiO_2(110) substrate. Surface roughness, when needed, is represented by an effective-medium approximation (EMA) layer of thickness d_{rough} whose dielectric function $\varepsilon_{\mathrm{EMA}}$ is obtained from a 50/50 Bruggeman mixing of void and film.

Dispersion models and retrieval of n,k. **SE** does not invert n and k directly; instead, a causal dielectric function $\varepsilon(\omega) = \varepsilon_1 + i\varepsilon_2$ is parameterized and fitted to the measured spectra. After regression, n and k are calculated from

$$|\varepsilon| = \sqrt{\varepsilon_1^2 + \varepsilon_2^2}, \quad n = \sqrt{\frac{|\varepsilon| + \varepsilon_1}{2}}, \quad k = \sqrt{\frac{|\varepsilon| - \varepsilon_1}{2}}. \tag{2.16}$$

For insulating M_1-VO_2, we employ the Tauc–Lorentz (TL) model:

$$\varepsilon_2^{\mathrm{TL}}(E) = \begin{cases} \dfrac{A\, C\, E_0\, (E - E_g)^2}{E\left[(E^2 - E_0^2)^2 + C^2 E^2\right]}, & E > E_g, \\ 0, & E \le E_g, \end{cases} \tag{2.17}$$

with $\varepsilon_1(E)$ obtained by Kramers–Kronig integration, where A is the oscillator amplitude, C is the broadening, E_0 is the resonance energy, and E_g is the optical band gap. For metallic R-VO_2, a Drude+Lorentz (DL) model is used:

$$\varepsilon(\omega) = \varepsilon_\infty - \frac{\omega_p^2}{\omega(\omega + i\gamma)} + \sum_j \frac{A_j E_j^2}{E_j^2 - \omega^2 - i\Gamma_j \omega}, \tag{2.18}$$

where ε_∞ is the high-frequency dielectric constant, ω_p the plasma frequency, γ the damping (scattering rate), and A_j,E_j,Γ_j the strength, resonance energy, and broadening of the jth Lorentz oscillator.

Film thickness determination. The interference phase $\beta \propto \tilde{n}_f d$ controls the oscillations of Ψ and Δ. Broadband spectra provide multiple fringes: the fringe period constrains d, while the envelope and phase constrain n,k. To reduce correlation between d and n, we (i) include ex-situ thickness priors (profilometry/XRR) as bounds when available, (ii) first anchor d in weakly absorbing regions before refining dispersion in absorbing regions.

Band gap extraction. Two routes are used for M_1-VO_2: (1) the TL parameter E_g gives the optical gap directly; (2) from fitted $k(E)$ we compute $\alpha(E) = 4\pi k/\lambda$ and construct a Tauc plot of $(\alpha E)^{1/m}$ vs E ($m = 2$ for indirect-like, $m = 1/2$ for direct-like), whose linear extrapolation yields E_g.

Electrical resistivity was measured using a four-point probe configuration in conjunction with a custom-built resistance measurement setup. Although direct resistivity measurements were not possible, sheet resistance R was determined, and resistivity ρ was calculated via

$$\rho = R \cdot W \cdot F(w/s), \tag{2.19}$$

where W is the film thickness and $F(w/s)$ is a geometric correction factor.

Optical transmittance was recorded using a PerkinElmer Lambda 900 UV–Vis–NIR spectrophotometer, integrated with a custom temperature-controlled sample stage. The instrument employs a dual-beam configuration to eliminate fluctuations in source intensity. During measurements, the broadband light was filtered through a double-monochromator and directed onto the sample, while the transmitted beam was collected and compared to a reference.

The integrated luminous transmittance (T_{lum}, 380–780 nm), infrared transmittance (T_{IR}, 780–2500 nm), and solar transmittance (T_{sol}, 300–2500 nm) were calculated from the recorded spectra according to

$$T_{\mathrm{lum}} = \frac{\int_{380}^{780} \varphi(\lambda) E_\lambda T(\lambda)\, d\lambda}{\int_{380}^{780} \varphi(\lambda) E_\lambda\, d\lambda}, \tag{2.20}$$

$$T_{\mathrm{IR}} = \frac{\int_{780}^{2500} E_\lambda T(\lambda)\, d\lambda}{\int_{780}^{2500} E_\lambda\, d\lambda}, \tag{2.21}$$

$$T_{\mathrm{sol}} = \frac{\int_{300}^{2500} E_\lambda T(\lambda)\, d\lambda}{\int_{300}^{2500} E_\lambda\, d\lambda}, \tag{2.22}$$

where $T(\lambda)$ is the measured film transmittance, $\varphi(\lambda)$ is the standard luminous efficiency function for the photopic vision of human eyes, and E_λ is the solar spectral irradiance (AM1.5).

The modulation of luminous, infrared, and solar transmittance between the low-temperature (25°C) and high-temperature (85°C) states was determined as

$$\Delta T_{\mathrm{lum}} = T_{\mathrm{lum,25°C}} - T_{\mathrm{lum,85°C}}, \tag{2.23}$$

$$\Delta T_{\mathrm{IR}} = T_{\mathrm{IR,25°C}} - T_{\mathrm{IR,85°C}}, \tag{2.24}$$

$$\Delta T_{\mathrm{sol}} = T_{\mathrm{sol,25°C}} - T_{\mathrm{sol,85°C}}. \tag{2.25}$$

The temperature control stage includes a copper sample mount with a central aperture, enabling high thermal conductivity and optical access. Samples are clamped to the stage for stability. LabVIEW-based software enables real-time monitoring and automated temperature-dependent transmittance measurements across full spectra or at selected wavelengths.

3 Publication 1: Correlation of MIT and strain state of VO_2 thin films on TiO_2 (110) substrates

This chapter explores the possibility of tuning the metal-to-insulator transition (MIT) of crystalline VO_2 thin films by strain engineering. We deposit high-quality VO_2 epitaxial films of different thicknesses on TiO_2 (110) substrates by pulsed laser deposition. The strain state of the deposited film varies with its thickness. This allows us to correlate the MIT characteristics with the strain state of the VO_2 film by a careful characterization of the structural and electrical properties. Thin VO_2 films on TiO_2 (110) substrates are almost fully strained up to thicknesses of about 20 nm and exhibit tensile strain along the *c*-axis of the (high-temperature) metallic rutile phase, leading to an increase of the MIT temperature by as much as 30 °C in comparison to the almost fully relaxed 300 nm-thick VO_2 film. The strain gradient within the thicker samples leads to a continuous serial switching of layered regions of the VO_2 film from the insulating to the metallic state with increasing temperature.

In order to achieve in-plane strain along the c-axis of the VO_2 thin films, we prepared a series of VO_2 epitaxial films on rutile TiO_2 (110) substrates with various thicknesses by PLD and studied the strain relaxation as a function of film thickness. VO_2 thin films were deposited using a KrF excimer laser (Lambda Physik COMPEX PRO 205 F, $\lambda = 248$ nm) as the ablation source. The laser pulse energy was fixed at 600 mJ/pulse with a repetition rate of 5 Hz. A high-purity (99.999%) VO_2 ceramic disk was used as the ablation target. Additional O_2 gas was introduced into the chamber as the reactive atmosphere. All samples were grown under identical conditions, with the film thickness controlled solely by varying the number of laser pulses during deposition. The O_2 pressure was maintained at 1.0 Pa during the growth process.

TiO_2 (110) substrates were ultrasonically cleaned in acetone, ethanol, and deionized water, each for 15 minutes, and immediately transferred into the deposition chamber after drying with nitrogen gas. The target-to-substrate distance was set to 6 cm. The base pressure of the chamber was maintained at 1×10^{-4} Pa before

introducing the O_2 gas. The substrate temperature during deposition was fixed at 600 °C. By varying the number of laser pulses from 500 to 18000, we obtained a series of VO_2 films with thicknesses ranging from 7 nm to 300 nm

X-ray diffraction (XRD) and reciprocal space mapping (RSM) were performed for the structural characterization of the deposited VO_2 films using a four-circle X-ray diffractometer (Bruker D8 Discover) with Cu Kα radiation ($\lambda = 1.5406$ Å).

The sample's electrical resistance was measured in a linear four-probe configuration between 25 °C and 90 °C to investigate the electrical switching properties of the VO_2 films.

Cross-sectional samples of the VO_2 thin films on rutile TiO_2 (110) substrates for transmission electron microscopy (TEM) analysis were prepared using an FEI Helios 600 dual-beam instrument via standard lift-out and polishing procedures. After polishing, the samples were cleaned using a Gatan 691 PIPS at 0.8 keV to remove residual contamination and possible surface damage.

High-angle annular dark-field (HAADF, 64 mrad $< \beta <$ 180 mrad) images were acquired in scanning-TEM mode using a JEM Grand ARM300F microscope equipped with double spherical aberration (Cs) correctors.

This work was published in *Applied Physics Letters* **123**, 042103 (2023), titled "**Correlation of metal-to-insulator transition and strain state of VO_2 thin films on TiO_2 (110) substrates**". The article published online on July 24, 2023. **DOI:** 10.1063/5.0152809

The VO_2 samples in this study were fabricated and characterized by Hao Lu. Lei Li, Zhiwu Tang, Maji Xu, Yinmei Lu, Mingkai Li, and Pai Li contributed to the early-stage discussions of the experimental design. Yonghui Zheng carried out the TEM characterization, and Zaoli Zhang performed the TEM data analysis. This work benefited greatly from extensive scientific discussions among all authors. In particular, the contributions of Martin Becker, Yunbin He and Peter J. Klar were essential for the interpretation and understanding of the results, as well as for providing valuable guidance on the subsequent experimental and theoretical investigations.

Copyright Permission Statement

I hereby declare that the copyright permission from the publisher was obtained prior to reproducing the previously published article in this dissertation.

Applied Physics Letters ARTICLE pubs.aip.org/aip/apl

Correlation of metal-to-insulator transition and strain state of VO_2 thin films on TiO_2 (110) substrates

Cite as: Appl. Phys. Lett. **123**, 042103 (2023); doi: 10.1063/5.0152809
Submitted: 1 April 2023 · Accepted: 7 July 2023 ·
Published Online: 24 July 2023

View Online Export Citation CrossMark

Hao Lu,[1,2,a)] Lei Li,[1] Zhiwu Tang,[1] Maji Xu,[1] Yonghui Zheng,[3] Martin Becker,[2] Yinmei Lu,[1] Mingkai Li,[1] Pai Li,[1] Zaoli Zhang,[3,a)] Peter J. Klar,[2] and Yunbin He[1,a)]

AFFILIATIONS

[1]Ministry-of-Education Key Laboratory of Green Preparation and Application for Functional Materials, Hubei Key Lab of Ferro & Piezoelectric Materials and Devices, Hubei Key Laboratory of Polymer Materials, and School of Materials Science & Engineering, Hubei University, Wuhan 430062, China
[2]Institute of Experimental Physics I and Center of Materials Research (ZfM/LaMa), Justus Liebig University Giessen, Giessen, Germany
[3]Erich Schmid Institute of Materials Science, Austrian Academy of Sciences, A-8700 Leoben, Austria

[a)]**Authors to whom correspondence should be addressed:** hao.lu@physik.uni-giessen.de; zaoli.zhang@oeaw.ac.at; and ybhe@hubu.edu.cn

ABSTRACT

We explore the possibility of tuning the metal-to-insulator transition (MIT) of crystalline VO_2 thin films by strain engineering. We deposit high-quality VO_2 epitaxial films of different thicknesses on TiO_2 (110) substrates by pulsed laser deposition. The strain state of the deposited film varies with its thickness. This allows us to correlate the MIT characteristics with the strain state of the VO_2 film by a careful characterization of the structural and electrical properties. Thin VO_2 films on TiO_2 (110) substrates are almost fully strained up to thicknesses of about 20 nm and exhibit tensile strain along the *c* axis of the (high-temperature) metallic rutile phase leading to an increase in the MIT temperature by as much as 30 °C in comparison to the almost fully relaxed 300 nm-thick VO_2 film. The strain gradient within the thicker samples leads to a continuous serial switching of layered regions of the VO_2 film from the insulating to the metallic state with increasing temperature.

In the vicinity of 68 °C, crystalline bulk vanadium dioxide (VO_2) undergoes a reversible structural phase transition from the high-temperature (HT) rutile phase to the low-temperature (LT) monoclinic phase which is accompanied by a metal-to-insulator transition (MIT).[1–3] When approaching the critical temperature T_C of the phase transition from below, the resistivity decreases by as much as five orders of magnitude at T_C,[4] and the optical transmittance in the near-infrared (NIR) region decreases significantly due to an increase in the reflectivity. Both effects are induced by the much increased free carriers in the metallic phase. Today, considerable effort is made to understand and manipulate the MIT in VO_2 thin films because such films serve as active functional materials in numerous device concepts, such as smart glass, storage media, and ultrafast switches.[5–7] There are many ways to tune the T_C of the MIT, such as doping and lattice strain.[8–11] In the case of high-quality epitaxial films, a variation of the MIT temperature can be achieved while keeping an abrupt phase transition in a narrow temperature window. Thus, a broad transition and a hysteresis of the switching between up- and down-sweep can be avoided. Such broadening often occurs when the transition temperature is tuned by doping.[12] Some studies address this issue by comparing the structural transition behavior of pure and doped VO_2 thin films grown on sapphire (Al_2O_3) substrates with the VO_2 bulk material.[13–15] An effective tuning of the transition temperature by strain is best achieved in the case of pseudomorphic growth of a crystalline thin film on a crystalline substrate of the same crystal structure and slightly different lattice constants. For example, rutile TiO_2 possesses the same crystal structure as the high-temperature VO_2 phase and comparable lattice parameters. Therefore, rutile TiO_2 substrates offer ideal conditions for the pseudomorphic growth of VO_2 thin films. Zhang *et al.* were the first to systematically study VO_2 films on TiO_2 substrates by transmission electron microscopy (TEM).[16] Basically, the MIT temperature of VO_2 varies with the spacing along the chain of V-atoms whose direction corresponds to the *a* and *c* axes of the monoclinic- and rutile-phase, respectively. Muraoka *et al.* reported that

compressive strain along the *c* axis of very thin VO_2 films on rutile TiO_2 (100) and (110) substrates induced a reduction in the MIT temperature.[17] Zou *et al.* confirmed that the temperature of MIT in the interface region of epitaxial VO_2 films grown on rutile TiO_2 (001) using oxide molecular beam epitaxy depends on the strain state.[18] It should be noted that for VO_2 thin films pseudomorphically grown on crystalline TiO_2 substrates of various orientations different strain states can be induced. In the case of TiO_2 (001) substrates, the *c* axis is perpendicular to the substrate surface and the VO_2 layer is biaxially strained. In contrast, the *c* axis lies in the substrate plane when TiO_2 (110) substrates are used and the in-plane strains are not the same in the directions parallel and perpendicular to the *c* axis. As yet, a systematic analysis of the intrinsic relationship between lattice strain and MIT is lacking. However, a thorough understanding of the strain effects is essential for exploiting such a correlation in device concepts.

In this work, we prepared a series of VO_2 epitaxial films on rutile TiO_2 (110) substrates of various thicknesses by pulsed laser deposition (PLD) and studied the strain relaxation with increasing film thickness. VO_2 thin-film samples were deposited on rutile TiO_2 (110) substrates by PLD employing a KrF excimer laser (Lambda Physik COMPEX PRO 205 F, $\lambda = 248$ nm) as the ablation source. The laser beam energy was fixed at 600 mJ/pulse at a pulse repetition rate of 5 Hz. A VO_2 ceramic disk of high-purity (99.999%) was used as an ablation target. Additional O_2 gas was introduced into the chamber as reactive gas. The same growth conditions were used for all samples, only the number of pulses in the ablation process was varied to obtain different sample thicknesses. The O_2 pressure was kept at 1.0 Pa during the film growth. The TiO_2 (110) substrates were cleaned ultrasonically in acetone, ethanol, and de-ionized water, each for 15 min, and then transferred into the deposition chamber immediately after blow-dry with nitrogen gas. The target–substrate distance was set to 6 cm. The base pressure in the chamber was 1×10^{-4} Pa prior to letting in the O_2 reactive gas. The substrate temperature during the deposition was fixed at 600 °C. By varying the number of pulses in the ablation process from 500 to 18 000, we obtained a series of VO_2 films with thicknesses of 7 to 300 nm.

X-ray diffraction (XRD) and reciprocal space mapping (RSM) using a four-circle x-ray diffractometer (Bruker, D8 discover) with Cu $K\alpha$ radiation ($\lambda = 1.5406$ Å) were performed for the structural characterization of the deposited VO_2 films. The sample's electrical resistance in a linear configuration of four contacts is measured between 25 and 90 °C to investigate the electrical switching properties of the VO_2 films. Cross-sectional samples of the VO_2 thin films on rutile TiO_2 (110) substrates for TEM analyses were prepared in an FEI Helios 600 instrument with a standard lift-out and polishing process. After polishing, the samples were cleaned in a Gatan 691 PIPS at 0.8 keV to remove the residual contamination and possible damage. The high-angle annular dark-field (HAADF, $64 < \beta < 180$ mrad) images were recorded using the scanning-TEM mode of the JEM Grand ARM300F microscope with double spherical aberration (Cs) correctors.

Figure 1(a) depicts ω–2θ–XRD traces of VO_2 films of various thicknesses between 7 and 300 nm. The film thicknesses were determined by x-ray reflection for films with thicknesses below 100 nm, and for thicker films, the thickness was estimated using the growth rate per laser pulse established for the thinner samples (see Fig. S1 of the supplementary material). The lattice parameters of the rutile TiO_2 substrate ($a = b = 4.593$ and $c = 2.959$ Å) and of the rutile VO_2 ($a = b = 4.554$ and $c = 2.855$ Å) are very close.[19,20] In the case of pseudomorphic growth on a TiO_2 (110) substrate, the VO_2 films should experience an anisotropic in-plane strain (0.85% along the $[1\text{–}10]_r$

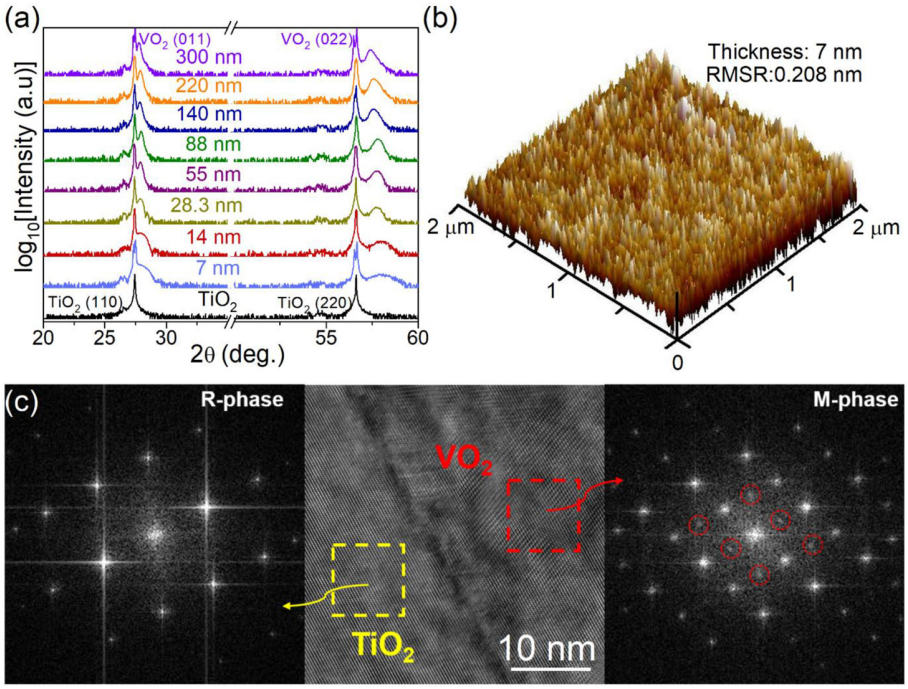

FIG. 1. (a) ω–2θ XRD traces of VO_2 films deposited on (110) TiO_2 substrates with various thicknesses. (b) AFM image of the surface of the 7 nm VO_2 film. (c) HRTEM image in the vicinity of the VO_2/TiO_2 interface of a sample with a 20 nm VO_2 film and corresponding FFT patterns.

direction and 3.5% along the $[001]_r$ direction) induced by the TiO_2 (110) substrates. The XRD traces show clear features of the VO_2 film in addition to the diffraction peaks from the TiO_2 (110) substrate. The two peaks close to 28° and 57° are assigned to diffraction from the monoclinic VO_2 $(011)_m$ and $(022)_m$ planes, respectively. No sign of polycrystalline or amorphous phases is present in the diffractogram, which demonstrates that a VO_2 film with domains of single orientation was prepared. Furthermore, we characterized the surface morphology of all grown VO_2 films by atomic force microscopy (AFM). Figure 1(b) shows an exemplary AFM image of the VO_2 film with a thickness of 7 nm. The surface of the film is dense and homogeneous, exhibiting small grains only. The root mean square roughness of all films averaged over a $2 \times 2\,\mu m^2$ surface area increases from 0.2 to 0.99 nm, when the film's thickness increases from 7 to 300 nm. Thus, all films grown can be considered smooth. Additional AFM images can be found in Fig. S2 of the supplementary material. The high-resolution TEM (HRTEM) data in Fig. 1(c) and the corresponding fast Fourier transformation (FFT) pattern confirm the assignment of the structures in the XRD analyses.

In Fig. 2(a), we zoom in into the region of ω–2θ XRD traces corresponding to the $(022)_m$ peak of monoclinic VO_2. The diffraction peak in the range from 58.05° to 57.44° depending on the VO_2 thickness is assigned to the monoclinic VO_2 $(022)_m$ plane, rather than the rutile $(220)_r$ plane. It is important to note for what follows that, according to this assignment, the c axis of the HT rutile phase of the VO_2 films deposited lies in the film plane. The ω–2θ XRD traces probe the lattice spacings of the VO_2 films in the growth direction, i.e., perpendicular to the c axis. In the case of pseudomorphic growth, the VO_2 film lattice is under tensile strain along the in-plane c axis of the HT rutile phase, as discussed above. Consequently, the lattice of the VO_2 film in the growth direction is expected to be compressively strained. As seen in Fig. 2(a), the $(022)_m$ diffraction peaks of the deposited VO_2 films of different thicknesses are located at various angles, which are all somewhat higher than that of the VO_2 bulk material (57.43° according to JCPDS No. 431051). This means that the $(022)_m$-plane interplanar spacings of all the deposited VO_2 films are shrunk relative to that of bulk VO_2. Thus, all the VO_2 films lattices are, indeed, under compressive strain as expected. With the increasing film thickness from 7 to 300 nm, the VO_2 $(022)_m$ diffraction peak gradually shifts to lower angles, indicating a continuous increase in the $(022)_m$ interplanar spacing and hence gradual relaxation of the compressed monoclinic VO_2 $(022)_m$ lattice along the film growth direction. The very thin VO_2 films of 7 and 14 nm thicknesses show an almost identical (022)m diffraction angle of 58.05° and can be regarded as fully strained to fit the TiO_2 (110) substrate. The strain energy builds up with increasing film thickness. At a critical film thickness of about 20 nm, the deposited VO_2 films start to relax, and their (022)m interplanar spacings approach continuously that of unstrained VO_2 bulk material. Almost complete relaxation has occurred at the film thickness of 300 nm. However, the $(022)_m$ diffraction peak of the 300 nm-thick VO_2 film is not symmetric, showing a pronounced tail on its right. This asymmetry of the diffraction peak reflects the strain distribution within the film, i.e., the strain state of the film gradually varies from the substrate–film interface toward the film surface. Thus, in thicker VO_2 films, this transition of the strain state can be roughly approximated by three regions with different strain states: fully strained (almost pseudomorphic growth), partially relaxed, and (almost) fully relaxed [corresponding positions of the $(022)_m$ diffraction peaks are indicated by red lines in Figs. 2(a) and 2(b)].

Figure 2(b) shows the results of RSM taken at 30 °C, i.e., below T_C where the VO_2 films are still in their LT monoclinic phase. The diffraction spots corresponding to the (220) planes of the rutile TiO_2

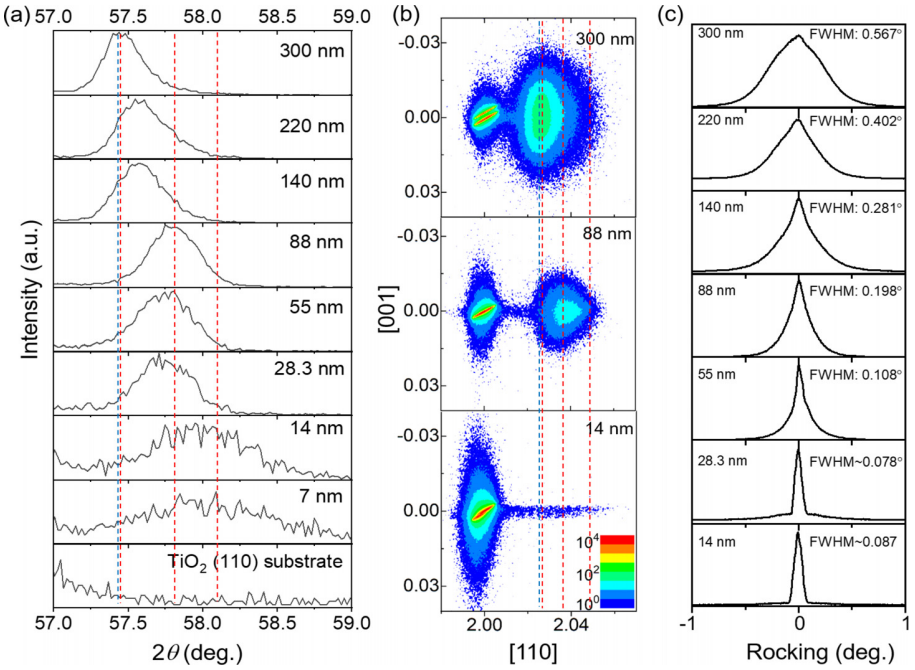

FIG. 2. (a) Zoom in ω–2θ XRD patterns of VO_2 films. (b) RSM images in the vicinity of the $(022)_m$ diffraction peak of the VO_2 films. (c) Rocking curves of the VO_2 $(011)_m$ plane of all films. All data were recorded at 30 °C.

substrate are visible on the left-hand side of the maps, and the diffraction spots of VO_2 $(022)_m$ planes occur on the right-hand side. The position of VO_2 $(022)_m$ diffraction spot gradually shifts toward to that of bulk VO_2 with the increasing film thickness from 14 via 88 to 300 nm, reflecting that the average strain in the film decreases with the increasing film thickness. The RSM results corroborate the $(022)_m$ peak shift trend of the ω–2θ XRD traces. In addition, we performed rocking-curve XRD measurements of $(011)_m$ planes to evaluate the out-of-plane atomic ordering of the deposited single-crystalline VO_2 films. The relation between the full width at half maximum (FWHM) of the XRD ω-scan rocking curves and the thickness of the VO_2 thin films is shown in Fig. 2(c). The FWHM increases from 0.078° to 0.567° when the film thickness increases from 28.3 to 300 nm. The increasing inhomogeneity and atomic disorder of the film can as well be interpreted in terms of the strain relaxation, which progresses with the increase in thickness.

Different strain states of the VO_2 lattice affect the phase transition temperature T_C of the MIT. The determination of T_C is not straightforward, in particular, when the transition takes place in a broader temperature window due to inhomogeneity of the VO_2 sample, e.g., in our case, due to a strain distribution along the growth direction of the VO_2 film. There are different ways of defining and determining a value for T_C in such cases, which lead to slightly different values, but reveal similar trends. Here, we focus on the change in the film resistivity ρ with temperature and determine T_C by the average of the positions of the minima of plots $d(\log\rho)/dT$ vs T measured during heating and cooling of the sample. Corresponding plots of resistivity ρ and $d(\log\rho)/dT$ vs T are shown in Figs. 3(a) and 3(b), respectively, for the samples with thicknesses of 7, 88, and 300 nm. The $d(\log\rho)/dT$ curves of all VO_2 films studied are shown in Fig. S3 of the supplementary material.

The thinnest VO_2 film with a thickness of 7 nm exhibits the highest T_C of 75.6 °C, which is anticipated from the XRD analysis as it possesses the longest c lattice parameter in the rutile phase due to the tensile strain in-plane of the film. Although strain relaxation sets in already at a film thickness of 14 nm, which leads to a slightly lowered T_C (74.8 °C). Drastic T_C drop occurs at the film thicknesses between 14 and 28.3 nm. T_C is already lowered down to about 55 °C at a thickness of 88 nm and further down to 49.4 °C for the 300 nm thick film. It is worth noting that the T_C values determined for the 88 and 300 nm VO_2 films are in concordance with the values revealed by RSM (see Fig. 4 for the 88 and 300 nm samples). Nevertheless, it is somewhat surprising that the T_C values of almost relaxed samples are lower than the T_C of bulk VO_2. As both methods yield similar results, we believe that the determined T_C values are reliable and this finding is due to non-stoichiometry, i.e., occurrence of oxygen vacancies in the deposited films, as reported by other researchers,[21,22] and confirmed by our x-ray photoelectron spectroscopy (XPS) measurements presented in Figs. S4 and S5. Nevertheless, Raman measurements in Fig. S6 of the supplementary material show that the deposited films are of M1-phase VO_2 despite the non-stoichiometry. Furthermore, the $d(\log\rho)/dT$ vs T curve exhibits an asymmetry for larger film thicknesses. A wing develops on the HT side of the minimum. This asymmetric minimum with the extended HT wing is clearly visible in the case of 88 nm film thickness and more pronounced in the 140 nm thick film (see Fig. S3 of the supplementary material) and further turns into a pronounced shoulder with virtually another minimum in the case of the thickest sample grown, i.e., the 300 nm VO_2 film. Thus, the shape of the $d(\log\rho)/dT$ curve reflects the strain distribution from the substrate-film interface to the film surface. The local strain state determines the local transition temperature inside the film. The layers parallel to the interface exhibit the same strain state, and the transition temperature decreases with increasing distance from the interface. Therefore, the metallic state across the entire film of the inhomogeneously strained samples is anticipated to be gradually established with the increasing temperature. It initializes in the vicinity of the film surface and finally reaches the layers close to the film–substrate interface. The samples with thicknesses in the range of 50–200 nm show the largest inhomogeneity due to strain. This is also reflected in Fig. 3(c), where the variation of $T_C = (T_{C,Heating} + T_{C,Cooling})/2$ with film thickness is plotted together with the thermal hysteresis width $\Delta T = T_{C,Heating} - T_{C,Cooling}$, in which $T_{C,Heating}$ and $T_{C,Cooling}$ are the transition temperatures determined at the minima of the $d(\log\rho)/dT$ curves corresponding to heating and cooling processes, respectively. Figure 3(d) illustrates schematically the three regions, namely, pseudomorphically/fully strained, partially relaxed, and fully relaxed, in the deposited VO_2 film as we proposed based on the above-mentioned discussions.

The *in situ* temperature-dependent high-resolution XRD-RSM results provide more evidence for the gradual structural phase

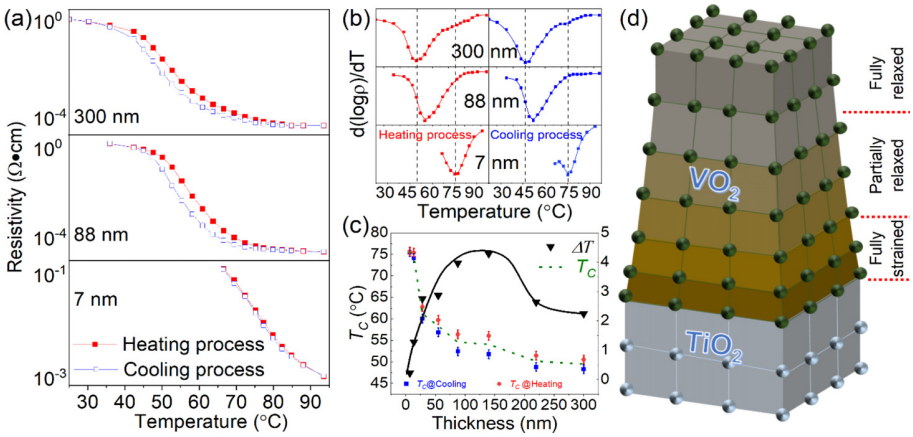

FIG. 3. (a) Temperature dependence of electrical resistivity. (b) Derivative curves (d[log (ρ)]/dT) as a function of temperature. (c) MIT transition temperature T_C and thermal hysteresis width ΔT as a function of film thicknesses. (d) Schematic illustration of the strain relaxation in a thick VO_2 thin film.

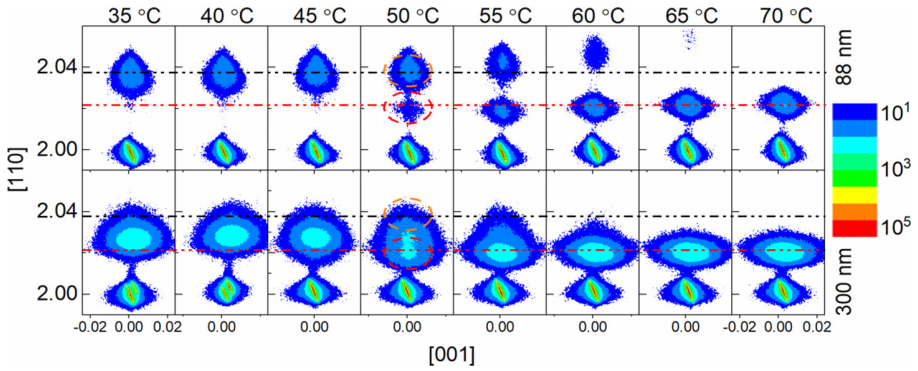

FIG. 4. RSM images of 88 and 300 nm thick VO_2 films on a rutile TiO_2 (110) substrate in the vicinity of the $(022)_m$ diffraction peak of monoclinic VO_2 as a function of temperature. The abscissae scales remain consistent, and to prevent the overlap of abscissa values in each image, only the complete values of the *x* axis for the panels on the far left and far right are displayed.

transition of the VO_2 films. Figure 4 shows RS maps obtained at various temperatures between 35 and 70 °C from the 88 and 300 nm thick VO_2 films with T_C of about 55 and 49.4 °C. The maps were recorded in the vicinity of the diffraction peak corresponding to $(022)_m$ planes of VO_2. The change in the central position of diffraction spots in reciprocal space mapping reflects the phase transition. Up to three diffraction spots can be discerned in maps associated with the phase transition. The bottom diffraction spot in the map corresponds to the (220) diffraction of the rutile TiO_2 substrate. The other two, one at the top and another in the middle of the map, disappears and appears, respectively, with increasing temperature. The top diffraction spot, which gradually fades away with increasing temperature, corresponds to the diffraction of $(022)_m$ planes of VO_2 in the LT monoclinic phase. The intermediate diffraction spot, which gradually appears with increasing temperature, arises from $(220)_r$ diffraction of VO_2 in the HT rutile phase. The position and intensity variation of diffraction spots of the 88 nm thick VO_2 film unanimously show that the phase transition gradually takes place in a rather broad temperature range between 50 and 65 °C. In this temperature range, both phases of VO_2, the metallic rutile phase and the insulating monoclinic phase, are present simultaneously in accordance with the interpretation of the temperature-dependent electrical measurements. At about 50 °C, metallic rutile-phase regions of the VO_2 film start to appear nearly the surface and at about 65 °C the last insulating monoclinic-phase regions close to the film–substrate interface lose their insulating character and become metallic. Between 30 and 45 °C, the VO_2 is solely in the insulating monoclinic-phase. Above 65 °C, the diffraction spot from the monoclinic (022) plane has disappeared, and the entire VO_2 film is transformed into the rutile phase. The phase transition exhibited by the 300 nm VO_2 film follows a comparable pattern. However, when comparing in detail the RSMs of both films at the same temperature in the vicinity of T_C, such as 50 °C, evident differences appear. For the 88 nm-thick film, the diffraction spot associated with the rutile structure is somewhat weaker in intensity than that corresponding to the monoclinic structure. Conversely, in the 300 nm film, the diffraction spot related to the rutile structure appears stronger than that associated with the monoclinic structure. This observation suggests that at 50 °C a greater number of regions are strain relaxed within the thicker film. These regions contribute to a lower overall phase transition temperature compared to the thinner film of 88 nm. The structural evolution deduced from RSMs recorded at different temperatures supports our proposal that the strain relaxation in VO_2 thin films grown on TiO_2 (110) substrates causes the reduction in the phase transition temperature of the film.

In summary, we provide further evidence that the phase transition temperature and the width of the temperature range where the MIT transition in VO_2 takes place depend on the strain distribution in the crystalline VO_2 layers. The strain distribution, in turn, depends on the choice of substrate, its orientation, and the thickness of the deposited VO_2 film. In particular, we demonstrate that the transition temperature in the case of crystalline VO_2 films deposited on TiO_2 (110) substrates can be varied by about 30 °C from above to below the T_C of bulk VO_2 when increasing the thickness of the deposited VO_2 film from 7 (almost fully strained) to 300 nm (almost fully relaxed). The strain gradient along the growth direction leads to a continuous serial switching of layer-like regions of the film into the metallic state with increasing temperature. The serial switching starts from the almost fully relaxed region near the surface and ends at the almost entirely strained region at the substrate–film interface.

See the supplementary material for XRR spectra, AFM images, and temperature-dependent electrical resistivity and derivative (d[log(ρ)]/dT) curves recorded during film heating and cooling for VO_2 films of various thicknesses; XPS survey and high-resolution spectra acquired for the 28.3 and 140 nm-thick films and Raman spectra of the 140 nm-thick VO_2 film and the TiO_2 substrate; and a table of FWHM, MIT temperature, RMSR, and the lattice parameters calculated from RSM measurements for VO_2 films of different thicknesses.

This work was supported by the National Natural Science Foundation of China (Grant Nos. 51572073, 11975093, and 62274057), the Sino-German Mobility Program (Grant No. M-0764), the Natural Science Foundation of Hubei Province (Grant Nos. 2019CFA006, 2021EHB005, and 2022EHB023), the Program for Science and Technology Innovation Team in Colleges of Hubei Province (Grant No. T201901), and the China Scholarship Council (award to Hao Lu for 3 year's study abroad at the University of Giessen). Furthermore, we acknowledge the support from the German BMBF (Grant No. 03VP09691), the Austrian innovation fund (with Project No. ÖAW 4023 Innovation funds), and DFG research grant 510965362.

AUTHOR DECLARATIONS

Conflict of Interest

The authors have no conflicts to disclose.

Author Contributions

Hao Lu: Conceptualization (equal); Data curation (equal); Formal analysis (equal); Investigation (equal); Methodology (equal); Writing – original draft (lead); Writing – review & editing (lead). **Zaoli Zhang:** Funding acquisition (equal); Writing – review & editing (equal). **Peter J. Klar:** Formal analysis (lead); Funding acquisition (lead); Supervision (lead); Writing – original draft (equal); Writing – review & editing (lead). **Yunbin He:** Formal analysis (lead); Funding acquisition (lead); Supervision (lead); Writing – original draft (equal); Writing – review & editing (lead). **Lei Li:** Conceptualization (equal); Data curation (equal); Methodology (equal); Writing – original draft (equal). **Zhiwu Tang:** Data curation (equal); Methodology (equal). **Maji Xu:** Data curation (equal); Methodology (equal). **Yonghui Zheng:** Data curation (equal); Formal analysis (equal). **Martin Becker:** Formal analysis (equal); Investigation (equal); Writing – review & editing (equal). **Yinmei Lu:** Conceptualization (equal); Funding acquisition (equal). **Mingkai Li:** Conceptualization (equal); Funding acquisition (equal). **Pai Li:** Funding acquisition (equal).

DATA AVAILABILITY

The data that support the findings of this study are available within the article and its supplementary material.

REFERENCES

[1]F. J. Morin, "Oxides which show a metal-to-insulator transition at the Neel temperature," Phys. Rev. Lett. **3**(1), 34 (1959).

[2]J. B. Goodenough, "The two components of the crystallographic transition in VO_2," J. Solid State Chem. **3**(4), 490–500 (1971).

[3]J. Narayan and V. M. Bhosle, "Phase transition and critical issues in structure-property correlations of vanadium oxide," J. Appl. Phys. **100**(10), 103524 (2006).

[4]H. S. Choi, J. S. Ahn, J. H. Jung, T. W. Noh, and D. H. Kim, "Mid-infrared properties of a VO_2 film near the metal-insulator transition," Phys. Rev. B **54**(7), 4621 (1996).

[5]F. Kuhl, M. Becker, S. L. Benz, J. Hauptmann, J. Kessler, S. Chatterjee, A. Polity, and P. J. Klar, "Embedding quaternary $V_{1-x-y}Sr_xW_yO_2$ into multilayer systems to enhance its thermochromic properties for smart glass applications," ACS Appl. Electron. Mater. **4**(1), 513–520 (2022).

[6]A. W. Smith, "Optical storage in VO_2 films," Appl. Phys. Lett **23**(8), 437–438 (1973).

[7]M. F. Becker, A. B. Buckman, R. M. Walser, T. Lépine, P. Georges, and A. Brun, "Femtosecond laser excitation of the semiconductor-metal phase transition in VO_2," Appl. Phys. Lett. **65**(12), 1507–1509 (1994).

[8]H. Lu, L. Chen, R. Cao, X. Tao, X. Wang, M. Li, P. Li, Y. Lu, P. J. Klar, and Y. He, "$RuVO_2$ alloy epitaxial films: Lowered insulator–metal transition temperature and retained modulation capacity," Appl. Phys. Lett **116**(19), 192103 (2020).

[9]J. Jian, X. Wang, L. Li, M. Fan, W. Zhang, J. Huang, Z. Qi, and H. Wang, "Continuous tuning of phase transition temperature in VO_2 thin films on c-cut sapphire substrates via strain variation," ACS Appl. Mater. Interfaces **9**(6), 5319–5327 (2017).

[10]H. Li, J. Wang, Z. You, Y. Yu, P. Li, L. Xiong, and Y. He, "Nb-doped VO_2 thin films with enhanced thermal sensing performance for uncooled infrared detection," Mater. Res. Bull. **146**, 111615 (2022).

[11]H. Guo, K. Chen, Y. Oh, K. Wang, C. Dejoie, S. A. Syed Asif, O. L. Warren, Z. W. Shan, J. Wu, and A. M. Minor, "Mechanics and dynamics of the strain-induced M1–M2 structural phase transition in individual VO_2 nanowires," Nano Lett. **11**(8), 3207–3213 (2011).

[12]X. Wang, L. Chen, H. Lu, W. Fang, H. Li, W. Yin, M. Li, Y. Lu, P. Li, and Y. He, "Enhancing visible-light transmittance while reducing phase transition temperature of VO_2 by Hf–W co-doping," Appl. Phys. Lett. **118**, 192102 (2021).

[13]P. Jin, M. Tazawa, K. Yoshimura, K. Igarashi, S. Tanemura, K. Macak, and U. Helmersson, "Epitaxial growth of W-doped VO_2/V_2O_3 multilayer on α-Al_2O_3 (110) by reactive magnetron sputtering," Thin Solid Films **375**(1–2), 128–131 (2000).

[14]J. M. Gregg and R. M. Bowman, "The effect applied strain resistance VO2 thin films," Appl. Phys. Lett. **71**(25), 3649–3651 (1997).

[15]V. Théry, A. Boulle, A. Crunteanu, J. C. Orlianges, A. Beaumont, R. Mayet, A. Mennai, F. Cosset, A. Bessaudou, and M. Fabert, "Role of thermal strain in the metal-insulator and structural phase transition of epitaxial VO_2 films," Phys. Rev. B **93**(18), 184106 (2016).

[16]Y. Zheng, Z. Chen, H. Lu, Y. Cheng, X. Chen, Y. He, and Z. Zhang, "The formation of TiO_2/VO_2 multilayer structure via directional cationic diffusion," Nanoscale **13**(16), 7783–7791 (2021).

[17]Y. Muraoka and Z. Hiroi, "Metal–insulator transition of VO_2 thin films grown on TiO_2 (001) and (110) substrates," Appl. Phys. Lett. **80**(4), 583–585 (2002).

[18]L. L. Fan, S. Chen, Z. L. Luo, Q. H. Liu, Y. F. Wu, L. Song, D. X. Ji, P. Wang, W. S. Chu, C. Gao, and C. W. Zou, "Strain dynamics of ultrathin VO_2 film grown on TiO_2 (001) and the associated phase transition modulation," Nano Lett. **14**(7), 4036–4043 (2014).

[19]H. E. Swanson, *Standard X-Ray Diffraction Powder Patterns* (U.S. Department of Commerce, National Bureau of Standards, 1953).

[20]K. D. Rogers, "An X-ray diffraction study of semiconductor and metallic vanadium dioxide," Powder Diffr. **8**(4), 240–244 (1993).

[21]S. Fan, L. Fan, Q. Li, J. Liu, and B. Ye, "The identification of defect structures for oxygen pressure dependent VO_2 crystal films," Appl. Surf. Sci. **321**, 464–468 (2014).

[22]Q. Lu, C. Sohn, G. Hu, X. Gao, M. F. Chisholm, I. Kylänpää, J. T. Krogel, P. R. Kent, O. Heinonen, P. Ganesh, and H. N. Lee, "Metal–insulator transition tuned by oxygen vacancy migration across TiO_2/VO_2 interface," Sci. Rep. **10**(1), 18554 (2020).

Supplementary materials: Correlation of metal-to-insulator transition and strain state of VO_2 films on TiO_2 (110) substrates

Hao Lu[1,3,a)], Lei Li[1], Zhiwu Tang[1], Maji Xu[1], Yonghui Zheng[2], Martin Becker[3], Yinmei Lu[1],Mingkai Li[1], Pai Li[1], Zaoli Zhang[2,a)], Peter J. Klar[3], and Yunbin He[1,a)]

[1] *Ministry-of-Education Key Laboratory of Green Preparation and Application for Functional Materials, Hubei Key Lab of Ferro & Piezoelectric Materials and Devices, Hubei Key Laboratory of Polymer Materials, and School of Materials Science & Engineering, Hubei University, Wuhan 430062, China.*

[2] *Erich Schmid Institute of Materials Science, Austrian Academy of Sciences, A-8700 Leoben, Austria*

[3] *Institute of Experimental Physics I and Center of Materials Research (ZfM/LaMa), Justus Liebig University Giessen, Giessen, Germany*

[a)] *Authors to whom correspondence should be addressed: ybhe@hubu.edu.cn, zaoli.zhang@oeaw.ac.at, and hao.lu@physik.uni-giessen.de*

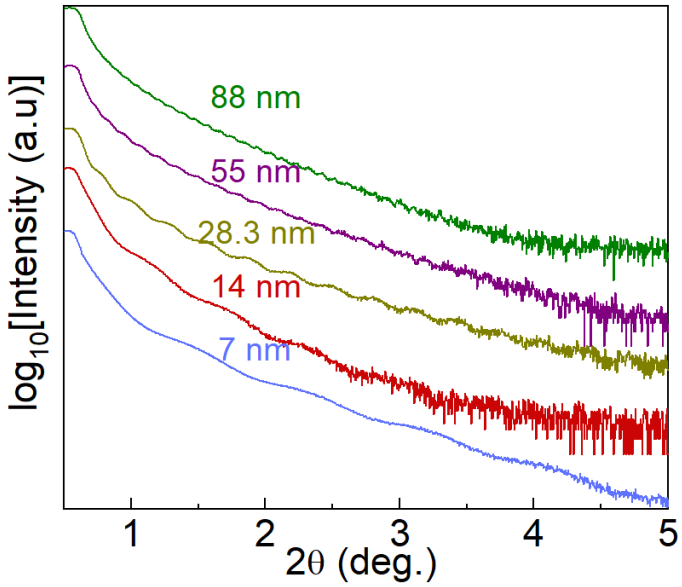

Fig. S1. XRR spectra of VO_2 films of various thicknesses.

X-ray Reflection (XRR) was used to determine the thickness of the deposited VO_2 films. Fig. S1 shows XRR curves of VO_2/TiO_2 (110) samples of different thicknesses. The Leptos software of the XRD apparatus was used for fitting the interference oscillations of the curves. Periodic oscillations of the XRR curve are only visible for samples with thicknesses below 100 nm. Therefore, XRR could only be used to determine the thickness of samples with thicknesses below 100 nm. For thicker samples, we estimated the thickness from the deposition rate (0.14 nm/pulse), which we calculated using the thickness extracted by XRR of samples below 100 nm and the corresponding number of pulses.

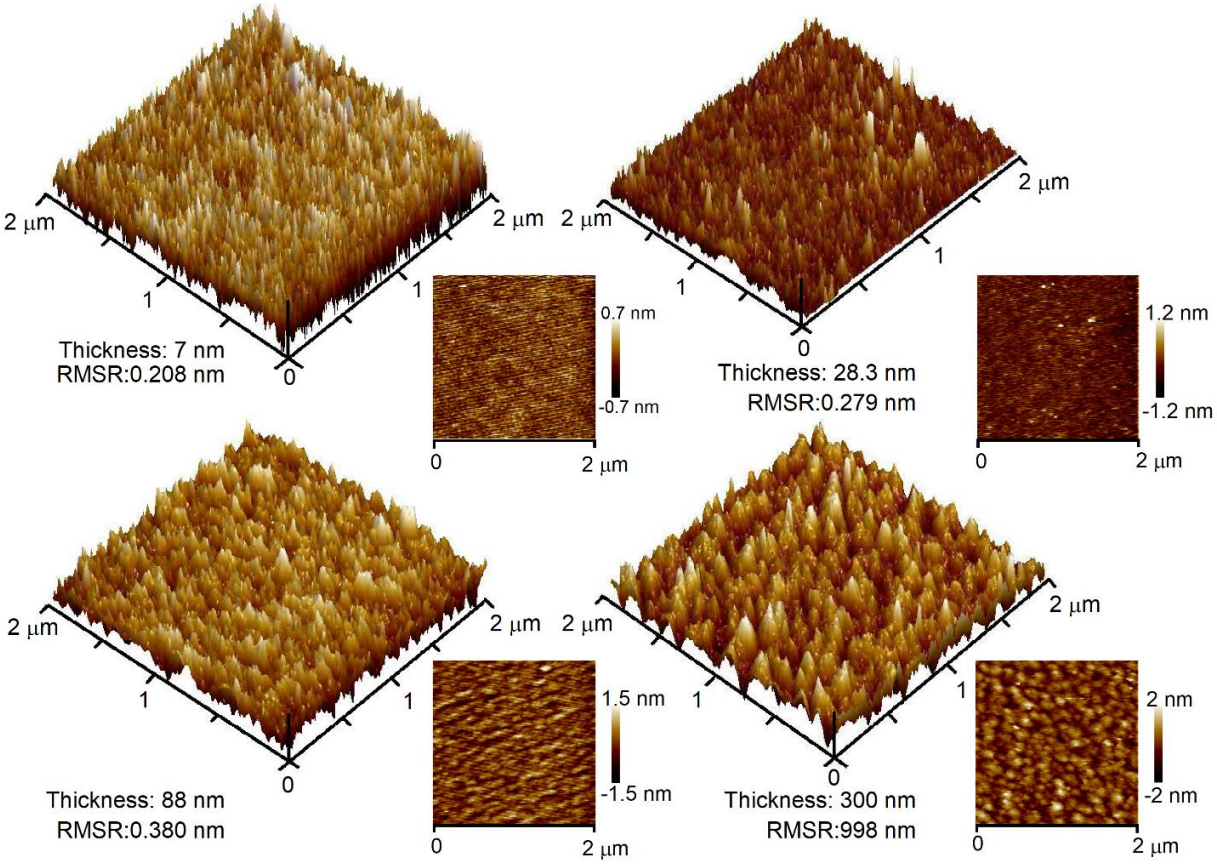

Fig. S2. AFM images of VO_2 films with different thicknesses.

The surface of the VO_2 films deposited on the rutile TiO_2 (110) substrates is dense, homogeneous, and consists of small grains. The root-mean-square (RMS) roughness of films averaged over a 2×2 μm^2 scan area is 0.2 to 0.99 nm and increases when the thickness of films increases from 7 nm to 300 nm.

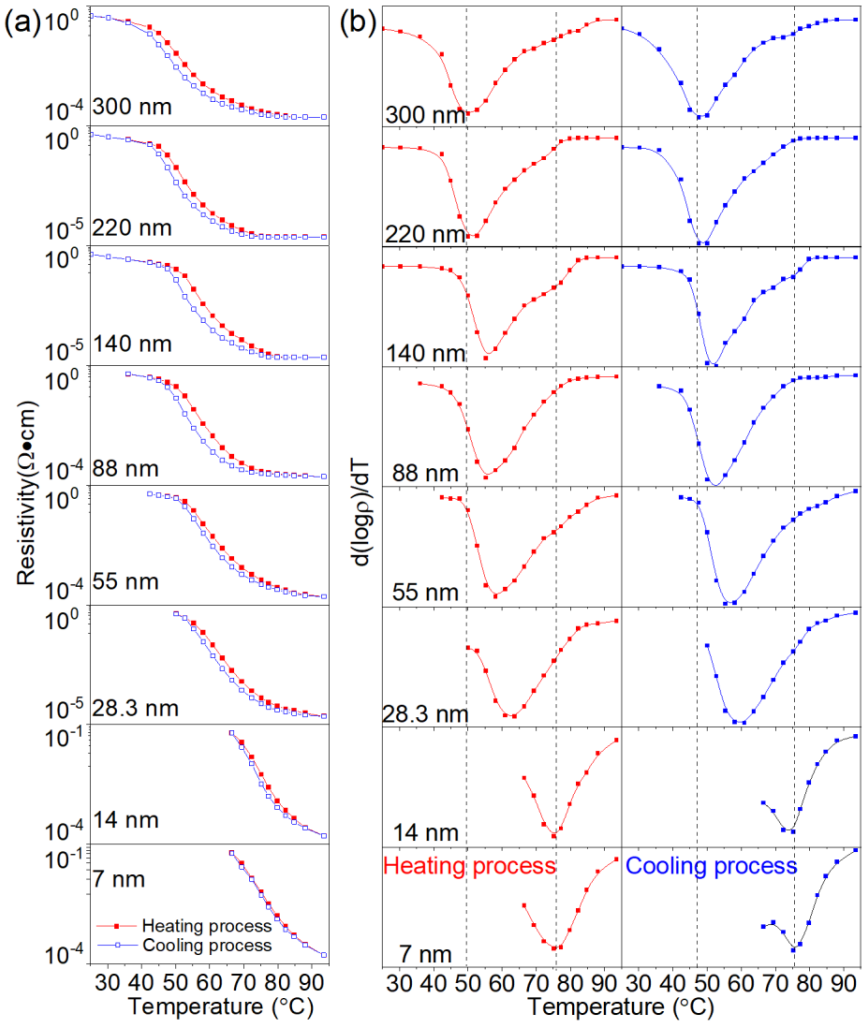

Fig. S3. (a) Temperature dependence of electrical resistivity for different-thickness VO_2 films. (b) Derivative curves (d[log(ρ)]/dT) versus temperature recorded during heating and cooling of the films shown in (a).

Fig. S3 (a) shows plots of the resistivity ρ curves of all VO_2 films on TiO_2 (110) studied. The plots are stacked for clarity. The electrical properties vary with temperature. The results obtained during heating and cooling processes differ and exhibit a hysteresis behavior. All the films show the expected MIT charater, where the resistivity changes by two to four orders of magnitude. For 7 nm and 14 nm ultrathin films, the resistivity in the insulating phase is too high to be measured at

temperatures below 65°C. (b) displays the d(log ρ)/dT vs T curves for all VO_2 films, the MIT temperature T_C corresponds to the average of temperatures where the minima occur in the d(log ρ)/dT curve measured during heating and cooling of the film. The MIT temperature decreases from 75.6 °C to 49.4 °C when increasing film thickness from 7 nm to 300 nm.

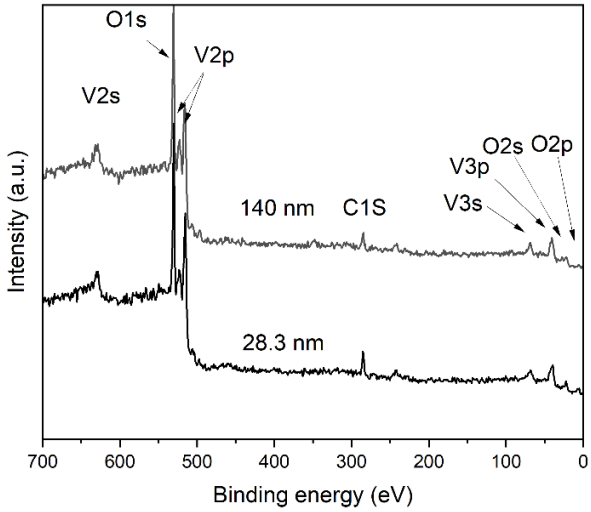

Fig. S4. XPS survery spectra of VO_2 films with thicknesses of 28.3 nm and 140 nm.

In Fig. S4, only V, O, and C signals appear in the XPS survey spectra, with C mainly originating from the XPS sample holder because sample size is smaller than the XPS signal collection area.

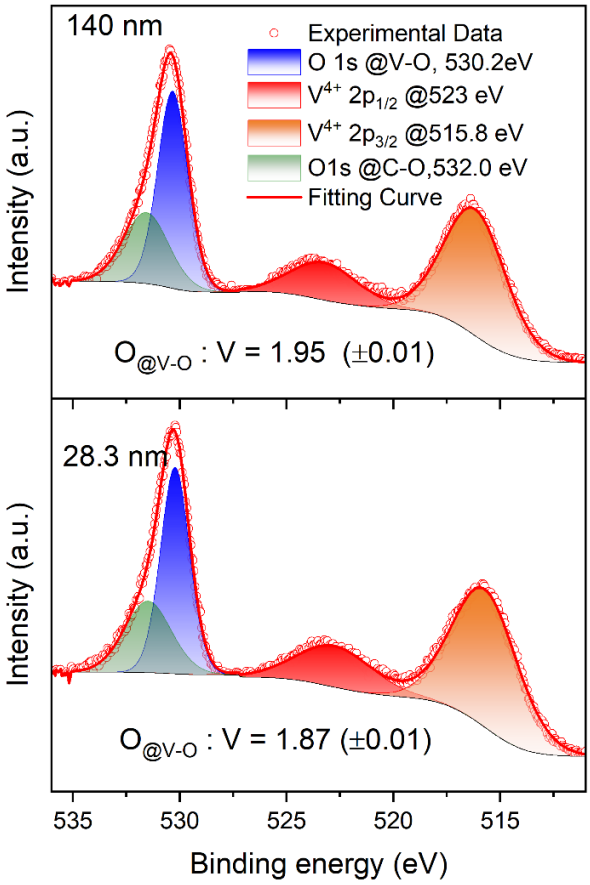

Fig. S5. Detailed XPS spectra of V 2p and O 1s for VO_2 films with thicknesses of 28.3 nm and 140 nm.

In Detailed XPS spectra, V^{4+} characteristic peaks were found at 523 eV and 515.8 eV, corresponding to V^{4+} $2p_{1/2}$ and V^{4+} $2p_{3/2}$, respectively. It indicates that the real compositions of the films are close to VO_2. However, there oxygen vacancies exist in thicker VO_2 films; as example, the O/V ratio (1.95) in the 140 nm-thick film is below 2.

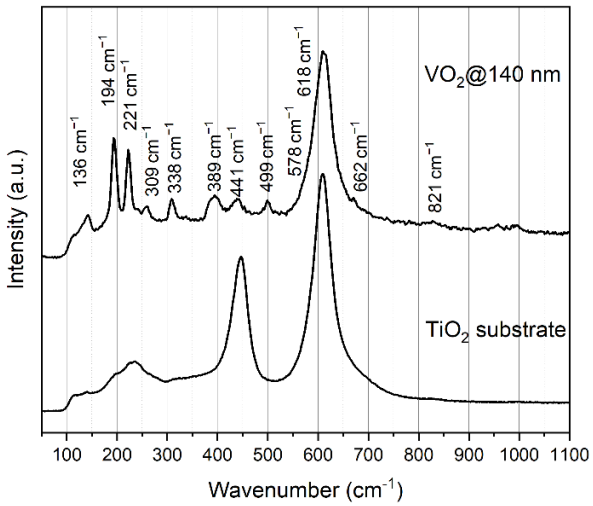

Fig. S6. Raman spectra of the 140 nm-thick VO_2 film and TiO_2 substrate.

The monoclinic VO_2 structure is associated with 18 Raman-active vibrations ($9A_g + 9B_g$). The modes at 136, 194, 221, 309, 338, 389, 499, 618, and 662 cm^{-1} are assigned to A_g phonons, whereas the modes at 136, 221, 261, 389, 441, 578, and 821 cm^{-1} are attributed to B_g symmetry (The signals corresponding to the 578 cm^{-1} mode are obscured by the dominant substrate signals in our measurement). The analyses of Raman spectra reveal that the films employed in our experiments exhibit characteristics consistent with the M1-phase of VO_2, although there exist some oxygen vacancies in the thicker films.

Table S1. FWHM, MIT temperature, RMSR, and the lattice parameters calculated from RSM measurements for VO_2 films of different thicknesses.

Film thickness (nm)	FWHM (deg.)	RMSR (nm)	MIT temperature (°C)	Lattice a_R (nm)	Lattice c_R (nm)	c_R/a_R
7	/	0.208	75.6	/	/	/
14	0.087	/	74.8	/	/	/
28	0.078	0.279	61.4	/	/	/
55	0.108	0.170	58.3	4.54225	2.86575	0.63091
88	0.198	0.380	54.4	4.54203	2.8614	0.62998
140	0.281	0.592	53.9	4.54652	2.85868	0.62876
220	0.402	0.741	50.1	4.55442	2.85501	0.62687
300	0.567	0.998	49.4	4.55512	2.84932	0.62552

4 Publication 2: $Cu_xTi_{1-x}O_2$ buffer layers in VO_2–based smart windows – a viable compromise towards large-scale industrial production

In this chapter, we investigate the use of rutile copper titanium oxide ($Cu_xTi_{1-x}O_2$) as a buffer layer for the low-temperature growth of thermochromic vanadium dioxide. Specifically, we examine how incorporating copper influences the structural and optical properties of titanium dioxide. On the one hand, its incorporation yields alloy formation and lowers the transition temperature of the anatase-to-rutile phase transition, enabling rutile $Cu_xTi_{1-x}O_2$ to be formed in the sputtering deposition process at temperatures as low as 200 °C, compared to the minimum of 600 °C required for rutile TiO_2. However, on the other hand, the optical transparency of $Cu_xTi_{1-x}O_2$ in the visible range of the electromagnetic spectrum decreases with increasing Cu content.

We design and grow a tri-layer structure consisting of a $Cu_xTi_{1-x}O_2$ buffer layer, a thermochromic VO_2 layer, and an anatase TiO_2 antireflection coating, and study its thermochromic key parameters. The performance is almost as good as that of a tri-layer structure where rutile TiO_2 is used as the buffer layer. Therefore, using a rutile $Cu_xTi_{1-x}O_2$ buffer layer allows VO_2-based multilayer structures for advanced thermochromic applications to be grown at deposition temperatures approaching those compatible with industrial sputtering apparatuses.

The $Cu_xTi_{1-x}O_2$ layers were deposited by radio-frequency sputtering on quartz substrates (Suprasil). A 4-inch ceramic TiO_2 target was used, positioned at a distance of 4 inches from the substrate. In order to alloy the TiO_2 thin films with Cu, several high-purity Cu wires were manually mounted on the surface of the target.

This target configuration allowed us to deposit $Cu_xTi_{1-x}O_2$ thin films with different Cu content x in a controlled and reproducible way by varying the number of Cu

wires. All thin films were sputtered to obtain a thickness between 100 and 200 nm. The heater temperature during deposition was set to a value in the range between 200°C to 400°C. A mixture of Ar and O_2 with a pressure of 3.4×10^{-3} mbar was used to generate the plasma. The O_2 gas flux was varied between 0 and 3 sccm at a fixed Ar flux of 31 sccm.

As reference buffer systems, anatase (A) and rutile (R) thin films were prepared by ion beam sputtering at room temperature and 560°C, respectively. VO_2 thin films used as active thermochromic layers within the tri-layer structure were prepared by RF sputtering using a 4-inch metallic vanadium target. The deposition temperature of the VO_2 films was set to 300°C. The RF plasma was again generated using a mixture of Ar and O_2 gases at a pressure of 3.4×10^{-3} mbar. The gas flux ratio was set at 1.1 sccm for O_2 and 31 sccm for Ar. All VO_2 thin films had a thickness of 40 nm.

The anatase TiO_2 layer serving as antireflection coating in case of tri-layer coatings also was deposited by ion beam sputtering at room temperature using a ceramic TiO_2 target.

The layer thicknesses and mass densities of the $Cu_xTi_{1-x}O_2$ thin films were analyzed with X-ray reflection. The film structure was analyzed with grazing-incidence X-ray diffraction (GIXRD). In this mode of XRD, the X-rays are incident on the sample at a grazing angle, meaning they skim along the surface rather than striking it directly perpendicularly. Experiments at this shallow angle possess an enhanced sensitivity to surface structures. XRD traces yielded the crystalline structure of the thin films. Both XRR and XRD were performed using a Rigaku SmartLab diffractometer, which operates with a 9 kW rotating Cu anode.

Raman spectroscopy with 515 nm laser excitation and a spectral resolution of 1.5 cm^{-1} (Renishaw inVia Raman microscope system) was used for phase identification of the $Cu_xTi_{1-x}O_2$ and VO_2 thin films, providing complementary confirmation of the findings obtained by XRD.

X-ray photoelectron spectroscopy was employed for the comprehensive analysis of both the elemental composition within the film and the valence states inherent to each individual element. A PHI VersaProbe II spectrometer with a monochromatic Al Kα (1486.6 eV) X-ray anode directed at 45° towards the surface normal was used. Charge compensation was achieved using a combination of an electron gun and an Ar^+ ion gun. The samples were exposed to a focused Ar^+ beam at an acceleration voltage of 1 kV to remove adsorbed impurities.

A Zeiss-Merlin scanning electron microscope equipped with an InLens detector was used for investigating the film morphology. Optical transmittance measurements were conducted using a PerkinElmer Lambda 900 UV–Vis–NIR spectrometer. For temperature-dependent measurements, a resistively heated sample holder,

controlled by a Eurotherm heating controller and integrated with a Peltier cooling device, was used to achieve precise heating and cooling rates. A PT100 sensor was employed to monitor the sample's actual temperature.

The optical constants, specifically the refractive index (n) and extinction coefficient (k), of rutile $Cu_xTi_{1-x}O_2$, anatase and rutile TiO_2, and VO_2 were measured at temperatures of 25°C and 90°C using an ellipsometer (SENresearch 4.0, Sentech) equipped with a custom-designed heating stage. The reference samples of rutile $Cu_xTi_{1-x}O_2$, anatase and rutile TiO_2, and VO_2 were prepared as thin films on (111)-oriented single-crystal silicon substrates. Single-crystalline silicon was chosen as the substrate material to avoid backside reflections during ellipsometry measurements.

The dispersions $n(\lambda)$ and $k(\lambda)$ of the different layer materials were then determined and used as input parameter files for the Essential MacLeod software to determine the optimal thicknesses of the buffer and antireflection layers surrounding the 40 nm thick VO_2 active layer in the tri-layer structure studied. The layer thicknesses were chosen to optimize the tri-layer structure $Cu_xTi_{1-x}O_2 \parallel VO_2 \parallel$ A-TiO_2 in terms of the thermochromic key performance parameters, i.e., the luminous transmittance (T_{lum}) and the solar modulation ability (ΔT_{sol}).

This work was published in *Solar Energy Materials and Solar Cells* **295**, 114016 (2026), titled "**$Cu_xTi_{1-x}O_2$ buffer layers in VO_2–based smart windows – a viable compromise towards large-scale industrial production**". The article was accepted on October 10, 2025. **DOI:** 10.1016/j.solmat.2025.114016

All samples in this study were fabricated and measured by Hao Lu. Jan Luka Dornseifer conducted the XPS measurements and analysis. Angelika Polity provided technical guidance on the operation of the magnetron sputtering system used in this work. This study greatly benefited from extensive scientific discussions among all authors. In particular, Martin Becker and Peter J. Klar made significant contributions to the interpretation and understanding of the results and provided valuable guidance for the subsequent experimental and theoretical developments.

Copyright Permission Statement

I hereby declare that the copyright permission from the publisher was obtained prior to reproducing the previously published article in this dissertation.

Solar Energy Materials & Solar Cells 295 (2026) 114016

Contents lists available at ScienceDirect

Solar Energy Materials and Solar Cells

journal homepage: www.elsevier.com/locate/solmat

$Cu_xTi_{1-x}O_2$ buffer layers in VO_2–based smart windows – a viable compromise towards large-scale industrial production

Hao Lu *, Martin Becker, Jan Luka Dornseifer, Angelika Polity, Peter J. Klar

Institute of Experimental Physics I and Center of Materials Research (ZfM/LaMa), Heinrich-Buff-Ring 16, 35392, Giessen, Germany

ARTICLE INFO

Keywords:
Vanadium dioxide
Rutile copper titanium oxide
Multilayer structure
Smart windows

ABSTRACT

The use of rutile copper titanium oxide ($Cu_xTi_{1-x}O_2$) as a buffer layer for the low-temperature growth of thermochromic vanadium dioxide is investigated. Specifically, this study examines how incorporating copper influences the structural and optical properties of titanium dioxide. On the one hand, its incorporation yields alloy formation and lowers the transition temperature of the anatase-to-rutile phase transition, enabling rutile $Cu_xTi_{1-x}O_2$ to be formed in the sputtering deposition process at temperatures as low as 200 °C, compared to the minimum of 600 °C required for rutile TiO_2. However, on the other hand, the optical transparency of $Cu_xTi_{1-x}O_2$ in the visible range of the electromagnetic spectrum decreases with increasing Cu content. A tri-layer structure consisting of a $Cu_xTi_{1-x}O_2$ buffer layer, a thermochromic VO_2 layer, and an anatase TiO_2 antireflection coating is designed and grown, and its thermochromic key parameters are studied. The performance is almost as good as that of a tri-layer structure where rutile TiO_2 is used as the buffer layer. Therefore, using a rutile $Cu_xTi_{1-x}O_2$ buffer layer allows VO_2-based multilayer structures for advanced thermochromic applications to be grown at deposition temperatures approaching those compatible with industrial sputtering apparatuses.

1. Introduction

The growing demand for energy-efficient building technologies has prompted research into dynamic window coatings that can regulate both incoming and outgoing transmission of solar heat and visible light [1,2]. Here, different coatings can be applied, dependent on area of application and of spectral range to be modulated. Among these, vanadium dioxide (VO_2) and VO_2-based thin-film coatings have attracted considerable attention [3–8]. Bulk VO_2 exhibits a reversible phase transition at around 68 °C, changing from a low-temperature monoclinic phase to a high-temperature rutile phase. This transition is accompanied by an insulator-to-metal transition, which causes dramatic changes in optical and electrical properties [1,2,9–11]. The ability to tune the phase transition temperature (T_c) and the optical properties in various ways (e.g. intrinsic [12,13] and extrinsic doping [4,14–18] or strain [10,19–21]) makes VO_2-based thin-film coatings prime candidates as active materials for smart window applications. Embedding the thermochromic layers in multilayer structures provides further opportunities to adjust the optical properties, i.e. transmittance in the visible spectrum and switching efficiency in the infrared range [5,17,22]. Researchers have now demonstrated that the performance of VO_2-based thermochromic multilayer structures meets the industry's requirements for their use as large-scale, energy-saving coatings in smart windows [23–27].

Taking the fabrication process of this thermochromic technology from the laboratory to a commercially viable smart window fabrication requires careful analysis of the process parameters for depositing multilayer structures, considering both scalability to window-pane sizes and compatibility with industrial deposition processes [2,6,24,28]. Industrial thin-film deposition processes necessitate a balance between the performance of the multilayer coating and fabrication costs [27,29]. Cost efficiency increases competitiveness in the market and determines the product's economic profitability. In addition, in processes with complex workflows, profitability is strongly influenced by throughput and reject rate [30]. More broadly, costs are determined by the availability of the chemical elements used, the energy efficiency and speed of the growth process, and its environmental friendliness. Put simply, lower growth temperatures and small variations in the deposition temperatures of the different layers of the multilayer coating result in lower energy consumption during the deposition process, enabling faster production times and a higher throughput rate [31]. This reduces operating costs. Production becomes more efficient and economical, particularly in the case of large-scale production [6]. Reduced energy

* Corresponding author.
E-mail address: Hao.lu@physik.uni-giessen.de (H. Lu).

https://doi.org/10.1016/j.solmat.2025.114016
Received 27 June 2025; Received in revised form 9 October 2025; Accepted 10 October 2025
Available online 18 October 2025

demand can be directly translated into lower CO_2 emissions and a smaller ecological footprint for the production process and product. Especially, this holds true in countries and regions where the energy supply is predominantly based on non-renewable sources. These considerations motivate our effort to minimize the growth temperature of each film layer.

Optimization of the industrial process for depositing thermochromic energy-saving multilayer coatings on float glass faces a major challenge. It is manifested by the typically high deposition temperatures ($\geq$400 °C) of VO_2-based materials. These deposition temperatures are too high and incompatible with the commonly used float glass window panes [32]. To address this challenge, buffer layers have been explored to lower the VO_2 formation temperature and improve its integration with various substrates [33]. In many VO_2-based multilayer structures used to successfully demonstrate that such multilayers can indeed fulfill the key performance parameters set by industry, rutile TiO_2 has been employed as buffer layer for the VO_2-based active layers [34]. Thus, it is among the candidate materials. However, TiO_2 with rutile structure itself requires rather high deposition temperatures, typically above 600 °C [35].

In this study, an alternative to rutile TiO_2 as a buffer layer in VO_2-based multilayer structures is sought to address the challenges posed by high growth temperatures and significant variations in the growth temperature profile. Generally, a polycrystalline buffer layer with grains of the same rutile structure as the VO_2 high-temperature phase supports polycrystalline VO_2 growth and enables high-quality VO_2 or VO_2-based films to be obtained at considerably lower temperatures [36]. In this regard, the $Cu_xTi_{1-x}O_2$ alloy is a possible replacement. In the first part of the paper, it is demonstrated that rutile $Cu_xTi_{1-x}O_2$ layers can be produced by sputter deposition at growth temperatures between 200 °C and 400 °C, unlike rutile TiO_2, which requires temperatures of at least 600 °C. This is because Cu doping in TiO_2 decreases the phase transition temperature of the anatase-to-rutile transition compared to pristine TiO_2 [33,37].

In the second part, it is demonstrated that VO_2 layers of good crystalline quality can be grown on rutile $Cu_xTi_{1-x}O_2$ buffer layers at considerably reduced deposition temperatures. To this end, an optimized tri-layer thin-film system was designed and grown, consisting of a VO_2 as the functional active layer embedded between a $Cu_xTi_{1-x}O_2$ buffer layer and an anatase TiO_2 antireflection coating. The tri-layer structure with optimal layer thicknesses was characterized. Its thermochromic key parameters realized were compared with those of a set of corresponding tri-layer samples where other buffer layers were employed. The agreement is found to be satisfactory. The results obtained suggest an approach to adjusting the growth temperature profile of the multilayer deposition process that could render the corresponding large-scale deposition process economically viable.

2. Experimental details

The $Cu_xTi_{1-x}O_2$ layers were deposited by radio-frequency (RF) sputtering on quartz substrates (Suprasil). A 4-inch target of ceramic TiO_2 was used and positioned at a distance of 4 inches from the substrate. To incorporate Cu into TiO_2 during thin-film growth, high-purity copper wires were symmetrically mounted on the target surface with the crossing point at the geometric center of the target. Using this approach, however, the exact position of the substrate relative to the geometric center of the wire distribution will influence the overall Cu content in the thin film and its lateral distribution. The substrate was placed on the sample holder directly facing the geometric center of the target to reduce this effect. Naturally, the Cu distribution of this target is less uniform than that of commercial Cu-doped TiO_2 targets. However, the doping level can be controlled by adjusting the number of copper wires without the need to exchange targets with different doping levels, thereby significantly reducing the experimental costs in the present study. Furthermore, potential preferential sputtering effects and, thus, changes in Ti:Cu ratio in the target itself, are avoided. In this work, when keeping the number and arrangement of the Cu wires, the substrate position, and the deposition parameters — including sputtering power, deposition temperature, and gas flow rates — constant, $Cu_xTi_{1-x}O_2$ films were obtained with a Cu content variation below 2 % between deposition runs. Furthermore, the difference in Cu content between the center and the edge of the substrate is less than 1 %. All thin films were sputtered to obtain a thickness between 100 and 200 nm. The heater temperature during deposition was set to a value in the range between 200 °C and 400 °C. A mixture of Ar and O_2 with a pressure of 3.4×10^{-3} mbar was used to generate plasma. The O_2 gas flux was varied between 0 and 3 sccm at a fixed Ar flux of 31 sccm. As reference buffer systems, anatase (A) and rutile (R) thin films were prepared by ion beam sputtering at room temperature and 560 °C, respectively. VO_2 thin films used as active thermochromic layers within the tri-layer structure were prepared by RF sputtering using a 4-inch metallic vanadium target. The deposition temperature of the VO_2 films was set to 300 °C. The RF plasma was again generated using a mixture of Ar and O_2 gases at a pressure of 3.4×10^{-3} mbar. The gas flux ratio was set at 1.1 sccm for O_2 and 31 sccm for Ar. All VO_2 thin films had a thickness of 40 ± 2 nm. The anatase TiO_2 layer serving as antireflection coating in case of tri-layer coatings also was deposited by ion beam sputtering at room temperature using a ceramic TiO_2 target.

The layer thicknesses and mass densities of the $Cu_xTi_{1-x}O_2$ thin films were analyzed with X-ray reflectivity (XRR). The film structure was analyzed with grazing-incidence X-ray diffraction (GIXRD). In this mode of XRD, the X-rays are incident on the sample at a grazing angle, meaning they skim along the surface rather than striking it directly perpendicularly. Experiments at this shallow angle possess an enhanced sensitivity to surface structures. XRD traces yielded the crystalline structure of the thin films. Both XRR and XRD were performed using a *Rigaku SmartLab* diffractometer which operates with a 9 kW rotating Cu anode. Raman spectroscopy with 515 nm laser excitation and a spectral resolution of 1.5 cm^{-1} (*Renishaw inVia* Raman microscope system) was used for phase identification of the $Cu_xTi_{1-x}O_2$ and VO_2 thin films, providing complementary confirmation of the findings obtained by XRD.

X-ray photoelectron spectroscopy (XPS) was employed for the comprehensive analysis of both the elemental composition within the film and the valence states inherent to each individual element. A *PHI VersaProbe II* spectrometer with a monochromatic Al K_α (1486.6 eV) X-ray anode directed at 45° towards the surface normal was used. Charge compensation was achieved using a combination of an electron gun and an Ar^+ ion gun. The samples were exposed to a focused Ar^+ beam at an acceleration voltage of 1 kV to remove adsorbed impurities.

A *Zeiss-Merlin* scanning electron microscope (SEM) equipped with an *InLens* detector was used for investigating the film morphology. Optical transmittance measurements were conducted using a *PerkinElmer Lambda 900* UV–Vis–NIR spectrometer. For temperature-dependent measurements, a resistively heated sample holder, controlled by a *Eurotherm* heating controller and integrated with a Peltier cooling device, was used to achieve precise heating and cooling rates. A PT100 sensor was employed to monitor the sample's actual temperature.

The optical constants, specifically the refractive index (n) and extinction coefficient (k), of rutile $Cu_xTi_{1-x}O_2$, anatase TiO_2 and VO_2 are measured at temperatures of 25 °C and 90 °C using an ellipsometer (*SENresearch 4.0*, Sentech) equipped with a custom-designed heating stage. The reference samples of rutile $Cu_xTi_{1-x}O_2$, anatase TiO_2, and VO_2 were prepared as thin films on (111)-oriented single-crystal silicon substrates. Single-crystalline silicon was chosen as substrate material to avoid backside reflections during ellipsometry measurements. The dispersions (n,k) of the different layer materials are then determined and used as input parameter files of the *Essential Macleod* software for determining the optimal thicknesses of buffer layer and antireflection layer surrounding the 40 nm thick VO_2 active layer of the tri-layer structure studied. The layer thicknesses are chosen to optimize the tri-layer structure $Cu_xTi_{1-x}O_2||VO_2||A\text{-}TiO_2$ in terms of the

thermochromic key performance parameters, i.e. the luminous transmittance (T_{lum}) and the solar modulation ability (ΔT_{sol}).

3. Results and discussion

Both parameters, oxygen flux and Cu content, are expected to affect the stoichiometry and the crystalline structure of a sputter deposited $Cu_xTi_{1-x}O_2$ thin film as will be discussed below. In the growth regime under investigation, the deposited $Cu_xTi_{1-x}O_2$ thin films are polycrystalline and the crystal structure of the grains is either anatase or rutile. The quantity Q_R is introduced to denote the volume fraction of rutile grains within the deposited thin film. The results shown in Fig. 1 are obtained on thin films deposited at a growth temperature of 400 °C. Thin films were grown at different oxygen and Cu contents by varying the O_2 fraction in the process gas and the number of Cu wires mounted on top of the ceramic TiO_2 target. It should be noted that similar results have been obtained on a series of samples grown at temperatures of 200 °C and 300 °C. Nevertheless, the focus in what follows will be on the samples grown at 400 °C to avoid complications in the growth of the active VO_2 layer. It is well established that VO_2 thin films require a minimum substrate surface temperature of approximately 400 °C when deposited directly on quartz glass substrates [38–40]. Therefore, deposition on a rutile buffer layer at this temperature must be possible without major adjustments of the growth parameters which may be difficult because of the narrow growth window for VO_2 [41]. Ideally, the buffer layer should yield further reduction of the growth temperature of polycrystalline VO_2. The main emphasis of the work presented is on finding an alternative for a rutile TiO_2 buffer layer which itself requires much higher growth temperatures of about 600 °C.

The Cu content of all deposited films was determined using XPS by thorough analysis of Cu and Ti 2*p* core levels (see discussion of in Fig. S1 and Fig. S2 in the supplementary information for more details). The analysis of the Cu 2*p* core levels also reveals the coexistence of monovalent and divalent states of Cu in all thin films studied. As expected, the ratio of Cu^+ to Cu^{2+} ions in the films gradually increases towards higher Cu doping concentration. Some authors propose that Cu^+ ions assume a critical role in the structural phase transition from anatase to rutile within TiO_2 [35]. The ionic radii of Cu^{2+} and Cu^+ are 0.073 nm and 0.077 nm, respectively, slightly larger than the ionic radius of Ti^{4+} (0.0605 nm). Cu^{2+} and Cu^+ ions likely substitute Ti^{4+} ions in the TiO_2 lattice without inducing the formation of a secondary phase. The substitution of Cu^{2+} and Cu^+ ions induces lattice distortion and generates oxygen vacancies, weakening Ti–O bonds and facilitating the nucleation and growth of the rutile phase [37]. Specifically, 1 mol% Cu^{2+} induces 1 mol% oxygen vacancies, while 1 mol% Cu^+ induces 1.5 mol% oxygen vacancies.

Obviously, a variation of the supply of oxygen in the growth process will also affect the stoichiometry of the deposited $Cu_xTi_{1-x}O_2$ thin film. Deviating from the ideal setting and reducing the oxygen flux generates additional oxygen vacancies (see Fig. S3 in the supplementary information). Thus, the formation of oxygen vacancies in the sputter process itself is expected to also affect the anatase-to-rutile phase transition.

Fig. 1(a) exemplarily shows the X-ray diffraction patterns of $Cu_xTi_{1-x}O_2$ thin films grown with 3 sccm oxygen flux. The XRD pattern obtained from the pure TiO_2 film mainly exhibits the characteristic diffraction peaks of a polycrystalline anatase structure. The diffraction peaks at 25.281°, 37.8°, 48.049°, 55.06°, 62.688°, 68.76° and 75.029° can be assigned to reflections (101), (004), (200), (211), (204), (116), and (215) (PDF#21–1272). The diffraction peaks at 27.446°, 36.085°, 41.225°, 56.64°, 64.038° and 69.008°, can be assigned to the rutile TiO_2 (110), (101), (111), (220), (310) and (301) planes (PDF#21–1276). With increasing Cu doping content of the films, a gradual structural transformation was observed from a predominantly anatase phase with minor rutile inclusions to a predominantly rutile phase with minor anatase inclusions, eventually resulting at sufficiently high Cu content in an almost perfect rutile phase. Already upon the incorporation of 12.6 % Cu into the crystalline lattice of TiO_2, rutile features become clearly visible in the corresponding XRD trace. With increased concentration of Cu, the XRD peaks of the rutile phase become more prominent, whereas the intensity of diffraction peaks attributed to the anatase phase diminishes. Finally, upon 23.5 % Cu content within the film, the almost complete transition into a rutile structure has occurred. The XRD results are fully corroborated by the trends observed in Raman spectra of the sample series (see Fig. S4 in the supplementary information). The Q_R

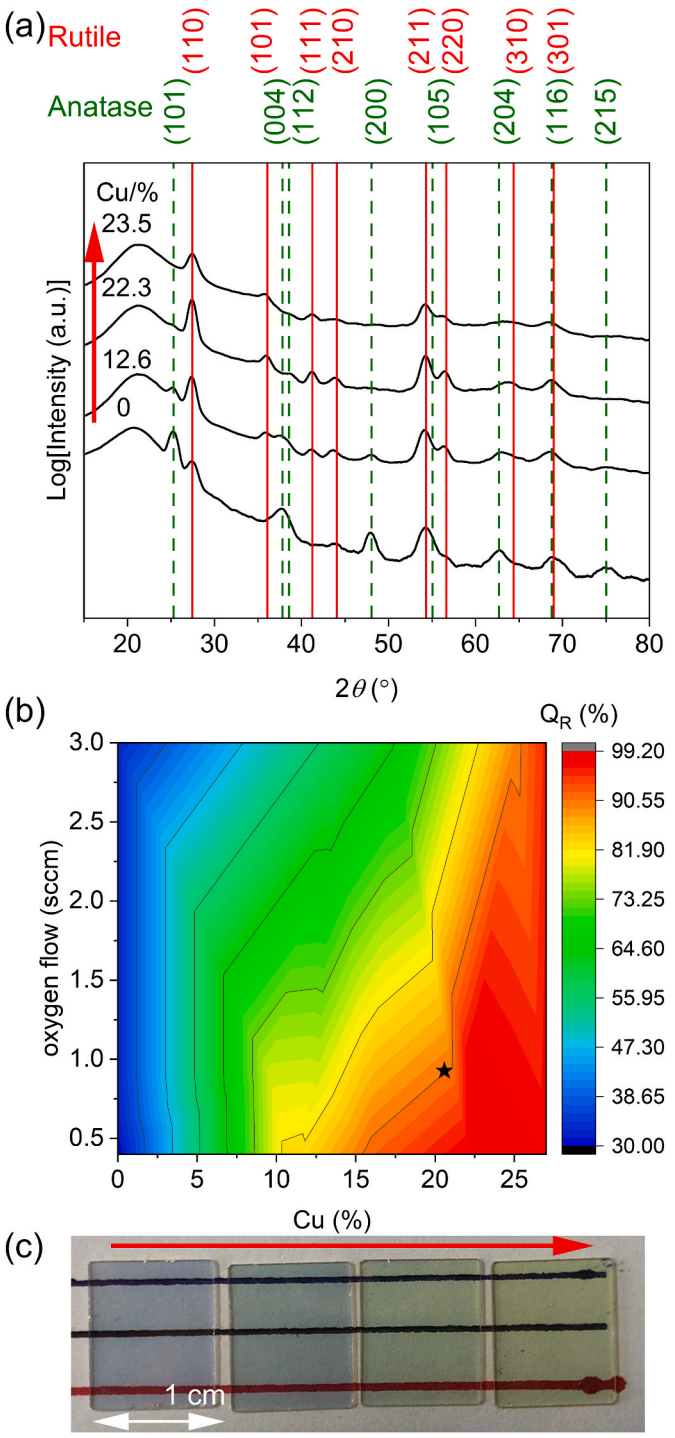

Fig. 1. (a) XRD diffraction patterns of $Cu_xTi_{1-x}O_2$ thin films of various Cu contents x. With increasing Cu content an anatase-to-rutile structural phase transition can be observed. (b) Rutile fraction Q_R as function of Cu content in the layer and oxygen flux applied during deposition. (c) Optical impression of the $Cu_xTi_{1-x}O_2$ thin films on quartz glass.

value can be obtained from the areas of the diffraction peaks of the rutile and anatase phases in the XRD traces. It is given by the ratio of the total area of the rutile peaks to the sum of the total areas of both anatase and rutile diffraction peaks.

The growth phase diagram for $Cu_xTi_{1-x}O_2$ thin films in Fig. 1(b) is a plot of the rutile volume fraction Q_R in dependence on the oxygen flow rate (parameter directly affecting oxygen vacancy incorporation) and the Cu content (as another means of generating oxygen vacancies or introducing strain). It clearly illustrates the anticipation that oxygen and copper incorporation into TiO_2 affect - though not independently – the anatase-to-rutile phase transition. If the Cu content is already sufficiently high, additional oxygen vacancies introduced by reduced oxygen supply to the sputter plasma will not change Q_R significantly, as the $Cu_xTi_{1-x}O_2$ layer is already completely in the rutile phase. However, this does not hold, if less Cu is introduced in the sputtering process. In this case, additional oxygen vacancies are needed to promote the phase transition towards the rutile structure. Exemplarily, at a Cu content of approximately 17 %, achieving the same Q_R as obtained with 22 % Cu at an oxygen flux of 3 sccm requires lowering the oxygen flux during sputtering to 1.5 sccm. The commonality between these two cases lies in the fact that both are ultimately governed by the interplay of lattice distortion induced by Cu^+/Cu^{2+} substitution for Ti^{4+}, the formation of additional oxygen vacancies, and the weakening of Ti-O bonds. The interplay of these tuning knobs yields the same QR for different deposition parameters. In the former case, reducing the oxygen flux enhances the relative fraction of Cu^+ among the incorporated Cu ions, thereby generating additional oxygen vacancies beyond the intrinsic ones in TiO_2 and facilitating the nucleation and growth of the rutile phase. In the latter case, a higher substitution ratio of Cu ions for Ti achieves a comparable effect. These observations demonstrate that there exist multiple pathways to tune Q_R of Cu-doped TiO_2 thin films. Within a certain range, one may either employ a higher Cu content or a lower oxygen flux as the primary control parameter. This offers great flexibility and potential for practical applications. The established growth phase diagram is the basis for preparing films with specific Q_R values.

Another aspect that needs to be considered when wanting to employ rutile $Cu_xTi_{1-x}O_2$ thin films as buffer layers in VO_2-based multilayer structures for thermochromic glazing is the optical transmittance of the thin film and its color impression. A good qualitative impression is given by the photograph of four about 150 nm thick $Cu_xTi_{1-x}O_2$ thin films on quartz substrates depicted in Fig. 1(c). The Cu content x increases from left to right in the series of samples shown ranging from about 0 % to 23.5 %. The color changes from a neutral blueish gray to a blue with a greenish tint within the series. This means that this type of buffer layer and its thickness will have an impact on the color impression and the optical transmittance in the visible spectral range (characterized by the key parameter luminous transmittance T_{lum}) of the resulting thermochromic glazing.

A more quantitative assessment of the impact of the (n,k) dispersions of the materials employed in a layer stack on the thermochromic key parameters can be obtained by a systematic study of these parameters, in particular T_{lum} and ΔT_{sol}, as a function of the thicknesses of the layers [5]. Such assessments have been performed in previous work of some of the authors where also the materials' dispersion (n,k) were determined, e.g., for anatase and rutile TiO_2 or VO_2 [5,34]. Therefore, only the spectroscopic ellipsometry data corresponding to the reference samples of the four $Cu_xTi_{1-x}O_2$ thin films shown in Fig. 1(c) are given in the supplementary information (in Fig. S5(a)). The band gaps determined, in addition to the (n,k) dispersions, confirm that Cu doping yields a non-linear reduction in the optical band gap of the $Cu_{1-x}Ti_xO_2$ films with Cu content x (cf. Fig. S5(b) in the supplementary information) from about 3.2 eV to 2.3 eV in accordance with the color impressions in Fig. 1 (c). This means that in choosing the best Cu-content for a $Cu_xTi_{1-x}O_2$ buffer layer of a VO_2-based layer system, one has to compromise in terms of high Q_R (i.e., promoting VO_2 crystallinity) and large band gap (corresponding to high optical transparency). The best choice is a $Cu_xTi_{1-x}O_2$ buffer layer with $x = 21$ %, it should have a Q_R close to 1 (see asterix in Fig. 1(b)) and a band gap of still about 2.85 eV.

As a model system, a tri-layer system was employed, consisting of an almost rutile $Cu_{0.21}Ti_{0.79}O_2$ buffer layer of 40 nm thickness, an active VO_2 layer with a thickness of 40 nm and a 170 nm thick anatase TiO_2 antireflection coating. The thermochromic properties (described by T_{lum} and ΔT_{sol}) of the tri-layer system can be modelled based on the dispersions (n,k) of the materials involved using the *Essential Macleod* software (see dispersions of the constituent materials in Fig. S6 in the supplementary information). The model can be further improved by accounting for interface roughness between the layers. An estimate of the surface roughness can be obtained from atomic force microscopic measurements as well as SEM images of the surfaces of the thin films [5]. Again, such measurements for rutile TiO_2 and VO_2 layers were performed in previous work of the authors [17,34]. As shown in Fig. 3(b), SEM images of $Cu_xTi_{1-x}O_2$ thin films with different Cu contents x (see all in Fig. S7 of the supplementary information) that $Cu_xTi_{1-x}O_2$ thin films have a different surface morphology than binary TiO_2 or VO_2 thin films. The surface of the latter consists of small grains with a defined and homogeneous spatial distribution with RMS roughnesses of about 5 nm [17]. Upon Cu doping, however, small grains at the surface coalesce into larger particles of spherical shape, each consisting of a conglomerate of numerous smaller grains. The spherical particles possess a diameter of 20–30 nm. This morphology does not change upon further addition of Cu in the range investigated in this work. Thus, the surface morphology of specimens exhibiting a mixed phase comprising rutile and anatase closely resembles that of full rutile phase specimens. The RMS roughness of those layers is 8 nm. Based on these input parameters, simulations of thermoelectric key parameters of the $Cu_{0.21}Ti_{0.79}O_2||VO_2||$A-$TiO_2$ tri-layer system were performed by systematically varying the thicknesses of the buffer and AR layer (denoted as d_{buffer} and d_{AR}, respectively, both ranging from 0 to 300 nm) for a constant thickness of VO_2 of 40 nm. Further details of the calculation procedure can be found in Becker et al. [5].

The simulation results are presented in Fig. 2 as 2D plots: (a) $T_{lum}(d_{buffer}, d_{AR})$ at 25 °C and (b) $\Delta T_{sol}(d_{buffer}, d_{AR})$. Starting point is the discussion of the behavior of the luminous transmittance T_{lum} in Fig. 2 (a). The corresponding 2D plot $T_{lum}(d_{buffer}, d_{AR})$ shows maxima and minima as the buffer and AR layer thicknesses are varied. Selecting a thickness pair (d_{buffer}, d_{AR}) in the range of the first-order interference maximum of T_{lum} usually offers two advantages. First, this maximum generally represents the highest luminous transmittance value achievable, and second, it exhibits a plateau in the (d_{buffer}, d_{AR})-space, making it more robust concerning deviations in deposition time or deposition rate. However, utilizing a corresponding thickness pair ($d'_{buffer} \approx 40$ nm, $d'_{AR} \approx 170$ nm) significantly reduces the solar modulation ability, *cf.* Fig. 2(b). In other words, the first-order interference maximum of T_{lum} roughly coincides with the overall minimum of ΔT_{sol}. Improvement is typically observed when considering the second-order interference maximum of T_{lum} at ($d''_{buffer} \approx 150$ nm, $d''_{AR} \approx 170$ nm). In this case, the maximum of $T_{lum}(d''_{buffer}, d''_{AR})$ overlaps with a region indicating higher $\Delta T_{sol}(d''_{buffer}, d''_{AR})$. Thus, choosing the thickness pair (d''_{buffer}, d''_{AR}) corresponding to the second-order interference maximum of T_{lum}, is usually more promising than the first-order maximum, as the former yields a significantly higher ΔT_{sol} while only slightly reducing T_{lum}. Becker et al. observed similar dependencies in their study of AlN||VO_2||AlN tri-layer coatings [5]. However, in case of a $Cu_xTi_{1-x}O_2$, a buffer layer, a thickness d''_{buffer} of approximately 150–160 nm will lower the optical transmittance in the visible range of the electromagnetic spectrum too much. Hence, we decided to define a thermochromic tri-layer test structure based on a 40 nm thick $Cu_xTi_{1-x}O_2$ buffer layer, a 40 nm thick VO_2 layer as the functional layer, and a 170 nm thick anatase TiO_2 antireflection layer. The chosen thickness pair (d_{buffer}, d_{AR}) is indicated by an asterisk in both 2D-plots of Fig. 2.

To validate the suitability of $Cu_xTi_{1-x}O_2$ as buffer layer, the $Cu_{0.21}Ti_{0.79}O_2||VO_2||$A-$TiO_2$ tri-layer test system was deposited with the

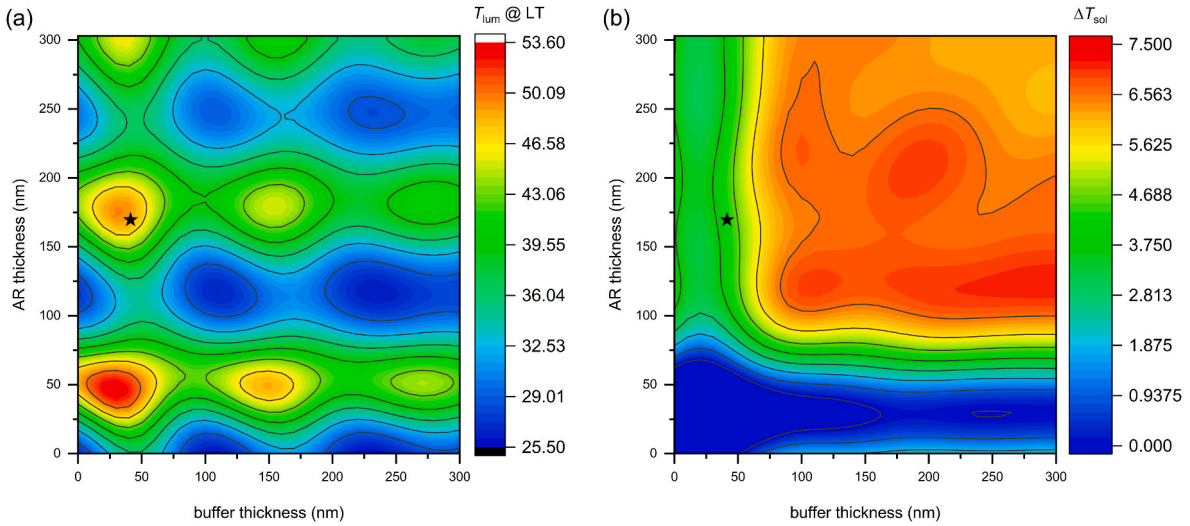

Fig. 2. Thermochromic key parameters (a)T_{lum} and (b)ΔT_{sol} as a function of the buffer layer thickness d_{buffer} and the thickness of an antireflection (AR) coating d_{AR}. A thermochromic tri-layer test structure based on 40 nm $Cu_xTi_{1-x}O_2$ as the buffer layer, 40 nm of VO_2 as the functional layer, and a suitable thickness of anatase TiO_2 as the antireflection layer(see asterisk) was selected for detailed investigation.

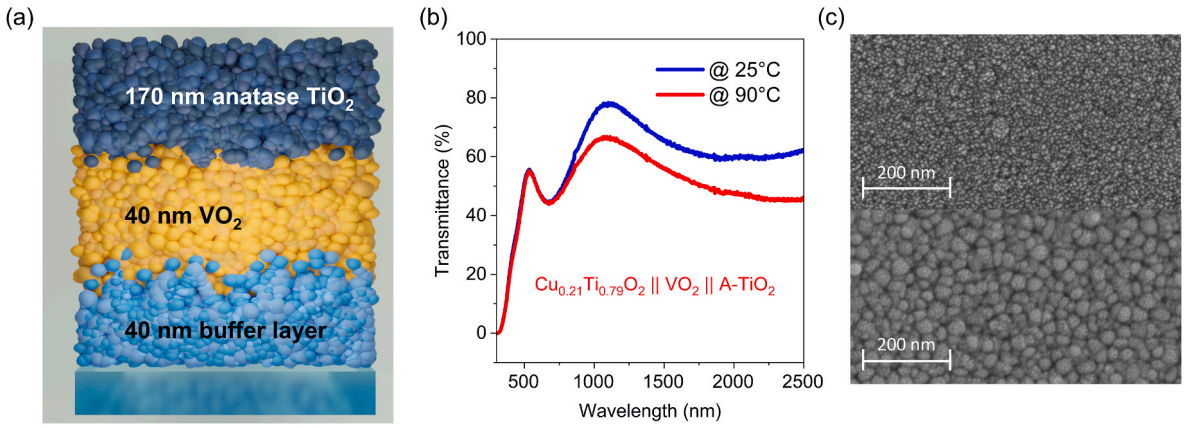

Fig. 3. (a) Schematic illustration of the tri-layer architecture $Cu_{0.21}Ti_{0.79}O_2$ ||VO_2||A-TiO_2 with fixed VO_2 thickness of 40 ± 2 nm. (b) Transmittance spectra obtained at room temperature and 90 °C for $Cu_{0.21}Ti_{0.79}O_2$ ||VO_2 ||A-TiO_2 with thicknesses of 40 ± 2 nm, 40 ± 2 nm and 170 ± 5 nm, respectively. (c) SEM images of unintentionally doped TiO_2 (top) and $Cu_{0.21}Ti_{0.79}O_2$ (bottom). The particles on the surface of pure TiO_2 exhibit approximately 10 nm sized grains, whereas the Cu-doped sample shows grains ranging from 20 to 30 nm.

optimized layer thicknesses. In addition, a set of three tri-layer reference samples was grown where other materials were employed as buffer layer, but the buffer thickness was not altered. A schematic of the tri-layer structure is shown in Fig. 3(a). The four 40 ± 2 nm thick buffer layers are: anatase TiO_2 (denoted as A-TiO_2) obtained by ion-beam sputtering at room temperature; as-grown TiO_2 (contains residual Cu and, thus, exhibits $Q_R \approx 30$ %, denoted as TiO_2) obtained by RF sputtering at 400 °C; $Cu_{0.21}Ti_{0.79}O_2$ deposited by RF sputtering at 400 °C (exhibits $Q_R \approx 81$ %); and rutile TiO_2 (denoted as R-TiO_2) obtained by ion beam sputtering at 560 °C. All VO_2 layers were grown by RF sputtering at 300 °C, all antireflection layers of A-TiO_2 by ion-beam sputtering at room temperature. The buffer materials used in the three reference tri-layer structures are amorphous TiO_2 (TiO_2), anatase TiO_2 (A-TiO_2), and rutile TiO_2 (R-TiO_2).

Optical transmittance measurements of all four tri-layer structures were conducted at 25 °C and at 90 °C. A distinct optical transmittance gap is observed, as exemplified by the temperature-dependent transmittance spectra of $Cu_{0.21}Ti_{0.79}O_2$ thin film shown in Fig. 3(b). On the basis of the recorded spectra, one can calculate the integrated luminous transmittance (T_{lum}, 380–780 nm), the integrated solar energy transmittance (T_{sol}, 300–2500 nm) and the infrared transmittance (T_{IR}, 780–2500 nm) using the expressions

$$T_{lum} = \int_{380}^{780} j(\lambda)E\lambda \cdot T(\lambda)d(\lambda) \Big/ \int_{380}^{780} j(\lambda)E\lambda \cdot d(\lambda),$$

$$T_{sol} = \int_{300}^{2500} E\lambda \cdot T(\lambda) \cdot d(\lambda) \Big/ \int_{300}^{2500} E\lambda \cdot d(\lambda) \text{ and}$$

$$T_{IR} = \int_{780}^{2500} E\lambda \cdot T(\lambda) \cdot d(\lambda) \Big/ \int_{780}^{2500} E\lambda \cdot d(\lambda),$$

where T is the recorded film transmittance, $\varphi(\lambda)$ is the standard luminous efficiency function for the photopic vision of human eyes and $E\lambda$ is the solar spectral irradiance. The key parameters of our samples were calculated as a function of a simulated solar irradiance spectrum for air mass 1.5. The modulation of luminous transmittance (ΔT_{lum}) and that of infrared transmittance (ΔT_{IR}) reflecting the switching of the optical properties due to the structural phase transition was derived as $\Delta T_{lum} = T_{lum,25\ °C} - T_{lum,90\ °C}$, $\Delta T_{sol} = T_{sol,25\ °C} - T_{sol,90°C}$ and $\Delta T_{IR} = T_{IR,25\ °C}$

-$T_{IR,90\ °C}$, respectively. The results are summarized in tabular form as Table 1.

It turns out that A-TiO_2||VO_2||A-TiO_2 tri-layer does not show a modulation of infrared light, i.e. $\Delta T_{IR} = 0$. The reason is that the vanadium oxide phase deposited on the anatase buffer was V_3O_7 instead of VO_2 (see Fig. S8 of the supplement information). It seems that excess oxygen from the buffer grown at room temperature diffuses during the growth of the vanadium oxide at 300 °C into the layer and alters the stoichiometry. All the other three tri-layer samples exhibit the switching of the IR-Transmittance with increasing temperature. In all three cases, the Raman analysis confirms that vanadium oxide layers deposited on the buffer layers are indeed VO_2. The R-TiO_2||VO_2||A-TiO_2 tri-layer structure with the buffer grown at 560 °C shows, as expected, the best IR performance ($\Delta T_{IR} \approx 10$ %). Second best ($\Delta T_{IR} \approx 9$ %) is that of the $Cu_{0.21}Ti_{0.79}O_2$||VO_2||A-TiO_2 tri-layer. Even the TiO_2||VO_2||A-TiO_2 tri-layer exhibits still ($\Delta T_{IR} \approx 8$ %) although it possesses a Q_R of about 30 % only. Notably, the $Cu_{0.21}Ti_{0.79}O_2$||VO_2||A-TiO_2 tri-layer compared to the R-TiO_2||VO_2||A-TiO_2 tri-layer shows only a 10 % lower T_{lum} value and a similar ΔT_{sol} value. Furthermore, its values for T_{lum} and ΔT_{sol} agree very well with the predictions made in Fig. 2. In summary, the thermochromic performance of the $Cu_{0.21}Ti_{0.79}O_2$||VO_2||A-TiO_2 tri-layer is not quite as good as that of the R-TiO_2||VO_2||A-TiO_2 tri-layer reference, but it still enables growth of crystalline VO_2 at 300 °C, a deposition temperature where only amorphous VO_2 is formed on the plain substrate: Furthermore, the almost rutile $Cu_{0.21}Ti_{0.79}O_2$ buffer layer used was deposited at 400 °C which is 200 °C lower than the typical deposition temperatures of rutile TiO_2 in RF sputtering processes; it can even be lowered further down to even 200 °C without significant loss of layer quality (see Fig. S9 of the supplementary information). This means that the deposition temperature profile of a $Cu_{0.21}Ti_{0.79}O_2$||VO_2||A-TiO_2 compares favorably with that of a R-TiO_2||VO_2||A-TiO_2 tri-layer in terms of process time and energy efficiency and, thus, cost efficiency.

4. Conclusion

Several of the multilayer structures proposed in the literature use rutile TiO_2 as a seed or buffer layer for growing VO_2-based thermochromic multilayers that fulfill the requirements for commercialization. However, rutile TiO_2 growth requires temperatures of almost 600 °C, which are incompatible with large-area growth on float glass window panes. Conversely, a buffer layer such as TiO_2 with the same rutile structure as the high-temperature phase of VO_2 considerably improves the crystalline quality of the VO_2-based active layer of the thermochromic layer system, leading to enhanced performance at a given growth temperature (i.e. achieving thermochromic performance that exceeds target values) or enabling lower growth temperatures (i.e. still achieving thermochromic performance that just reaches target values). The deposition of polycrystalline rutile-structured $Cu_xTi_{1-x}O_2$ buffer layers on quartz glass substrates has been demonstrated at temperatures ranging from 200 °C to 400 °C. Furthermore, polycrystalline VO_2 can be deposited on these almost rutile $Cu_xTi_{1-x}O_2$ seed layers in crystalline form at 300 °C, whereas a layer deposited on a plain substrate remains amorphous and does not exhibit thermochromic behavior. The drop in performance of the $Cu_{0.21}Ti_{0.79}O_2$||VO_2||A-TiO_2 tri-layer test system compared to the R-TiO_2||VO_2||A-TiO_2 tri-layer reference system is small, especially considering the enhanced cost efficiency. Given that the deposition temperature of $Cu_{0.21}Ti_{0.79}O_2$ is much lower than that of R-TiO_2, its use can significantly save energy in large-scale production, making the $Cu_{0.21}Ti_{0.79}O_2$||VO_2||A-TiO_2 tri-layer system's cost efficiency far superior to that of the R-TiO_2||VO_2||A-TiO_2 reference system. Furthermore, using copper as the dopant adds to the cost efficiency due to its abundance. Here, the temperature profile of the proposed growth process for the three layers reads 400 °C (possibly 200 °C is sufficient) → 300 °C → 25 °C, rather than 600 °C → 300 °C → 25 °C. This profile is compatible with large-scale deposition on float glass, as all deposition temperatures in the proposed $Cu_{0.21}Ti_{0.79}O_2$||VO_2||A-TiO_2 system remain below the softening point (550–600 °C) of float glass. Thus, lower average temperature and smaller temperature variations should make the entire production process more energy efficient and more reliable. This study addresses the lowering of the overall fabrication temperature for a thermochromic tri-layer structure thereby significantly reducing the energy demand during film deposition. An effective strategy is proposed that employs inexpensive metal doping to decrease the growth temperature of the rutile TiO_2 buffer layer. The resulting rutile buffer layer not only reduces the formation temperature of VO_2 but also helps to maintain an excellent infrared modulation capability of the VO_2 layer deposited on top. In future work, other metal dopants of the TiO_2 buffer layer will be explored to further improve the buffer properties, i.e., yielding a widening of the band gap in addition to a rutile structure at low growth temperatures. Overall, this work establishes an important step for transforming thermochromic device concepts from laboratory prototypes into practical and market-competitive smart-window technologies.

Table 1
Thermochromic key quantities luminous transmittance (T_{lum}), solar energy transmittance modulation (ΔT_{sol}) and infrared energy transmittance modulation (ΔT_{IR}) for different multilayer structures of type $Cu_xTi_{1-x}O_2$ ||VO_2|| anatase TiO_2.

	$T_{lum,25\ °C}$ (%)	ΔT_{sol} (%)	ΔT_{IR} (%)
A-TiO_2 ‖ VO_2 ‖ A-TiO_2	59.00	0	0
TiO_2 ‖ VO_2 ‖ A-TiO_2	36.17	3.38	7.74
$Cu_{0.21}Ti_{0.79}O_2$ ‖ VO_2 ‖ A-TiO_2	45.20	4.11	8.53
R-TiO_2 ‖ VO_2 ‖ A-TiO_2	57.28	4.35	9.79

CRediT authorship contribution statement

Hao Lu: Writing – review & editing, Writing – original draft, Visualization, Methodology, Investigation, Formal analysis, Data curation. **Martin Becker:** Visualization, Supervision, Methodology, Funding acquisition. **Jan Luka Dornseifer:** Data curation. **Angelika Polity:** Methodology. **Peter J. Klar:** Writing – review & editing, Supervision, Resources, Project administration, Funding acquisition, Conceptualization.

Declaration of competing interest

We declare that there are no known competing financial interests or personal relationships that could have appeared to influence the work reported in this paper.

Acknowledgements

This work was supported by the German BMBF (Grant No. 03VP09691), the DFG under research grant 510965362 and the Sino-German mobility programme (Grant No. M-0764). Furthermore, we acknowledge Dr. Yunlei Wang from the Department of Mathematics, University of Bordeaux, for discussions.

Appendix A. Supplementary data

Supplementary data to this article can be found online at https://doi.org/10.1016/j.solmat.2025.114016.

Data availability

All data supporting the conclusions of this work are openly accessible via https://doi.org/10.22029/jlupub-19769.

References

[1] M. Casini, Active dynamic windows for buildings: a review, Renew. Energy 119 (2018) 923–934, https://doi.org/10.1016/j.renene.2017.12.049.

[2] M. Aburas, V. Soebarto, T. Williamson, R. Liang, H. Ebendorff-Heidepriem, Y. Wu, Thermochromic smart window technologies for building application: a review, Appl. Energy 255 (2019) 113522, https://doi.org/10.1016/j.apenergy.2019.113522.

[3] M.K. Dietrich, F. Kuhl, S. Benz, M. Becker, P.J. Klar, Optimizing thermochromic VO_2 by co-doping with W and Sr for smart window applications, Appl. Phys. Lett. 110 (14) (2017) 141907, https://doi.org/10.1063/1.4979700.

[4] H. Lu, L. Chen, R. Cao, X. Tao, X. Wang, M. Li, P. Li, Y. Lu, P.J. Klar, Y. He, $RuVO_2$ alloy epitaxial films: lowered insulator–metal transition temperature and retained modulation capacity, Appl. Phys. Lett. 116 (19) (2020) 192103, https://doi.org/10.1063/5.0005426.

[5] M. Becker, Y. Wollenweber-Bienerth, J. Hauptmann, E. Celik, F. Kuhl, C. Byrne, P. J. Klar, S. Benz, Assessing AlN||VO_2||AlN multilayer architectures deposited by ion-beam sputtering for smart window applications, ACS Appl. Electron. Mater. 6 (8) (2024) 6049–6058, https://doi.org/10.1021/acsaelm.4c00957.

[6] Y. Cui, Y. Ke, C. Liu, Z. Chen, N. Wang, L. Zhang, Y. Zhou, S. Wang, Y. Gao, Y. Long, Thermochromic VO_2 for energy-efficient smart windows, Joule 2 (9) (2018) 1707–1746, https://doi.org/10.1016/j.joule.2018.06.018.

[7] Y. Qiao, Z. Tang, Z. Wu, J. Wang, X. Sun, F. Yu, C. Wang, J. Mao, Q. Zhang, F. Cao, VO_2-based colorful smart windows with self-cleaning function, Sol. Energy Mater. Sol. Cell. 274 (2024) 113004, https://doi.org/10.1016/j.solmat.2024.113004.

[8] Z. Zhao, Y. Liu, D. Wang, C. Ling, Q. Chang, J. Li, Y. Zhao, H. Jin, Sn dopants improve the visible transmittance of VO_2 films achieving excellent thermochromic performance for smart window, Sol. Energy Mater. Sol. Cell. 209 (2020) 110443, https://doi.org/10.1016/j.solmat.2020.110443.

[9] N.F. Mott, Metal-insulator transition, Rev. Mod. Phys. 40 (4) (1968) 677–683, https://doi.org/10.1103/RevModPhys.40.677.

[10] H. Lu, L. Chen, R. Cao, X. Tao, X. Wang, M. Li, P. Li, Y. Lu, P.J. Klar, Y. He, Correlation of metal-to-insulator transition and strain state of VO_2 thin films on TiO_2 (110) substrates, Appl. Phys. Lett. 123 (4) (2023) 042104, https://doi.org/10.1063/5.0156782.

[11] G.B. Stefanovich, A.L. Pergament, D.G. Stefanovich, Electrical switching and mott transition in VO_2, J. Phys. Condens. Matter 12 (41) (2000) 8837–8845, https://doi.org/10.1088/0953-8984/12/41/310.

[12] Q. Lu, C. Sohn, G. Hu, X. Gao, M.F. Chisholm, I. Kylänpää, H.N. Lee, Metal–insulator transition tuned by oxygen vacancy migration across TiO2/VO2 interface, Sci. Rep. 10 (1) (2020) 18554, https://doi.org/10.1038/s41598-020-75695-1.

[13] X. Liu, S.-W. Wang, F. Chen, L. Yu, X. Chen, Tuning phase transition temperature of VO_2 thin films by annealing atmosphere, J. Phys. Appl. Phys. 48 (26) (2015) 265104, https://doi.org/10.1088/0022-3727/48/26/265104.

[14] N. Suzuki, Y. Xue, T. Hasegawa, S. Yin, Phase transition behavior and optical properties of F/Mo co-doped VO_2 for smart windows, Sol. Energy Mater. Sol. Cell. 251 (2023) 112105, https://doi.org/10.1016/j.solmat.2022.112105.

[15] M. Panagopoulou, E. Gagaoudakis, N. Boukos, E. Aperathitis, G. Kiriakidis, D. Tsoukalas, Y.S. Raptis, Thermochromic performance of Mg-doped VO_2 thin films on functional substrates for glazing applications, Sol. Energy Mater. Sol. Cell. 157 (2016) 1004–1010, https://doi.org/10.1016/j.solmat.2016.08.021.

[16] J. Wu, L. Tong, H. Wang, G. Liu, X. Fu, T. Fan, Regulation of phase transition temperature and preparation for doping-VO_2 smart thermal control films, J. Appl. Phys. 131 (8) (2022) 085101, https://doi.org/10.1063/5.0054066.

[17] F. Kuhl, S. Benz, M. Becker, P.J. Klar, Embedding quaternary $V_{1-x-y}Sr_xW_yO_2$ into multilayer systems to enhance its thermochromic properties for smart glass applications, ACS Appl. Electron. Mater. 4 (1) (2022) 513–520, https://doi.org/10.1021/acsaelm.1c01115.

[18] X. Wang, L. Chen, H. Lu, Y. Liu, P.J. Klar, Enhancing visible-light transmittance while reducing phase transition temperature of VO_2 by Hf–W co-doping, Appl. Phys. Lett. 118 (19) (2021) 191905, https://doi.org/10.1063/5.0047006.

[19] L. Rodríguez, F. Sandiumenge, C. Frontera, J.M. Caicedo, J. Padilla, G. Catalán, J. Santiso, Strong strain gradients and phase coexistence at the metal-insulator transition in VO_2 epitaxial films, Acta Mater. 220 (2021) 117336, https://doi.org/10.1016/j.actamat.2021.117336.

[20] D. Lee, J. Zhai, J. Lee, S. Kim, Sharpened VO_2 phase transition via controlled release of epitaxial strain, Nano Lett. 17 (9) (2017) 5614–5619, https://doi.org/10.1021/acs.nanolett.7b02271.

[21] M. Yang, W. Zhong, Z. Yu, L. Wang, X. Lin, J. Zhou, Suppression of structural phase transition in VO_2 by epitaxial strain in vicinity of metal-insulator transition, Sci. Rep. 6 (2016) 23119, https://doi.org/10.1038/srep23119.

[22] H. Kocer, M. Janssen, K. Kudo, P.J. Klar, Intensity tunable infrared broadband absorbers based on VO_2 phase transition using planar layered thin films, Sci. Rep. 5 (2015) 13384, https://doi.org/10.1038/srep13384.

[23] C. Jiang, Z. Zhao, H. Liu, L. Wang, H. Li, X. Cao, Phase-change VO_2-based thermochromic smart windows, Light Sci. Appl. 13 (1) (2024) 255, https://doi.org/10.1038/s41377-024-01560-9.

[24] K. Bao, X. Li, Chemical vapor deposition of vanadium dioxide for thermochromic smart window applications, J. Inorg. Mater. 39 (3) (2024) 233–258, https://doi.org/10.15541/jim20230386.

[25] X. Zhou, Y. Ping, J. Gao, D. Gu, H. Zhou, M. Yang, Y. Jiang, Facile fabrication of HfO_2/nanocomposite vanadium oxide bilayer film with enhanced thermochromic properties and excellent durability, Appl. Surf. Sci. 597 (2022) 153729, https://doi.org/10.1016/j.apsusc.2022.153729.

[26] H. Zong, D. Zhou, L. Yan, M. Li, W. Qiao, S. Zhang, Q. Hu, L. Bian, Preparation and characterization of HfO_2/VO_2/HfO_2 sandwich structures with low phase transition temperature, excellent thermochromic properties, and superior durability, Ceram. Int. 48 (5) (2022) 6734–6744, https://doi.org/10.1016/j.ceramint.2021.11.224.

[27] M. Kaufman, J. Vlček, J. Houška, S. Farrukh, S. Haviar, Design and scalable synthesis of thermochromic VO_2-based coatings for energy-saving smart windows with exceptional optical performance, ACS Appl. Mater. Interfaces 16 (42) (2024) 57268–57276, https://doi.org/10.1021/acsami.4c05696.

[28] J. Rezek, J. Szelwicka, J. Vlček, R. Čerstvý, J. Houška, M. Fahland, J. Fahlteich, Transfer of the sputter technique for deposition of strongly thermochromic VO_2-based coatings on ultrathin flexible glass to large-scale roll-to-roll device, Surf. Coating. Technol. 442 (2022) 128273, https://doi.org/10.1016/j.surfcoat.2022.128273.

[29] Y. Lu, Z. Cao, C. Chen, J. Li, Z. Deng, J. Qiu, Y. Zhan, C. Wang, Controllable air cooling of VO_x multilayer film with enhanced thermochromic property, Ceram. Int. 49 (11) (2023) 19541–19544, https://doi.org/10.1016/j.ceramint.2023.03.020.

[30] M.A. Butt, Thin-film coating methods: a successful marriage of high-quality and cost-Effectiveness—A brief exploration, Coatings 12 (8) (2022) 1115, https://doi.org/10.3390/coatings12081115.

[31] D. Kolenatý, J. Vlček, T. Bárta, J. Rezek, J. Houška, S. Haviar, High-performance thermochromic VO_2-based coatings with a low transition temperature deposited on glass by a scalable technique, Sci. Rep. 10 (2020) 11107, https://doi.org/10.1038/s41598-020-68002-5.

[32] D.C. Larsen, J.J. Mills, J.L. Sievert, Stress relaxation behavior of soda-lime glass between the transformation and softening temperatures, J. Non-Cryst. Solids 14 (1) (1974) 269–285.

[33] B. Zhu, H. Tao, X. Zhao, Effect of buffer layer on thermochromic performances of VO_2 films fabricated by magnetron sputtering, Infrared Phys. Technol. 75 (2016) 22–25, https://doi.org/10.1016/j.infrared.2016.03.006.

[34] M. Becker, S. Benz, F. Kuhl, Y. Wollenweber-Bienerth, E. Celik, J. Hauptmann, P. J. Klar, Employing ion-beam sputter deposited TiO_2 buffer layers for VO_2-related devices, ACS Appl. Electron. Mater. 5 (7) (2023) 3560–3570, https://doi.org/10.1021/acsaelm.3c00712.

[35] C. Byrne, H. Kuhl, M. Becker, P.J. Klar, Effect of Cu doping on the anatase-to-rutile phase transition in TiO_2 photocatalysts: theory and experiments, Appl. Catal. B Environ. 246 (2019) 266–275, https://doi.org/10.1016/j.apcatb.2019.01.046.

[36] Z. Ding, Y. Cui, D. Wan, J. Wang, High-performance thermal sensitive VO_2(B) thin films prepared by sputtering with TiO_2(A) buffer layer and first-principles calculations study, RSC Adv. 7 (47) (2017) 29496–29504, https://doi.org/10.1039/C7RA04075J.

[37] M. Tang, D. Yang, J. Wang, H. Chen, Y. Luo, Effects of Cu doping on the phase transition and photocatalytic activity of anatase/rutile mixed crystal TiO_2 nanocomposites, Mater. Res. Express 8 (8) (2021) 085007, https://doi.org/10.1088/2053-1591/ac0xxx.

[38] P. Dagur, A.U. Mane, S.A. Shivashankar, Thin films of VO_2 on glass by atomic layer deposition: microstructure and electrical properties, J. Cryst. Growth 275 (1–2) (2005) e1223–e1228, https://doi.org/10.1016/j.jcrysgro.2004.03.077.

[39] J. Jian, J. Kim, Q. Li, H. Lee, K. Park, Sharp semiconductor-to-metal transition of VO_2 thin films on glass substrates, J. Appl. Phys. 114 (24) (2013) 243505, https://doi.org/10.1063/1.4847590.

[40] K. Kato, S. Matsubara, T. Onda, Y. Tanaka, Study on thermochromic VO_2 films grown on ZnO-coated glass substrates for 'smart windows, Jpn. J. Appl. Phys. 42 (10R) (2003) 6523–6527, https://doi.org/10.1143/JJAP.42.6523.

[41] M. Becker, C. Byrne, F. Kuhl, P.J. Klar, Phase control of multivalent vanadium oxides VO_x by ion-beam sputter-deposition, physica status solidi (a) 219 (9) (2022) 2100828, https://doi.org/10.1002/pssa.202100828.

Supplementary Material: $Cu_xTi_{1-x}O_2$ Buffer Layers in VO_2–based Smart Windows – a viable compromise towards large-scale industrial production

Determination of the Cu content of the $Cu_xTi_{1-x}O_2$ thin films by XPS; Interplay between Cu valence states and oxygen supply during growth

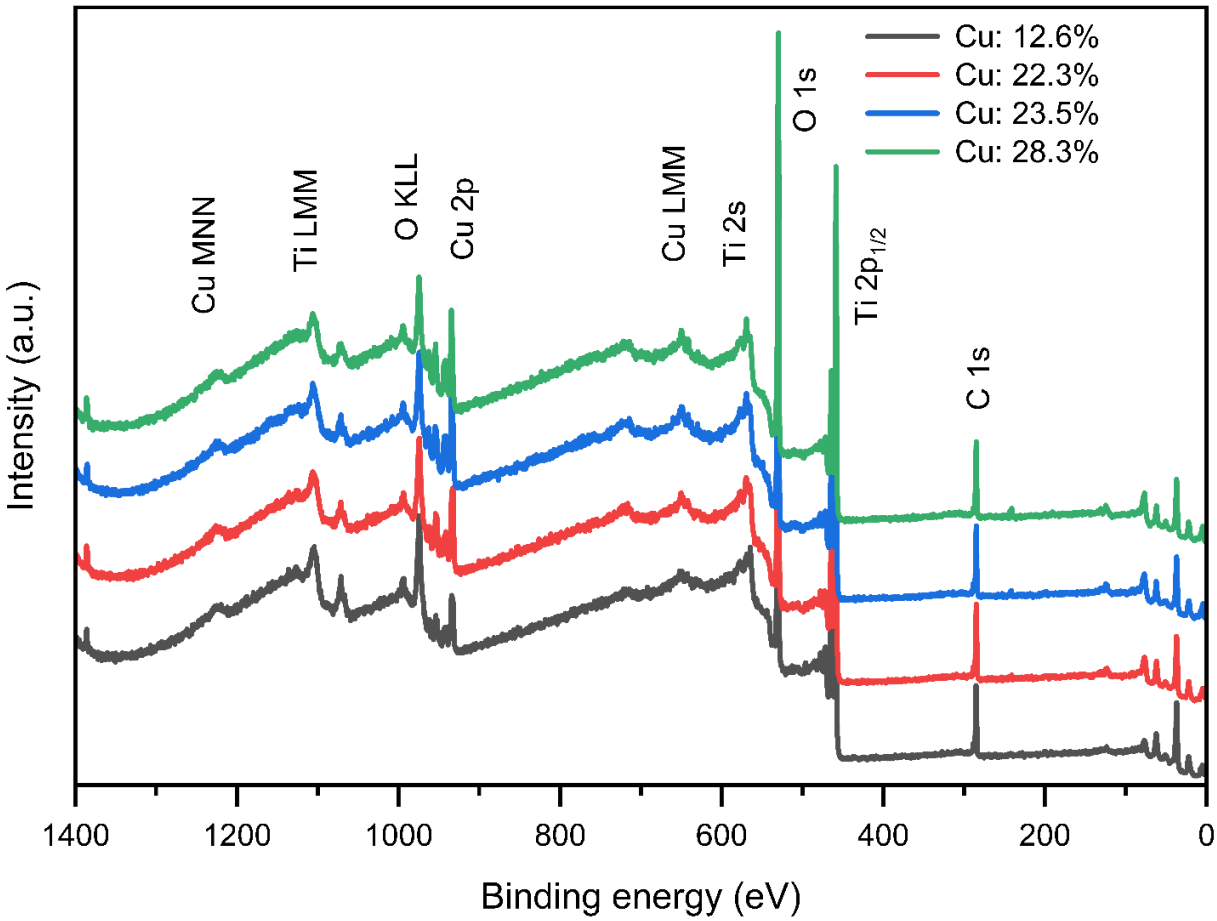

Figure S1. *XPS survey spectra of $Cu_xTi_{1-x}O_2$ thin films of different Cu:Ti ratio sputtered at 400°C heater temperature and 3 sccm oxygen flux.*

Fig. S1 shows, as typical examples, XPS survey spectra of $Cu_xTi_{1-x}O_2$ thin films grown with 3 sccm oxygen flux and different numbers of Cu wires on the ceramic TiO_2 target. The spectra reveal the exclusive presence of the elements Cu, Ti, O, and C in the film. Notably, the carbon (C) content is

attributed to impurities adsorbed from ambient air onto the film surface. Photoemission peaks Cu *2p*, Ti *2s*, Ti *2p*, O *1s*, and C *1s* as well as the corresponding Auger electron lines Cu LMM, Cu MNN, Ti LMM, and O KLL are clearly distinguishable in the spectra.

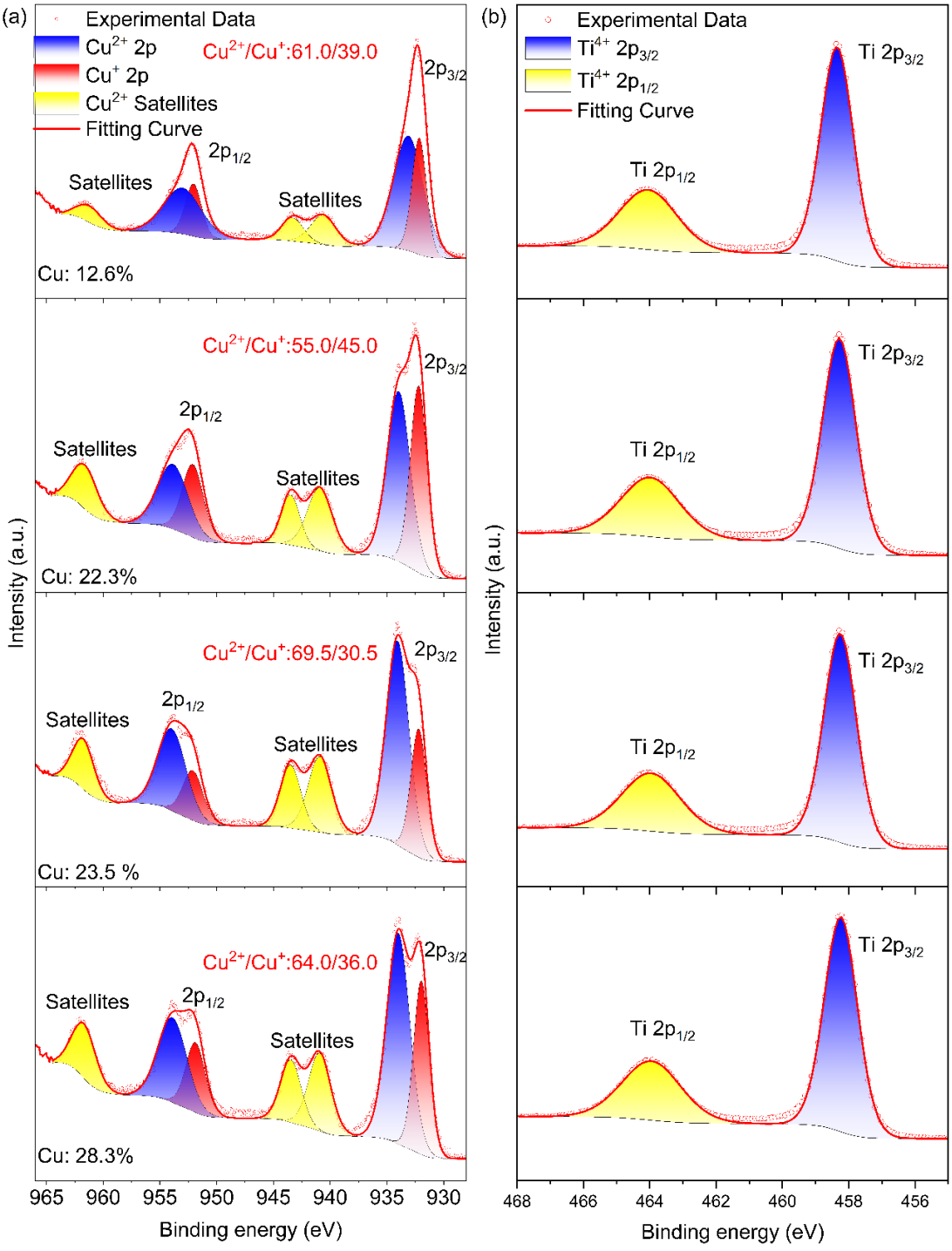

Figure S2. *Core level spectra of Ti 2p (a) and Cu 2p (b) for $Cu_xTi_{1-x}O_2$ thin films of different Cu:Ti ratio (films grown using 4, 8, 12 and 16 Cu wires) sputtered at 400°C heater temperature and 3 sccm oxygen flux.*

The [Cu]/[Ti] ratios of the $Cu_xTi_{1-x}O_2$ films were then determined by evaluation of the core levels Ti *2p* and Cu *2p*. XPS spectra of the corresponding core level regions are shown in **Fig. S2**. Both, Ti 2*p* and Cu 2*p*, show an additional splitting in Ti/Cu $2p_{1/2}$ and Ti/Cu $2p_{3/2}$ caused by spin-orbit coupling. While Ti manifests a singular valence state, exclusively existing as the +4 oxidation state, the coexistence of monovalent and divalent states of Cu is observed in all films. Cu 2*p* peak splitting thus results in two distinct binding energies corresponding to the two valence states of Cu, namely +2 and +1. As expected, the ratio of Cu^+ to Cu^{2+} ions in the films gradually increased with higher Cu doping concentrations. In order to quantify atomic species within the $Cu_xTi_{1-x}O_2$ films, we evaluate the areas under the Ti and Cu core level peaks. When increasing the number of Cu wires from 4 to 8, 12, and 16, we find 12.6%, 22.3%, 23.5%, and 28.3%, respectively.

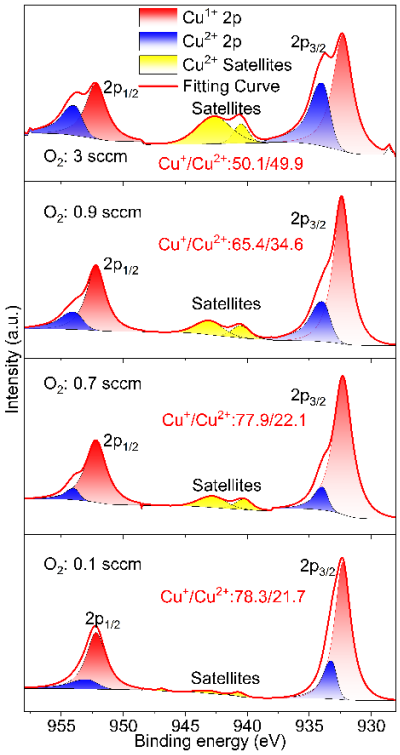

Figure S3. *Cu 2p core level spectra obtained by XPS. We compare $Cu_xTi_{1-x}O_2$ thin films deposited with different oxygen fluxes using the same number of Cu wires for doping purposes.*

The XPS results of the Cu 2*p* core level region in **Fig. S3** obtained of a series of thin films with the same Cu content deposited with different oxygen fluxes reveal the interplay of Cu incorporation and oxygen supply on the stoichiometry of the samples. With decreasing oxygen flux from 3 sccm to 0.1 sccm, the ratio of the Cu^+/Cu^{2+} increases from about 1 : 1 to almost 4 : 1. This behavior reflects Cu^{2+} and Cu^+ induces different numbers of oxygen vacancies. The increasing ratio of Cu^{1+}

to Cu^{2+} ions in the films leads to more oxygen vacancies as 1 mol% Cu^{2+} induces only 1 mol% oxygen vacancies, whereas 1 mol% Cu^{+} induces 1.5 mol% oxygen vacancies.

Identification of rutile and anatase phase in $Cu_xTi_{1-x}O_2$ thin films by Raman spectroscopy

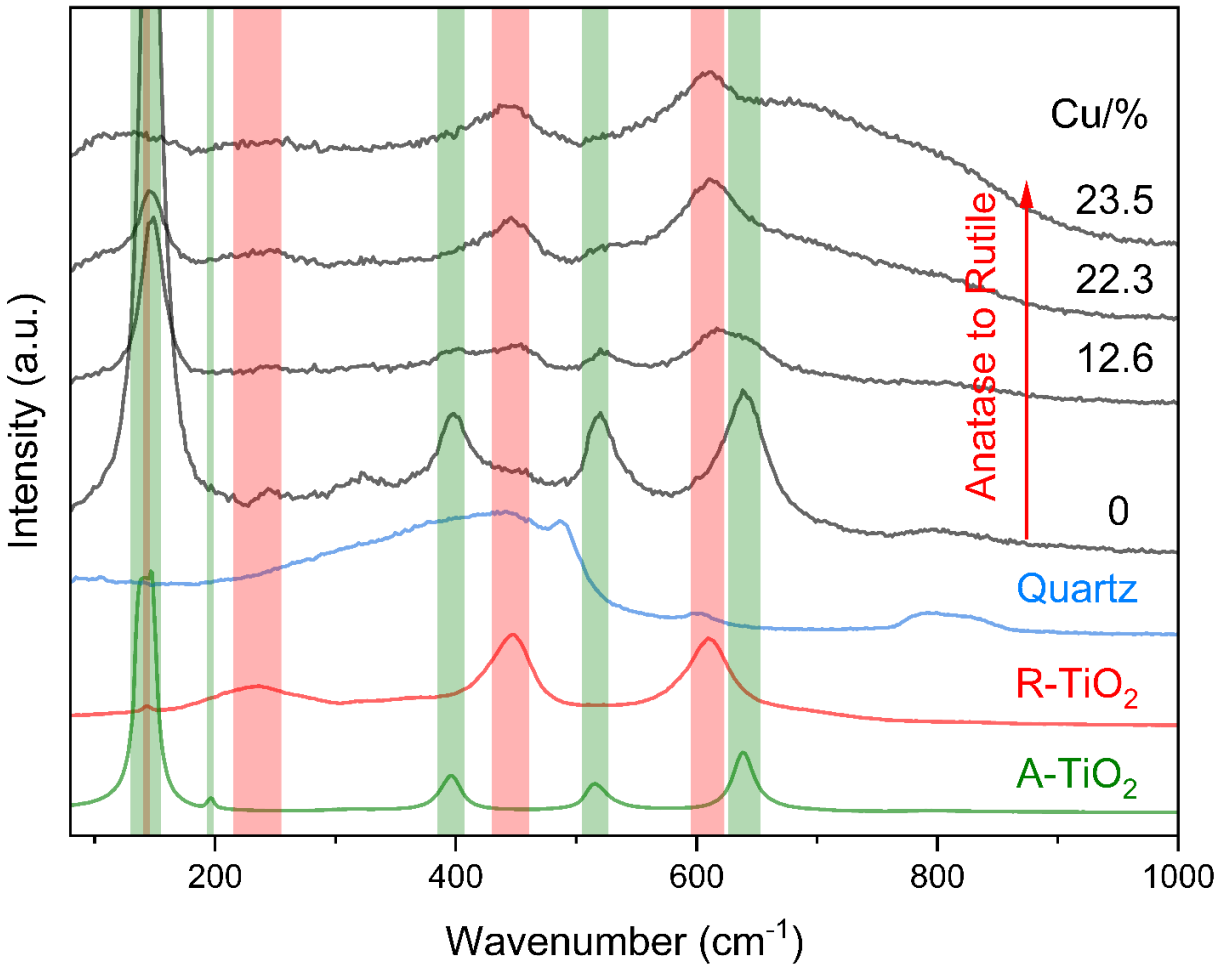

Figure S4. *Raman spectra of the $Cu_xTi_{1-x}O_2$ thin films of different Cu:Ti ratio sputtered at 400°C heater temperature and 3 sccm oxygen flux*

Fig. S4 shows a comparison of Raman spectra of the $Cu_xTi_{1-x}O_2$ thin films of different Cu content *x* sputtered at 400°C heater temperature and 3 sccm oxygen flux with those of the pristine quartz substrate as well as anatase and rutile TiO_2 thin films. The Raman vibrational modes of anatase TiO_2 are observed at Raman shifts of 145 cm^{-1}, 397 cm^{-1}, 520 cm^{-1}, and 640 cm^{-1}, corresponding to the E_g, B_{1g}, B_{1g}, and E_g modes, respectively.[1] These Raman signals define the four green vertical bands in the figure. Rutile TiO_2 exhibits a multi-phonon Raman signal at 240 cm^{-1}, and three one-phonon Raman bands at 167 cm^{-1} 444 cm^{-1} and 610 cm^{-1}, corresponding to the B_{1g}, E_g and A_{1g} modes. [2] These signals define the four pink vertical bands in the figure. At a Cu content of 12.6%, Raman spectroscopy reveals vibrational modes corresponding to both rutile and anatase structures, indicating their coexistence in the $Cu_xTi_{1-x}O_2$ alloy thin films at low Cu concentrations. On increasing the Cu content further up to approximately 23.5%, the modes of the anatase phase vanish completely. Thus, only modes corresponding to the rutile phase are present. Exemplarily, in the Raman spectrum of the $Cu_{0.235}Ti_{0.765}O_2$ thin film, only three distinct vibrational modes are still observed at 240 cm^{-1}, 145 cm^{-1}, 444 cm^{-1} and 610 cm^{-1}, corresponding to the multi-phonon signal and the B_{1g}, E_g and A_{1g} modes of the rutile TiO_2 structure. [2]

Characterization of $Cu_xTi_{1-x}O_2$ of different *x* by ellipsometry

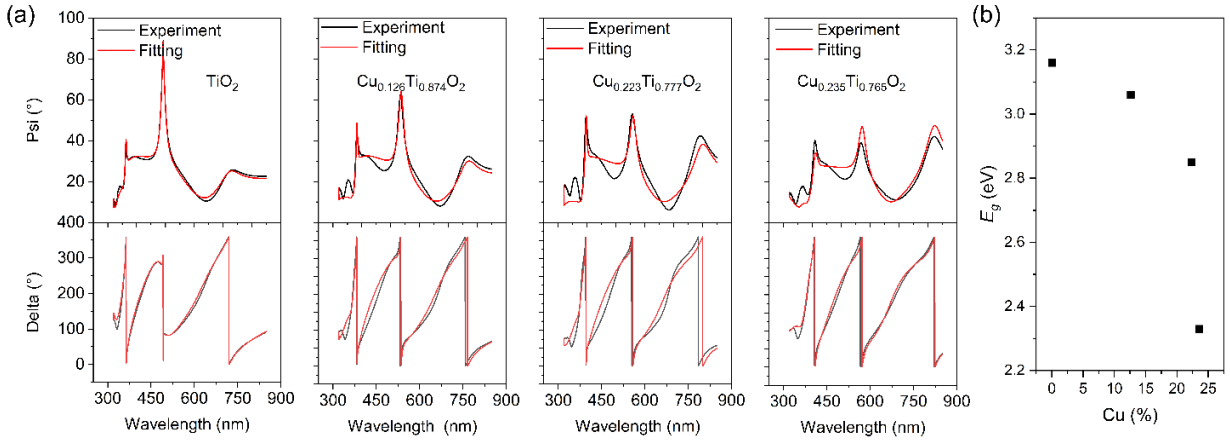

Figure S5. *Key quantities ψ and Δ obtained by spectroscopic ellipsometry (a). Experimental data are shown in black, whereas the results of the fitting procedure are shown in red. Aside from refractive index and layer thickness, the optical band gap can be deduced (b) and is seen to decrease with increasing Cu content.*

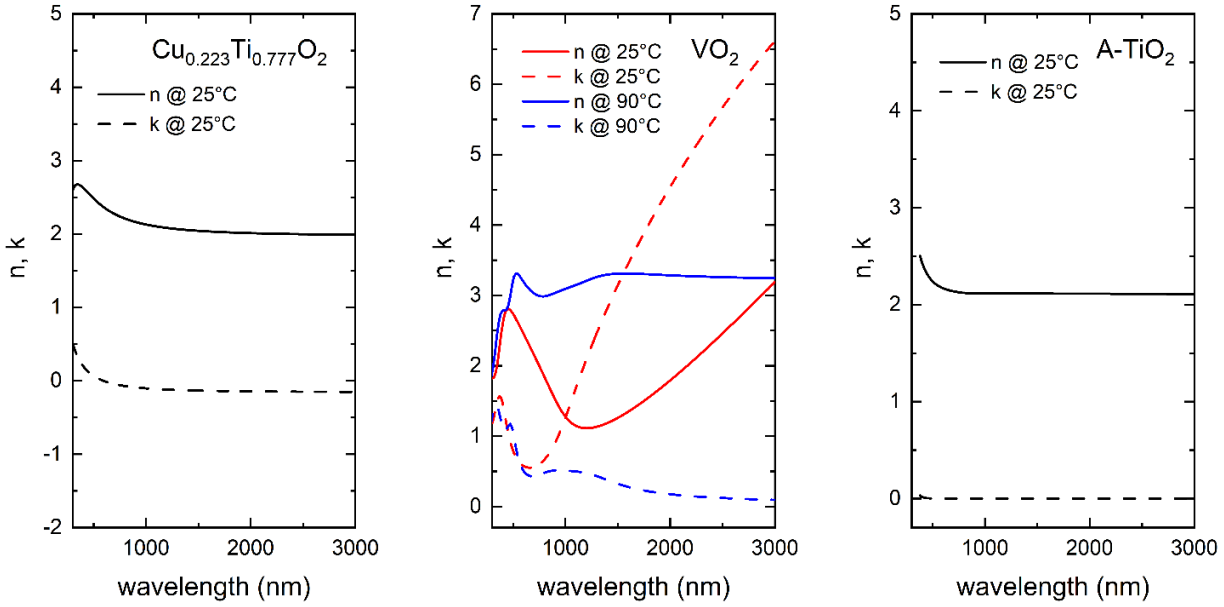

Figure S6. *The dispersions n(λ) and k(λ) of $Cu_{0.223}Ti_{0.777}O_2$, VO_2, and anatase TiO_2 measured and evaluated by ellipsometry. Those dispersions serve as input for the simulations of optical parameters of the multilayer stacks $CuTiO_2||VO_2||A\text{-}TiO_2$. The dispersions n(λ) and k(λ) of $Cu_{0.223}Ti_{0.777}O_2$ and anatase TiO_2 at 25 °C and 90 °C appear nearly identical on the scale presented.*

Evolution of the surface morphology of the $Cu_xTi_{1-x}O_2$ thin films with increasing *x*

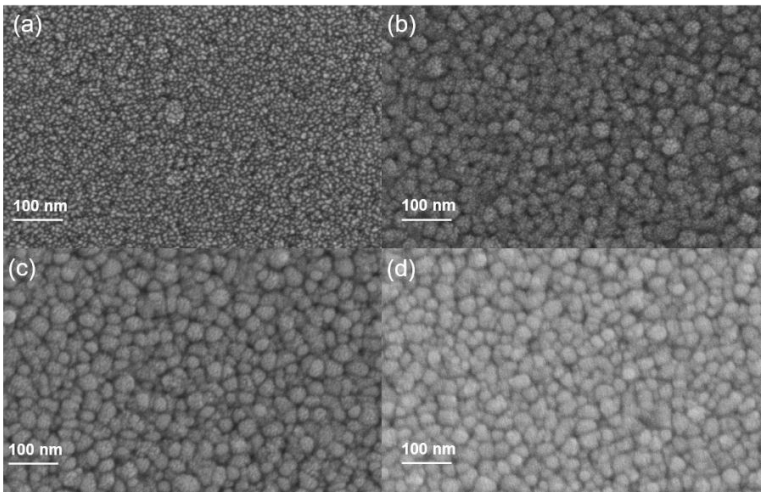

Figure S7. *SEM images corresponding to samples with different Cu concentrations. Binary TiO_2 exhibits grains with a defined and homogeneous distribution, cf. Fig. 3(a). Upon Cu doping, surface those grains seem to coalesce into larger particles, each consisting of numerous smaller particles which have conglomerated. The particles on the surface of pure TiO_2 exhibit a nominal diameter of approximately 10 nm, while the aggregated particles following clustering manifest a diameter ranging from 20 to 30 nm. This morphology, however, does not change upon further addition of Cu in the range investigated in this work.*

Raman characterization of VO_2 deposited at 400°C on quartz glass and different 40 nm thick buffer layers

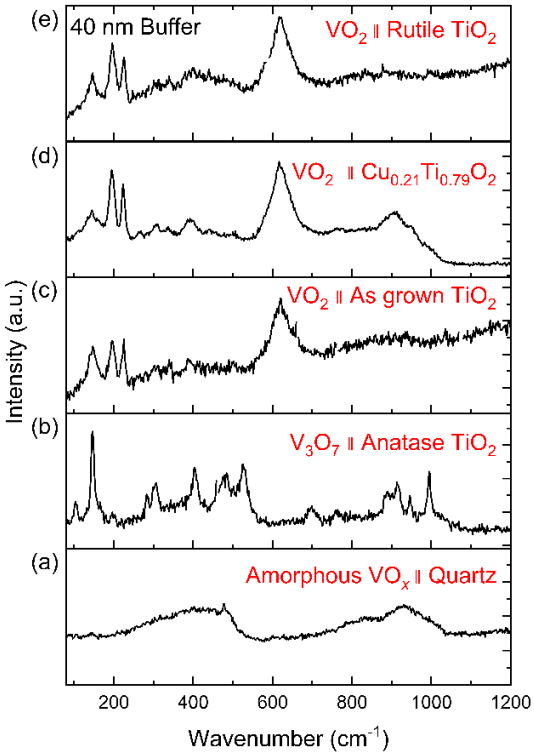

Figure S8. *Raman spectra of 40 nm VO_2 thin films deposited on 40 nm-thick buffer layers at 300°C. The VO_2 films were deposited on quartz substrate (a), IBS-grown anatase TiO_2 (b), as-grown mixed-phase TiO_2 (c), $Cu_{0.21}Ti_{0.79}O_2$ (d), and IBS-grown rutile TiO_2 (e).*

We have grown vanadium oxide on different buffer layers to evaluate which type of buffer layer supports the growth of VO_2. **Fig. S7** shows the Raman spectra of 50 nm VO_2 thin films deposited at 300°C on a plane quartz substrate, and four different 40 nm thick buffer layers, i.e., anatase TiO_2 obtained by ion-beam sputtering at room temperature, as-grown TiO_2 obtained by rf sputtering at 400°C, $Cu_{0.21}Ti_{0.79}O_2$ deposited by rf sputtering at 400°C, and rutile TiO_2 obtained by ion beam sputtering at 560°C. We compare the VO_x formation on the different buffer layers and the plain substrate based on the characteristic Raman spectra. To facilitate the analysis, all Raman spectra were background-corrected to eliminate features attributed to the quartz substrate. On the plane substrate the deposited VO_x is amorphous. On the anatase buffer, the deposited VO_x is V_3O_7 as indicated by the Raman modes at 105, 145, 284, 303, 403, 480, 526, 696, 890, 913, 947, and 994 cm^{-1}. [1] Thus, an anatase TiO_2 buffer does not promote the formation of pure-phase VO_2 thin films in a growth process at 400°C. The rf sputtered, as grown TiO_2 (which very likely contains residual Cu and exhibits a Q_R of 30% shows a feeble Raman spectrum characteristic for VO_2 with Raman signals at 143, 193, 222, and 621 cm^{-1}. The same holds for the $Cu_{0.21}Ti_{0.79}O_2$ buffer layer with Q_R = 81% and the rutile TiO_2 buffer. The results clearly underline that polycrystalline buffer layers exhibiting at least a fraction of grains of rutile phase promote the growth of crystalline VO_2.

Demonstration that almost rutile $Cu_{0.235}Ti_{0.765}O_2$ can be grown at 200°C, 300°C, and 400°C

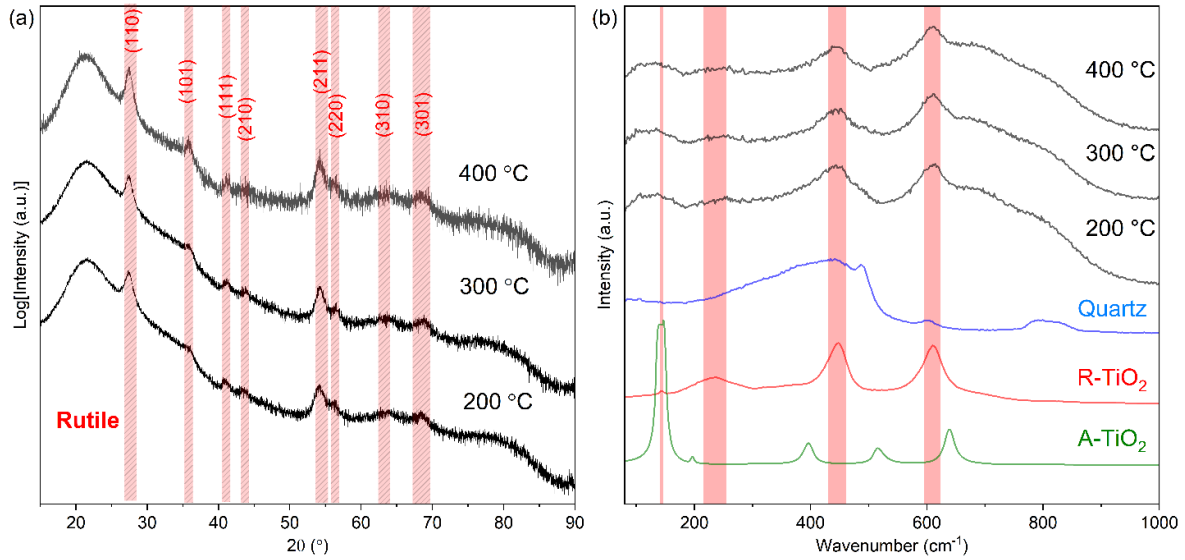

Figure S9. *XRD traces and Raman spectra of $Cu_{0.235}Ti_{0.765}O_2$ thin films grown at different growth temperatures. In all layers, the crystalline phase is observed to be rutile. If any, a descending trend in peak intensities is noted from 400°C to 200 °C. This observation would imply a slight degradation in the crystallinity or crystal quality of the thin film with a reduction in temperature. In Fig. S8(b), the Raman spectra of $Cu_{0.235}Ti_{0.765}O_2$ are shown. Again, no significant changes can be observed upon lowering the growth temperature. Thus, the growth temperature of $Cu_{0.235}Ti_{0.765}O_2$ thin films may be reduced to 200 °C without significantly lowering Q_R.*

References

[1] Becker, M., Byrne, C., Kuhl, F., Klar, P. J. “Phase control of multivalent vanadium oxides VO_x by ion-beam sputter-deposition.” *physica status solidi (a)* **219**.9 (2022): 2100828. https://doi.org/10.1002/pssa.202100828

[2] Kuhl, F., Becker, M., Hauptmann, J., Klar, P. J. “Raman scattering of $Ti_xV_{1-x}O_2$ thin films on (110) rutile TiO_2 in the low and high temperature phase adjacent to the metal–insulator transition.” *Journal of Raman Spectroscopy* **55**.8 (2024): 923–938. https://doi.org/10.1002/jrs.6614

5 Conclusions and Outlook

This dissertation presents an integrated investigation into strain-tunable metal–insulator transitions and low-temperature fabrication strategies for VO_2-based smart coatings. We demonstrate that the T_c and thermal hysteresis width of VO_2 thin films are governed by the strain distribution, which is modulated through film thickness on TiO_2 (110) substrates. By increasing film thickness from 7 nm to 300 nm, the strain state evolves from nearly fully strained to fully relaxed, allowing T_C to be tuned over a range of approximately 30 °C. A strain gradient along the growth axis gives rise to sequential phase switching of VO_2 sublayers, highlighting the interplay between mechanical constraints and electronic transitions.

In parallel, we develop a cost-effective and scalable multilayer structure for thermochromic applications using $Cu_xTi_{1-x}O_2$ as a rutile-phase buffer layer. This buffer promotes crystalline VO_2 growth at temperatures as low as 300 °C, circumventing the 600 °C requirement for conventional rutile TiO_2. Despite a slight performance reduction relative to traditional tri-layer systems, the $Cu_{0.21}Ti_{0.79}O_2\|VO_2\|TiO_2$ architecture achieves satisfactory thermochromic behavior while enabling deposition processes compatible with float glass and industrial sputtering conditions.

Together, these findings provide fundamental insights and practical solutions for tailoring VO_2-based smart coatings, contributing toward the realization of energy-efficient window technologies. Despite more than half a century of intensive research, the mechanism underlying the MIT in VO_2 remains unresolved. It is widely accepted that both lattice distortions and electronic correlations contribute to the transition, yet no single theoretical framework has captured the full complexity of the phenomenon. Several key questions remain open, including the role of chemical doping in reshaping the phase diagram, the impact of charged and magnetic defects on transport and structural properties, and the evolution of the phase transition under extreme conditions such as high pressure or strong magnetic fields. Furthermore, the interplay among electron–phonon coupling, polaronic effects, and electronic correlations; the order–disorder dynamics during the MIT; the emergence of nonthermal excited states in the first-order transition; and the influence of ferroelasticity, structural disorder, and domain formation—particularly in epitaxial or strain-engineered films—represent critical directions for future investigation.

Currently, the most widely explored application of VO_2 is in thermochromic smart windows. In practice, lowering the transition temperature or widening the optical band gap often comes at the cost of reduced infrared modulation. Multilayer optical designs provide an effective means to reduce the reliance on heavy doping while simultaneously enhancing visible transmittance, thereby preserving the intrinsic modulation capacity of VO_2 films to the greatest extent possible. Although doping and multilayer strategies can address fundamental performance trade-offs, large-scale deployment remains limited by technical and economic challenges—such as high synthesis temperatures, reliance on costly dopants, and difficulties in achieving uniform large-area coatings. Addressing these issues requires the development of low-temperature fabrication routes, energy-efficient processing, and the identification of earth-abundant dopants capable of effectively tuning the transition temperature.

By contrast, VO_2 remains underexplored in next-generation electronic and photonic devices, such as temperature-sensitive sensors, microactuators, neuromorphic elements, and optoelectronic switches. These emerging applications rely more sensitively on a detailed understanding of the MIT mechanism, and their full potential may only be realized as key fundamental questions are resolved.

Looking ahead, the convergence of microscopic insight and functional device innovation will be essential for unlocking the full technological potential of VO_2. As experimental capabilities and theoretical models continue to evolve, VO_2 stands as a model system in strongly correlated electron physics—where new physical insights and transformative applications may emerge hand in hand.

Bibliography

[1] L. R. Caswell. Andres del Rio, Alexander von Humboldt, and the twice discovered element. 2003.

[2] S. NG. Über das Vanadin: ein neues Metall, gefunden im Stangeneisen von Eckersholm, einer Eisenhütte. 1830.

[3] F. J. Morin. Oxides Which Show a Metal-to-Insulator Transition at the Néel Temperature. *Physical Review Letters*, 3(1):34–36, July 1959.

[4] A. Zylbersztejn and N. F. Mott. Metal-insulator transition in vanadium dioxide. *Physical Review B*, 11(11):4383–4395, June 1975.

[5] E. Hoschek and W. Klemm. Weitere Beiträge zur Kenntnis der Vanadinoxyde. *Zeitschrift für anorganische und allgemeine Chemie*, 242(1):63–69, July 1939.

[6] N. Perrakis. Contribution à l'étude de la magnéto-chimie du vanadium. *Journal de Physique et le Radium*, 8(11):473–480, 1927.

[7] O. Cook. High-temperature heat contents of V_2O_3, V_2O_4, and V_2O_5. *Journal of the American Chemical Society*, 69(2):331–333, 1947.

[8] Y. Cui, Y. Ke, C. Liu, Z. Chen, N. Wang, L. Zhang, Y. Zhou, S. Wang, Y. Gao, and Y. Long. Thermochromic VO_2 for Energy-Efficient Smart Windows. *Joule*, 18, 2018.

[9] V. Eyert. The metal-insulator transitions of VO_2: A band theoretical approach. *Annalen der Physik*, 514(9):650–704, Oct. 2002.

[10] J. Sugar. Energy levels of vanadium, v i through v xxiii. *Journal of Physical and Chemical Reference Data*, 8(4):865–918, 1979.

[11] S. Gedeon, V. Y. Lazur, and A. Kochemba. Calculation of atomic structure of neutral vanadium. *Semiconductor Physics, Quantum Electronics & Optoelectronics*, 28(2):221–231, 2025.

[12] S. Wang, Y. Qiu, H. Fang, and W. Schwarz. The challenge of the so-called electron configurations of the transition metals. *Chemistry–A European Journal*, 12(15):4101–4114, 2006.

[13] E. Schrödinger. Quantization as a problem of proper values. part ii. *Annalen der Physik*, 384(6):489–527, 1926.

[14] W. Pauli. Über den Zusammenhang des Abschlusses der Elektronengruppen im Atom mit der Komplexstruktur der Spektren. *Zeitschrift für Physik*, 31:765–783, 1925.

[15] G. E. Uhlenbeck and S. Goudsmit. Spinning electrons and the structure of spectra. *Nature*, 117(2938):264–265, 1926.

[16] J. T. Waber and D. T. Cromer. Orbital radii of atoms and ions. *Journal of Chemical Physics*, 42(12):4116–4123, 1965.

[17] J. P. Desclaux. Relativistic dirac–fock expectation values for atoms with $z = 1$ to $z = 120$. *Atomic Data and Nuclear Data Tables*, 12(4):311–406, 1973.

[18] D. C. Ghosh. Theoretical calculation of absolute radii of atoms and ions. *International Journal of Molecular Sciences*, 3(2):87–106, 2002.

[19] K. Brandhorst, J. Grunenberg, and M. Tamm. Two equivalent eg orbitals for the discussion of bonding in octahedral complexes. *Journal of chemical education*, 85(12):1692, 2008.

[20] J. E. House and K. A. House. *Descriptive inorganic chemistry*. Academic Press, 2015.

[21] Embedded peierls instability and the electronic structure of MoO_2.

[22] J. B. Goodenough. The two components of the crystallographic transition in VO_2. *Journal of Solid State Chemistry*, 3(4):490–500, Nov. 1971.

[23] N. F. Mott. Metal-Insulator Transition. *Reviews of Modern Physics*, 40(4):677–683, Oct. 1968.

[24] D. Adler and H. Brooks. Theory of Semiconductor-To-Metal Transitions. *Physical Review*, 155(3):826–840, Mar. 1967.

[25] H. W. Verleur, A. S. Barker, and C. N. Berglund. Optical Properties of VO_2 between 0.25 and 5 eV. *Physical Review*, 172(3):788–798, Aug. 1968.

[26] C. N. Berglund and H. J. Guggenheim. Electronic Properties of VO_2 near the Semiconductor-Metal Transition. *Physical Review*, 185(3):1022–1033, Sept. 1969.

[27] M. Marezio, D. B. McWhan, J. P. Remeika, and P. D. Dernier. Structural Aspects of the Metal-Insulator Transitions in Cr-Doped VO_2. *Physical Review B*, 5(7):2541–2551, Apr. 1972.

[28] J. P. Pouget and H. Launois. METAL-INSULATOR PHASE TRANSITION IN VO_2. *Le Journal de Physique Colloques*, 37(C4):C4–49–C4–57, Oct. 1976.

[29] M. F. Becker, A. B. Buckman, R. M. Walser, T. Lépine, P. Georges, and A. Brun. Femtosecond laser excitation of the semiconductor-metal phase transition in VO_2. *Applied Physics Letters*, 65(12):1507–1509, Sept. 1994.

[30] R. M. Wentzcovitch, W. W. Schulz, and P. B. Allen. VO_2: Peierls or Mott-Hubbard? A view from band theory. *Physical Review Letters*, 72(21):3389–3392, May 1994.

[31] S. Biermann, A. Poteryaev, A. I. Lichtenstein, and A. Georges. Dynamical Singlets and Correlation-Assisted Peierls Transition in VO_2. *Physical Review Letters*, 94(2), Jan. 2005.

[32] M. M. Qazilbash, M. Brehm, B.-G. Chae, P.-C. Ho, G. O. Andreev, B.-J. Kim, S. J. Yun, A. V. Balatsky, M. B. Maple, F. Keilmann, H.-T. Kim, and D. N. Basov. Mott Transition in VO_2 Revealed by Infrared Spectroscopy and Nano-Imaging. *Science*, 318(5857):1750–1753, Dec. 2007.

[33] J. D. Budai, J. Hong, M. E. Manley, E. D. Specht, C. W. Li, J. Z. Tischler, D. L. Abernathy, A. H. Said, B. M. Leu, L. A. Boatner, R. J. McQueeney, and O. Delaire. Metallization of vanadium dioxide driven by large phonon entropy. *Nature*, 515(7528):535–539, Nov. 2014.

[34] Z. Tao, T.-R. T. Han, S. D. Mahanti, P. M. Duxbury, F. Yuan, C.-Y. Ruan, K. Wang, and J. Wu. Decoupling of Structural and Electronic Phase Transitions in VO_2. *Physical Review Letters*, 109(16):166406, Oct. 2012.

[35] F. Kuhl, H. Lu, M. Becker, L. Chen, Y. Zheng, A. Polity, Z. Zhang, Y. He, and P. J. Klar. Raman scattering of $Ti_xV_{1-x}O_2$ thin films on (110) rutile TiO_2 in the low and high temperature phase adjacent to the metal–insulator transition. *Journal of Raman Spectroscopy*, 55(8):923–938, 2024.

[36] F. Théobald, R. Cabala, and J. Bernard. Essai sur la structure de VO_2 (B). *Journal of Solid State Chemistry*, 17(4):431–438, 1976.

[37] J.-P. Pouget. Basic aspects of the metal–insulator transition in vanadium dioxide VO_2: a critical review. *Comptes Rendus. Physique*, 22(1):37–87, 2021.

[38] Y. Oka, T. Yao, N. Yamamoto, Y. Ueda, and A. Hayashi. Phase transition and V^{4+}–V^{4+} pairing in VO_2 (B). *Journal of Solid State Chemistry*, 105(1):271–278, 1993.

[39] F. Beteille and J. Livage. Optical switching in VO_2 thin films. *Journal of Sol-Gel Science and Technology*, 13(1):915–921, 1998.

[40] D. B. Rogers, R. D. Shannon, A. W. Sleight, and J. L. Gillson. Crystal chemistry of metal dioxides with rutile-related structures. *Inorganic Chemistry*, 8(4):841–849, 1969.

[41] S. Shin, S. Suga, M. Taniguchi, M. Fujisawa, H. Kanzaki, A. Fujimori, H. Daimon, Y. Ueda, K. Kosuge, and S. Kachi. Vacuum-ultraviolet reflectance and photoemission study of the metal-insulator phase transitions in VO_2, V_6O_{13}, and V_2O_3. *Physical Review B*, 41(8):4993, 1990.

[42] V. Bermudez, R. Williams, J. Long, R. Reed, and P. Klein. Photoemission study of hydrogen adsorption on vanadium dioxide near the semiconductor-metal phase transition. *Physical Review B*, 45(16):9266, 1992.

[43] E. Goering, M. Schramme, O. Müller, H. Paulin, M. Klemm, S. Horn, et al. Angular-resolved photoemission on V_2O_3 and VO_2. *Physica B: Condensed Matter*, 230:996–998, 1997.

[44] E. Goering, M. Schramme, O. Müller, R. Barth, H. Paulin, M. Klemm, S. Horn, et al. LEED and photoemission study of the stability of VO_2 surfaces. *Physical Review B*, 55(7):4225, 1997.

[45] J. B. Goodenough. Direct cation–cation interactions in several oxides. *Physical Review*, 117(6):1442, 1960.

[46] M. M. Qazilbash, A. A. Schafgans, K. S. Burch, S. J. Yun, B.-G. Chae, B.-J. Kim, H.-T. Kim, and D. N. Basov. Electrodynamics of the vanadium oxides VO_2 and V_2O_3. *Physical Review B*, 77:115121, 2008.

[47] A. S. Barker, H. W. Verleur, and H. J. Guggenheim. Infrared optical properties of vanadium dioxide above and below the transition temperature. *Physical Review Letters*, 17(26):1286–1289, 1966.

[48] A. Romanyuk, R. Steiner, L. Marot, and P. Oelhafen. Temperature-induced metal–semiconductor transition in W-doped VO_2 films studied by photoelectron spectroscopy. *Solar Energy Materials and Solar Cells*, 91(19):1831–1835, Nov. 2007.

[49] W. Burkhardt, T. Christmann, B. Meyer, W. Niessner, D. Schalch, and A. Scharmann. W- and F-doped VO_2 films studied by photoelectron spectrometry. *Thin solid films*, 345(2):229–235, 1999.

[50] C. Si, W. Xu, H. Wang, J. Zhou, A. Ablat, L. Zhang, J. Cheng, Z. Pan, L. Fan, C. Zou, and Z. Wu. Metal–insulator transition in $V_{1-x}W_xO_2$: structural and electronic origin. *Physical Chemistry Chemical Physics*, 14:15021–15028, 2012.

[51] Y. Wu, L. Fan, Q. Liu, S. Chen, W. Huang, F. Chen, G. Liao, C. Zou, and Z. Wu. Decoupling the lattice distortion and charge doping effects on the phase transition behavior of VO_2 by titanium (Ti^{4+}) doping. *Scientific Reports*, 5:9328, 2015.

[52] H. Peng, A. Madan, P. Xu, N. Aetukuri, J. Jeong, M. G. Samant, and S. S. P. Parkin. Carrier density modulation of vanadium dioxide nanowires by field effect. *Physical Review Applied*, 5(5):054008, 2016.

[53] J. Jeong, N. Aetukuri, T. Graf, T. D. Schladt, M. G. Samant, and S. S. P. Parkin. Suppression of metal-insulator transition in VO_2 by electric field–induced oxygen vacancy formation. *Science*, 339(6126):1402–1405, 2013.

[54] H. Y. Xu, Y. H. Huang, S. Liu, K. W. Xu, F. Ma, and P. K. Chu. Effects of annealing ambient on oxygen vacancies and phase transition temperature of VO_2 thin films. *RSC Advances*, 6(83):79383–79388, 2016.

[55] Z. Zhang, F. Zuo, C. Wan, A. Dutta, J. Kim, J. Rensberg, R. Nawrodt, H. H. Park, T. J. Larrabee, X. Guan, et al. Evolution of metallicity in vanadium dioxide by creation of oxygen vacancies. *Physical Review Applied*, 7(3):034008, 2017.

[56] D. Mondal, S. R. Mahapatra, A. M. Derrico, R. K. Rai, J. R. Paudel, C. Schlueter, A. Gloskovskii, R. Banerjee, A. Hariki, F. M. DeGroot, et al. Modulation-doping a correlated electron insulator. *Nature Communications*, 14(1):6210, 2023.

[57] X. Tan, Z. Yang, Y. Zhou, X. Li, S. Chen, M. Liu, and Y. Wu. Symmetry-controlled structural phase transition temperature in chromium-doped vanadium dioxide. *Journal of Physical Chemistry C*, 120(48):28163–28168, 2016.

[58] D. Shiga, X. Cheng, T. T. Kim, T. Kanda, N. Hasegawa, M. Kitamura, K. Yoshimatsu, and H. Kumigashira. Electronic phase diagram of Cr-doped VO_2 epitaxial films studied by in situ photoemission spectroscopy. *Physical Review B*, 108(4):045112, 2023.

[59] Y. Muraoka and Z. Hiroi. Metal–insulator transition of vo_2 thin films grown on tio_2 substrates. *Applied Physics Letters*, 80(4):583–585, 2002.

[60] P. M. Anderson, J. P. Hirth, and J. Lothe. *Theory of dislocations*. Cambridge University Press, 2017.

[61] H. Lu, L. Li, Z. Tang, M. Xu, Y. Zheng, M. Becker, Y. Lu, M. Li, P. Li, Z. Zhang, et al. Correlation of metal-to-insulator transition and strain state of VO_2 thin films on TiO_2 (110) substrates. *Applied Physics Letters*, 123(4), 2023.

[62] L. L. Fan, S. Chen, Z. L. Luo, Q. H. Liu, Y. F. Wu, L. Song, D. X. Ji, P. Wang, W. S. Chu, C. Gao, et al. Strain dynamics of ultrathin VO_2 film grown on TiO_2 (001) and the associated phase transition modulation. *Nano Letters*, 14(7):4036–4043, 2014.

[63] Y. Cui, C. Cao, Z. Chen, H. Luo, and Y. Gao. Atomic and electronic structures of thermochromic VO_2 with Sb-doping. *Computational Materials Science*, 130:103–108, 2017.

[64] T. Ramesh, R. Prakash, and K. K. Shukla. Life cycle energy analysis of buildings: An overview. *Energy and buildings*, 42(10):1592–1600, 2010.

[65] R. Baetens, B. P. Jelle, and A. Gustavsen. Properties, requirements and possibilities of smart windows for dynamic daylight and solar energy control in buildings: A state-of-the-art review. *Solar energy materials and solar cells*, 94(2):87–105, 2010.

[66] H. K. Park and H. Kim. Acoustic insulation performance of improved airtight windows. *Construction and Building Materials*, 93:542–550, 2015.

[67] C. Tuchinda, S. Srivannaboon, and H. W. Lim. Photoprotection by window glass, automobile glass, and sunglasses. *Journal of the American Academy of Dermatology*, 54(5):845–854, 2006.

[68] R. F. Edlich, A. L. Fisher, K. L. Winters, M. J. Cox, D. G. Becker, J. H. Horowitz, L. S. Nichter, L. D. Britt, and W. B. Long. Use of uv-protective windows and window films to aid in the prevention of skin cancer. *Journal of Long-Term Effects of Medical Implants*, 14(1):15–30, 2004.

[69] I. J. Chabane and R. Bensalem. Passive cooling techniques under hot and arid climate. In *Proceedings of the 23rd Conference on Passive and Low Energy Architecture (PLEA 2006)*, Geneva, Switzerland, 2006.

[70] L. Q. Mai, B. Hu, T. Hu, W. Chen, and E. D. Gu. Electrical Property of Mo-Doped VO_2 Nanowire Array Film by Melting-Quenching Sol-Gel Method. *The Journal of Physical Chemistry B*, 110(39):19083–19086, Oct. 2006.

[71] G. Khan, K. Asokan, and B. Ahmad. Room temperature tunability of Mo-doped VO_2 nanofilms across semiconductor to metal phase transition. *Thin Solid Films*, 625:155–162, Mar. 2017.

[72] S. Guan, M. Souquet-Basiège, O. Toulemonde, D. Denux, N. Penin, M. Gaudon, and A. Rougier. Toward Room-Temperature Thermochromism of VO_2 by Nb Doping: Magnetic Investigations. *Chemistry of Materials*, 31(23):9819–9830, Dec. 2019.

[73] H. Lu, L. Chen, R. Cao, X. Tao, X. Wang, M. Li, P. Li, Y. Lu, P. J. Klar, and Y. He. $RuVO_2$ alloy epitaxial films: Lowered insulator–metal transition temperature and retained modulation capacity. *Applied Physics Letters*, 116(19):192103, May 2020.

[74] X. Wang, L. Chen, H. Lu, W. Fang, H. Li, W. Yin, M. Li, Y. Lu, P. Li, and Y. He. Enhancing visible-light transmittance while reducing phase transition temperature of VO_2 by Hf–W co-doping. *Applied Physics Letters*, 118(19), 2021.

[75] L. Hu, H. Tao, G. Chen, R. Pan, M. Wan, D. Xiong, and X. Zhao. Porous w-doped VO_2 films with simultaneously enhanced visible transparency and thermochromic properties. *Journal of Sol-Gel Science and Technology*, 77(1):85–93, 2016.

[76] Pgm market report may 2021. Technical report, Johnson Matthey, 2021.

[77] Mineral commodity summaries 2025: Tungsten. Technical report, U.S. Geological Survey, 2025. Zugriff am 18.11.2025.

[78] Y. Chen, Z. Wang, S. Chen, H. Ren, L. Wang, G. Zhang, Y. Lu, J. Jiang, C. Zou, and Y. Luo. Non-catalytic hydrogenation of VO_2 in acid solution. *Nature Communications*, 9(1):818, 2018.

[79] Y. Cui, S. Shi, L. Chen, H. Luo, and Y. Gao. Hydrogen-doping induced reduction in the phase transition temperature of VO_2: a first-principles study. *Physical Chemistry Chemical Physics*, 17(32):20998–21004, 2015.

[80] M. Panagopoulou, E. Gagaoudakis, N. Boukos, E. Aperathitis, G. Kiriakidis, D. Tsoukalas, and Y. Raptis. Thermochromic performance of Mg-doped VO_2 thin films on functional substrates for glazing applications. *Solar energy materials and solar cells*, 157:1004–1010, 2016.

[81] C. Ji, Z. Wu, X. Wu, J. Wang, J. Gou, Z. Huang, H. Zhou, W. Yao, and Y. Jiang. Al-doped VO_2 films as smart window coatings: reduced phase transition temperature and improved thermochromic performance. *Solar Energy Materials and Solar Cells*, 176:174–180, 2018.

[82] M. Gu, S. A. Wolf, and J. Lu. Two-dimensional Mott insulators in $SrVO_3$ ultrathin films. *Advanced Materials Interfaces*, 1(7):1300126, 2014.

[83] M. K. Dietrich, F. Kuhl, A. Polity, and P. J. Klar. Optimizing thermochromic VO_2 by co-doping with W and Sr for smart window applications. *Applied Physics Letters*, 110(14), 2017.

[84] N. Shen, S. Chen, Z. Chen, X. Liu, C. Cao, B. Dong, H. Luo, J. Liu, and Y. Gao. The synthesis and performance of Zr-doped and W–Zr-codoped VO_2 nanoparticles and derived flexible foils. *Journal of Materials Chemistry A*, 2(36):15087–15093, 2014.

[85] C. Ji, Z. Wu, L. Lu, X. Wu, J. Wang, X. Liu, H. Zhou, Z. Huang, J. Gou, and Y. Jiang. High thermochromic performance of Fe/Mg co-doped VO_2 thin films for smart window applications. *Journal of Materials Chemistry C*, 6(24):6502–6509, 2018.

[86] M. Jiang, X. Cao, S. Bao, H. Zhou, and P. Jin. Regulation of the phase transition temperature of VO_2 thin films deposited by reactive magnetron sputtering without doping. *Thin Solid Films*, 562:314–318, 2014.

[87] G. Xu, P. Jin, M. Tazawa, and K. Yoshimura. Thickness dependence of optical properties of VO_2 thin films epitaxially grown on sapphire (0001). *Applied Surface Science*, 244(1–4):449–452, 2005.

[88] S.-Y. Li, N. R. Mlyuka, D. Primetzhofer, A. Hallén, G. Possnert, G. A. Niklasson, and C. G. Granqvist. Bandgap widening in thermochromic Mg-doped VO_2 thin films: quantitative data based on optical absorption. *Applied Physics Letters*, 103(16):161907, 2013.

[89] L. Dai, S. Chen, J. Liu, Y. Gao, J. Zhou, Z. Chen, C. Cao, H. Luo, and M. Kanehira. F-doped VO_2 nanoparticles for thermochromic energy-saving foils with modified color and enhanced solar-heat shielding ability. *Physical Chemistry Chemical Physics*, 15(28):11723–11729, 2013.

[90] L. Zhao, L. Miao, C. Liu, C. Li, T. Asaka, Y. Kang, Y. Iwamoto, S. Tanemura, H. Gu, and H. Su. Solution-processed VO_2–SiO_2 composite films with simultaneously enhanced luminous transmittance, solar modulation ability and anti-oxidation property. *Scientific Reports*, 4:7000, 2014.

[91] M. Becker, Y. R. Wollenweber-Bienerth, S. Hartmann, A. Polity, S. Chatterjee, and P. J. Klar. Optimization and validation of the thermochromic performance of a trilayer coating of TiO_2/VO_2/TiO_2 for smart windows. *ACS Applied Electronic Materials*, 2025.

[92] Y. Chen et al. High performance and enhanced durability of thermochromic films using VO_2@ZnO core–shell nanoparticles. *ACS Applied Materials & Interfaces*, 9(33):27784–27791, 2017.

[93] M. Kaufman, J. Vlcek, J. Houska, S. Farrukh, and S. Haviar. Design and scalable synthesis of thermochromic VO_2-based coatings for energy-saving smart windows with exceptional optical performance. *ACS Applied Materials & Interfaces*, 16(42):57268–57276, 2024.

[94] Z. Qu, L. Yao, Y. Zhang, B. Jin, J. He, and J. Mi. Surface and interface engineering for VO_2 coatings with excellent optical performance: From theory to practice. *Materials Research Bulletin*, 109:195–212, 2019.

[95] M. Becker, Y. R. Wollenweber-Bienerth, J. Hauptmann, E. Celik, A. Polity, S. Chatterjee, and P. J. Klar. Assessing AlN|| VO_2|| AlN multilayer architectures deposited by ion-beam sputtering for smart window applications. *ACS Applied Electronic Materials*, 6(8):6049–6058, 2024.

[96] Z. Li, S. Zhao, Z. Shao, H. Jia, A. Huang, P. Jin, and X. Cao. Deterioration mechanism of vanadium dioxide smart coatings during natural aging: Uncovering the role of water. *Chemical Engineering Journal*, 447:137556, 2022.

[97] Y. Yang, X. Mao, Y. Yao, H. Huang, Y. Lu, L. Luo, X. Zhang, G. Yin, T. Yang, and X. Gao. Thickness effects on the epitaxial strain states and phase transformations in (001)-VO_2/TiO_2 thin films. *Journal of Applied Physics*, 125(8):082508, Feb. 2019.

[98] M. Tang, D. Yang, J. Wang, Q. Zhou, X. Zhu, and Y. Jiao. Effects of cu doping on the phase transition and photocatalytic activity of anatase/rutile mixed crystal TiO_2 nanocomposites. *Materials Research Express*, 8(8):085007, 2021.

6 Acknowledgments

I would like to express my sincere gratitude to all those who have provided invaluable support throughout the completion of this dissertation.

I sincerely thank the members of my doctoral committee—**Prof. Dr. Peter J. Klar**, **Prof. Dr. Yunbin He**, **Prof. Dr. Christian Heiliger**, and **Prof. Dr. Matthias Elm**—for their time, evaluation, and valuable insights regarding this thesis.

First and foremost, my deepest thanks go to my supervisor, **Prof. Dr. Peter J. Klar**. He has been not only a rigorous academic mentor but also a trusted friend. With patience, meticulous attention, and unfailing kindness, he engaged in in-depth academic discussions with me and reviewed every manuscript I wrote word by word.

My heartfelt appreciation also goes to **Dr. Martin Becker**, my most trusted collaborator in experimental work. Whenever research reached an impasse, he was almost always the person who helped me find an effective solution.

I would also like to express my heartfelt thanks to **Dr. Limei Chen** for her professional guidance on Raman spectroscopy and warm-hearted support.

I would like to express my sincere gratitude to my Master's supervisor in China, **Prof. Dr. Yunbin He**, for his unwavering support and guidance over the years.

During my doctoral studies, I am grateful to **Jan Luka Dornseifer** for his assistance with XPS measurements and the organization of the party. And thank all colleagues and faculty members who offered support at the institute, specifically **Dr. Fynn Kunze**, **Hannes Hergert**, **Nathalie Weigand**, **Tim Hecker**, **Julius Dinter**, **Marius Wasem**, **Dr. Markus Stein**, **Konstantin Keil**, **Prof. Dr. Detlev Hofmann**, **Dr. Nils Neugebauer**, **Dr. Mario Zscherp**, **Dr. Jörg Schörmann**, **Angelika Polity**, **Hans P. Jorde**, **Dr. Torsten Henning**, **Dr. Janis K. Eckhardt**, **Markus S. Friedrich**, and **Anja Denhardt**.

Beyond academic life, I have received tremendous personal support. I am especially thankful to **Prof. Dr. Sangam Chatterjee**, who provided me with a comfortable place to live; I am also grateful to **Dr. Florian Kuhl** for his practical help during

my early days in Germany and to **Yan R. Wollenweber-Bienerth** for fostering a harmonious office environment.

My sincere thanks also go to my Chinese friends —**Dr. Shuxing Wang** and **Zexi Wang**—for their care that felt like family. I appreciate **Dr. Wei Wang** and **Dr. Yu Wang** for our mutual academic encouragement, and **Muyao Tang** for the help and kindness he offered when I first arrived in Giessen, which made my life here far more enriching. I would also like to thank my cousin, **Dr. Yunlei Wang**, for his ongoing care regarding both my research progress and daily life.

Finally, my deepest gratitude goes to my family. Thank you for your unwavering support, trust, and encouragement. Your love has accompanied me every step of the way.

7 Declaration of Originality

I declare that I have completed this dissertation single-handedly without the unauthorized help of a second party and only with the assistance acknowledged therein. I have appropriately acknowledged and cited all text passages that are derived verbatim from or are based on the content of published work of others, and all information relating to verbal communications. I consent to the use of an anti-plagiarism software to check my thesis. I have abided by the principles of good scientific conduct laid down in the charter of the Justus Liebig University Giessen „Satzung der Justus-Liebig-Universität Gießen zur Sicherung guter wissenschaftlicher Praxis" in carrying out the investigations described in the dissertation.

Statement about the use of Artificial Intelligence (AI) based aids like ChatGPT or SchulKI by OpenAI, or Gemini by Google in the creation of my thesis (marked as applicable):

- ☐ I have not used any AI tool in preparing this text
- ☐ I used an AI tool in the following areas (multiple answers possible):
  - ☐ Finding ideas, stimulating my creativity
  - ☐ Understanding concepts, researching facts and definitions
  - ☐ Optimising a text that I drafted myself
  - ☐ Creating entire text passages following my prompts

I used the following AI tools to improve the given passages of the text in the manner stated: